Material-Driven Design of Mixed-Metal Nanoparticles for Enhanced Heating Efficiency and Cancer-Selective Thermal Response

Qi Jia
贾 琪

Material-Driven Design of Mixed-Metal Nanoparticles for Enhanced Heating Efficiency and Cancer-Selective Thermal Response

Qi JIA

Material-Driven Design of Mixed-Metal Nanoparticles for Enhanced Heating Efficiency and Cancer-Selective Thermal Response

Dissertation

for the purpose of obtaining the degree of doctor
at Delft University of Technology
by the authority of the Rector Magnificus,
Prof.dr.ir. H. Bijl,
chair of the Board for Doctorates
to be defended publicly on
Wednesday, 22 April 2026 at 12:30 pm

By

Qi JIA

This dissertation has been approved by the promotors.

Composition of the doctoral committee:

Rector Magnificus,	chairperson
Dr. K. Djanashvili	Delft University of Technology, promotor
Prof. Dr. ir. A.G. Denkova	Delft University of Technology, promotor

Independent Members:

Prof. dr. F. Hollmann	Delft University of Technology
Prof. dr. H.T. Wolterbeek	Delft University of Technology
Prof. dr. G.C. van Rhoon	Erasmus MC
Prof. dr. C. Platas-Iglesias	University of Coruna, Spain
Dr. S. Lacerda	Centre National de la Recherche Scientifique, France

The research presented in this thesis was performed at the Department of Radiation Science and Technology and Department of Biotechnology, Faculty of Applied Sciences, Delft University of Technology, the Netherlands. This research was funded by the China Scholarship Council (CSC).

Key words: Magnetic hyperthermia, iron oxide nanoparticles, element doping
Printed by: Proefschriftspecialist
Cover by: Qi Jia with the assistance of Doubao AI

ISBN: 978-94-6518-279-7

An electronic version of this dissertation is available at: http://repository.tudelft.nl

CONTENTS

CHAPTER 1 GENERAL INTRODUCTION **1**

CURRENT CANCER TREATMENTS AND THEIR LIMITATIONS 2

HYPERTHERMIA/THERMAL ABLATION AS AN ALTERNATIVE METHOD 3

MECHANISM AND BASIC PRINCIPLES OF MHT 4

TUNING MNPS FOR HIGHER SLP 7

BEYOND MHT: SECONDARY APPLICATIONS OF MNPS 10

SAFETY OF MHT 12

SCOPE AND OUTLINE OF THE THESIS 15

REFERENCES 16

ENHANCING MAGNETIC HYPERTHERMIA EFFICIENCY IN PD/FE-OXIDE HYBRID NANOPARTICLES THROUGH MN-DOPING **29**

INTRODUCTION 30

MATERIALS AND METHODS 31

RESULTS AND DISCUSSION 36

CONCLUSION 48

REFERENCES 49

ADAPTIVE DESIGN OF HO-DOPED IRON OXIDE NANOPARTICLES: COMPOSITION-STRUCTURE-PROPERTY INSIGHTS FOR ENHANCED MAGNETIC HEATING **53**

INTRODUCTION 54

MATERIALS AND METHODS 55

RESULTS AND DISCUSSION 57

CONCLUSION 66

REFERENCES 68

IN VITRO INVESTIGATION OF THE SYNERGISTIC EFFECTS OF MAGNETIC HYPERTHERMIA AND RADIOTHERAPY ENABLED WITH ^{166}HO:HO/FE-OXIDE NANOPARTICLES **71**

INTRODUCTION 72

MATERIALS AND METHODS 74

RESULTS AND DISCUSSION 76

Conclusions 80

References 81

Towards Selective Magnetic Hyperthermia of Tumors via pH-responsive Heating Modulated by ZIF-coated Fe-oxide NPs 83

Introduction 84

Materials and Methods 86

Results and Discussion 88

Conclusion 97

References 98

General conclusions and outlook 101

References 106

Summary 107

Samenvatting 109

List of publications 111

Acknowledgements 113

Curriculum Vitae 115

General Introduction

1

Current cancer treatments and their limitations

Cancer has been one of the biggest threats for human health for decades. Around 20 million new cases and 9.7 million deaths were reported in 2022 (Figure 1.1).[1, 2] Up to now, surgery, chemotherapy and radiotherapy are still the three main approaches applied for cancer treatment. Surgery is usually the first choice, which is performed to completely remove tumor tissues.[3] However, this is often associated with residual cancerous cells at the resection margins, microscopic deposits, and micrometastases, which can progress rapidly.[4] Besides, surgical intervention may potentially cause infections, decreased life quality, and postoperative recovery.[5,6]

Chemotherapy is effective in the treatment of malignant metastases, but due to its high toxicity and low delivery efficiency, the treatment often needs to be terminated before the desired effects have been achieved. Although recent studies focus on the combination of chemotherapeutic drugs with some targeting groups or drug delivery agents to improve delivery efficiency, the impact of the chemotherapeutics on the immune system may still affect healthy tissues and put the patient at increased risk of infection.[7]

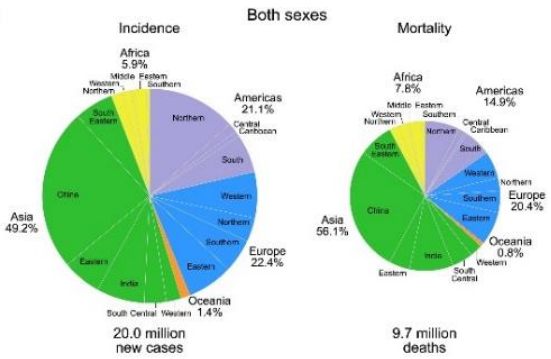

Figure 1.1 Regional distribution of global cancer incidence and mortality for men and women in 2022, adapted from [1].

Radiotherapy is widely used for treatment of malignant tumors at both surface and deep tissues due to its deep penetration.[8] According to how the radiation is applied, radiotherapy is mainly categorized into three kinds: external beam radiotherapy, brachytherapy and radionuclide therapy.[9, 10] External beam radiotherapy makes use of external radiation source such as X-rays and gamma-rays to irradiate localized tumors. Brachytherapy is conducted by placing radiation source in or near localized tumors. For radionuclide therapy, radioisotopes are bounded to targeting agents and injected intravenously or orally (^{131}I) for the treatments of metastases.[8, 11] However, considering radiation penetration depth and the ununiformed shape of tumors, it is difficult for external sources to deliver dose homogeneously to the entire tumor without putting adjacent organs and tissues at risk of radiation exposure. In addition, oxygen concentration, genetic factors and metabolites influence the clinical outcome of patients.[11] Despite the widespread use of surgery, chemotherapy and radiotherapy, new cancer treatments are still required as alternative methods with higher efficiency, lower toxicity and less invasiveness.[11]

Hyperthermia/thermal ablation as an alternative method

One of the alternative strategies is hyperthermia/thermal ablation (HT/TA), which has been reported as a possible treatment of intractable asthma, gonococcal infections and rheumatoid arthritis since 1930s.[12-14] Later in 1946-1970, the potential of HT/TA for cancer treatments was noticed and a series of studies were carried out since then.[15-19]

Hyperthermia is defined as a mild raising of body temperature from 37 °C to 42-46 °C.[20, 21] Healthy cells and tissues may survive at 44 °C for 1 h due to efficient internal heat dissipation mechanism that prevents further increase in the temperature, in contrast to solid tumors that do not have this adaptability.[22, 23] Besides, higher temperature may induce some cellular changes to make cells more sensitive to other treatments.[20, 24, 25] Therefore, HT/TA may be used to (partially) kill tumor cells or in combination with other treatment methods.

How temperature/heat kills cells

Temperature and heat are the most important factors for HT/TA. To achieve HT/TA, heat is generated, which leads to an increase in local body temperature. When the temperature increases to 41 ˚C, heat shock protein becomes upregulated, which is a defensive mechanism that protects cells from heat damage. Irreversible cell necrosis occurs when tissues are heated to more than 42 ˚C. However, no direct cell death or destruction of proteins and membrane will occur in the temperature range of hyperthermia. Owing to the vessel thrombosis and ischemia, rapid cell death can occur when the temperature is above 46 ˚C, and therefore, this temperature range is called thermal ablation.[26, 27]

Although thermal ablation can be a possible alternative for traditional cancer treatments, hyperthermia is more promising as it can conveniently be combined with other treatments, allowing for less damage to healthy tissue. For instance, hyperthermia may help to overcome drug resistance by modulation of different pathways such as DNA repair and immune response.[25, 28] The faster blood flow induced by moderate hyperthermia can accelerate the delivery of drugs and help to overcome hypoxia, which is highly connected to radioresistance. [20, 24, 25]

Heating sources for HT/TA

According to different heating sources, hyperthermia can be divided into two types: direct and indirect heating. Direct heating sources such as microwave (MW), radiofrequency (RF) and ultrasound may generate heat directly inside human body, while photothermal (PTT) and magnetic hyperthermia (MHT) therapies can only be performed after the injection of the corresponding agents.[29, 30] While the application of all direct heating requires precise calculations and implantation of the sources to focus the energy on the treatment site avoiding healthy tissues, the indirect heating source could offer the ability to generate heat exclusively at the place where both hyperthermia agents and excitation energy are present.[30, 31]

Ultrasound

Ultrasound technology provides enhanced spatial and dynamic control of heating, owing to its deep penetration in soft tissues and its capability to shape the energy distribution patterns.[32-34] In soft tissues, the attenuation coefficient describing ultrasound energy loss is approximately proportional to the applied frequency. Thus, the penetration depth for ultrasound treatment can be easily controlled from ±1 cm to ±10 cm, by adjusting the frequency in the range of 0.5-10 MHz.[35, 36] However, the reflection from gas surfaces and high acoustic absorption at bone interfaces make it difficult to apply ultrasound hyperthermia at certain sites.[31]

MW/RF

Among other hyperthermia methods, MW/RF therapy is currently most commonly applied for cancer patients. When MW/RF energy is applied to the human body, all tissues behave as lossy dielectric materials, meaning they are neither good electrical conductors nor effective insulators.[29,37] Therefore, the energy from MW/RF is gradually absorbed and a rise of temperature is induced at the irradiated area due to intermolecular friction.

PTT

PTT is conducted by the combination of injected photothermal agents and a near infrared (NIR, 700-1700 nm) laser. With high photothermal conversion efficiency, photothermal agents absorb energy from NIR laser and convert it into heat to increase the surrounding temperature. Using external laser irradiation with adjustable injection dosage, it is possible to precisely target tumor with a minimized damage to healthy tissues. However, the limited penetration depth of NIR laser (~3 cm) hinders its further application. [26, 27]

MHT

MHT makes use of the high tissue penetrating alternating magnetic field (AMF) to generate heat with application of magnetic materials such as iron oxide nanoparticles (Fe-oxide NPs). When Fe-oxide NPs are delivered to cancer tissue and the AMF is switched on, heat is produced through energy loss processes, such as Néel and Brownian relaxations and nanoparticle hysteresis loss. Taking advantage of the injection of magnetic materials and the high penetration depth of AMF, it is possible to achieve MHT in almost any part of the body. [38-41]

Mechanism and basic principles of MHT

The study of MHT started with the understanding of its mechanism and the basic parameters that influence the heat generation. As illustrated previously, MHT is the conversion of electromagnetic energy to heat by magnetic nanoparticles (MNPs).[42] The initial magnetic moments (*m*) of MNPs align with the applied external magnetic field and the energy loss during this process is transferred

to heat through hysteresis loss, Néel and Brownian relaxation.[42-44] To further illustrate the key parameters of this process, some basic principles of MNPs and heat dissipation equations need to be discussed.

Hysteresis loop and superparamagnetism

The hysteresis loop represents the magnetization (M) change with field (H), which is usually used to study the basic magnetic properties of MNPs. It is achieved by magnetizing and demagnetizing the MNPs in opposite directions and measuring the material magnetization parallel to the applied field. With a typical magnetization curve of ferro/ferrimagnetic materials shown in Figure 1.2, the following parameters can be obtained: (1) saturation magnetization (M_S), the maximum magnetization induced when all magnetic dipoles are aligned with the external magnetic field; (2) remanent magnetization (M_r), magnetization remaining after removal of the applied magnetic field; (3) coercivity (H_C), intensity of an external magnetic field required to force the magnetization to zero.[45, 46]

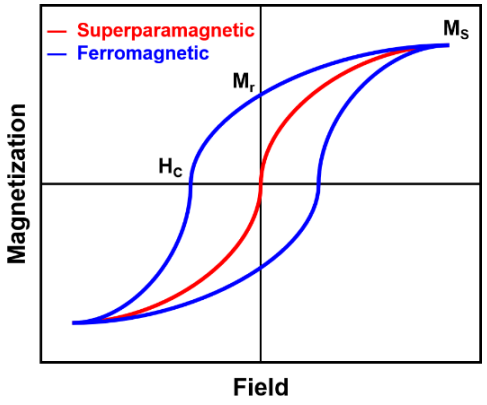

Figure 1.2 Magnetization curves of superparamagnetic and ferro/ferrimagnetic materials, with corresponding saturation magnetization (M_S), remanent magnetization (M_r) and coercivity (H_C).[46]

In bulk magnetic materials and relatively large nanoparticles, magnetic domains are usually organized into domain walls, whereas at particle sizes below a certain value, MNPs exhibit a single-domain character.[46] This size depends on the composition and morphology of MNPs next to their domain wall energy.[47] For Fe-oxide NPs such as magnetite (Fe_3O_4) and maghemite (γ-Fe_2O_3), this transition from multi-domain to mono-domain happens within 80-90 nm, while an even smaller particle size of <20-30 nm allows the transition of Fe-oxide NPs to superparamagnetic state.[44, 48]

The crystal lattice of MNPs possesses a preferred direction along one of its crystallographic axes in which magnetization is energetically favored. This property is known as anisotropy. In single-domain MNPs, the magnetic moment can adopt two stable orientations along this 'easy axis',

which are anti-parallel to each other and separated by an energy barrier. The anisotropy energy (E_a) depends on both the magnetocrystalline anisotropy constant (K) and the magnetic volume (V) of the MNPs.[49] For sufficiently small particles, typically below 20-30 nm, the thermal energy (k_BT) can exceed the energy barrier required to reverse the magnetic moment. As a result, the magnetic moments fluctuate between the two orientations. This thermally driven switching leads spontaneous and continuous reversal of the magnetic moments, producing a time-averaged net magnetization of zero, which is a behavior known as superparamagnetism.[50]

As shown in Figure 1.2, a similar sigmoidal curve is observed for superparamagnetic NPs, while no coercivity is shown in the hysteresis loop. The heating mechanism of both multi-domain and mono-domain MNPs are related to the generation of a hysteresis cycle, and the thermal loss is proportional to the area enclosed by the hysteresis loop (hysteresis loss). This unique magnetization behavior means that no energy loss is caused by hysteresis loss for superparamagnetic NPs.[46]

Besides hysteresis loss, Néel relaxation and Brownian relaxations are also the main heat generation mechanisms in MHT, especially for superparamagnetic NPs.[44] Néel relaxation refers to the internal rotation of the magnetic moments within MNPs,[51] which is typically hindered by magnetic frictions that tend to orient the magnetic domains in a given direction relative to the crystal lattice. Brownian relaxation refers to the external rotation of the nanoparticle itself, [52] which is controlled by the viscosity of the medium (η) in which the MNPs are placed, and all other mechanical parameters that restrict the movement.

Heat dissipation equations

The heat dissipation equations describe the parameters that govern the MHT. The specific absorption rate (SAR) and specific loss power (SLP) are defined to evaluate the heating conversion efficiency of the MNPs.[53] The amount of heat generated by MNPs depends on the heat dissipation power (P) and the density of the MNPs (ρ). For both multi- and mono-domain nanoparticles, P is given by the product of the area of each cycle (A) and the magnetic field frequency (f) (Eq. 1).[47]

$$SAR = SLP = \frac{P}{\rho} = \frac{f \times A}{\rho} \quad (1)$$

Since the hysteresis loss is absent in the case of superparamagnetic NPs, Eq. 1 is not applicable, and an alternative model developed by Rosensweig can be used to correlate the features of MNPs to the area of the hysteresis generated under AMF, and to calculate the heat generation (Eq. 2). [54]

$$P = f \times A = \mu_0 \pi H_{max}^2 f \chi'' \quad (2)$$

In this equation, μ_0 represents the permeability of free space, and the loss component of susceptibility (χ'') can be expressed as:

$$\chi'' = \chi_0 \frac{\omega\tau}{(1+\omega\tau)^2} \quad (3)$$

where χ_0 is the static susceptibility, which can be further expressed in Eq. 4.

$$\chi_0 = \frac{M_S^2 V}{3k_b T} \quad (4)$$

For superparamagnetic nanoparticles, heat is generated through both Néel and Brownian relaxation, where the effective relaxation time τ can be calculated as: [45]

$$\frac{1}{\tau} = \frac{1}{\tau_N} + \frac{1}{\tau_B} \quad (5)$$

where the relaxation time of Néel and Brownian relaxation can be expressed as Eqs. 6 and 7, respectively.

$$\tau_N = \tau_0 exp\ (\frac{KV_m}{k_B T}) \quad (6)$$

$$\tau_B = \frac{3V_H \eta}{k_B T} \quad (7)$$

In the above equations, V_m represents the magnetic volume, while V_H is the hydrodynamic volume of MNPs.

Both Néel and Brownian relaxation times are influenced by the volume of MNPs. However, τ_N is exponentially dependent on the magnetic volume of MNPs, and thus their anisotropy energy E_a, while τ_B is less dependent on the particles size.[42] For γ-Fe_2O_3 NPs smaller than 17 nm, heat generation is predominantly contributed by Néel relaxation and highly dependent on particle size.[42] With particle size bigger than 17 nm, τ_N is longer than τ_B, and the contribution of Brownian relaxation becomes predominant.

Moreover, the SLP value is also influenced by other physical properties of MNPs, such as the saturation magnetization M_S, magnetic anisotropy energy E_a, as well as the frequency f and the intensity (H) of the applied external magnetic field.

Tuning MNPs for higher SLP

The above-mentioned parameters affecting the SLP values and heating efficiencies of MNPs can be easily improved by tuning the frequency and intensity of AMF or by optimizing the properties of MNPs themselves. Modulations of the size and shape of the MNPs, modification of their surface, crystallinity and composition, incl. doping with other elements, and control of the aggregation state, are among typical parameters assessable through synthetic methods, with a direct effect on the saturation magnetization, magnetic anisotropy, relaxation times, and therefore, leading to an improved heating efficiency.

Size

As discussed earlier, the size of the NPs influences both the SLP and the heating efficiency through the contribution to the Néel relaxation. Therefore, increasing the SLP is often approached

through synthetic procedures aiming at an optimal NP diameter (d_{opt}) and monodispersity.[47] However, the d_{opt} cannot be fixed to a single value, even if optimal synthetic conditions are identified. Although the differences arising from the composition of the NPs are evident, the medium and the applied magnetic field also play an important role. For example, Sathya *et al.* synthesized a series of $Co_xFe_{3-x}O_4$ NCs and compared the SAR values of the iron content fixed as $Co_{0.7}Fe_{2.3}O_4$ with the particle size of 15, 17, 19, 23 and 27 nm. The highest heating performance was obtained with the NPs of 17 and 19 nm, which is similar as the previous experiments on iron oxide nanotubes.[55] Guardia *et al.* reported a higher d_{opt} of 23 nm for Au@Fe_xO_y, observing an increase in SAR at sizes ranging from 17 to 23 nm, and a clear decrease at 26 nm.[56] Fortin *et al.* investigated the SLP changes of maghemite and cobalt ferrite nanoparticles in the range of 5-20 nm in aqueous solvents of various viscosities.[57] The d_{opt} of maghemite in both water and glycerol were 14 - 16 nm and decreased with the applied frequencies (100 kHz - 1 MHz), while the d_{opt} of cobalt ferrite varied with the viscosities. Mehdaoui *et al.* studied the SAR change with $\mu_0 H_{max}$ of various particle sizes in the range of 5.6 - 27.5 nm at 54 kHz and 274 kHz.[58] The d_{opt} for both frequencies was 8.9 nm when the magnetic field was low (8, 16 mT for 54 kHz and 23, 30 mT for 274 kHz). With higher magnetic field, the d_{opt} increased to 13.7 nm and 19.7 nm. Despite the reported differences in d_{opt} depending on various parameters, the generally accepted range of d_{opt} for Fe-oxide NPs is 10 - 20 nm.

Shape and crystallinity

Different shapes of MNPs also exhibit different heating efficiencies. Although the reported SLP values vary, a general order of heat performance can be approximated as: nanotubes > nanoflowers > nanoctahedra > truncated NPs > nanorods.[47] These shapes can be acquired with different synthesis methods, which on its turn can also influence the crystallinity of MNPs.

The synthesis of MNPs can be both hydrolytic (co-precipitation, oxidative precipitation) or non-hydrolytic (solvothermal, thermal decomposition).[47] Hydrolytic methods make use of Fe(III) and Fe(II) salts and a strong base (NaOH or ammonia), allowing direct synthesis of water-dispersible MNPs and enabling easy scale-up of the mass of MNPs obtained per batch. However, hydrolytic methods always result in low crystallinity and are not suitable for shape control.[59] Non-hydrolytic methods use alkyl oxygen derivatives as oxygen donors to form Fe-oxide NPs at higher temperatures. This allows for varying a range of experimental conditions, such as heating rate, time and pressure.[60] Together with the choice of specific ligands/stabilizers and their molar ratio to the metal precursor, it is possible to allow or inhibit the growth of nanocrystal in certain directions, and hence, achieve shape-controlled synthesis. For instance, the nanocrystal growth along (111) direction leads to the formation of nanocubes, while the growth along (100) direction over (111) leads to the formation of octahedral MNPs.[61, 62] For cubic-shaped MNPs, the higher M_S values and better heating characteristics are due to their lower surface spin disorder, higher crystallinity, and higher magnetic moments.[47, 63] For nanorods and nano-octapods, their lower SLP and M_S values are mainly due to the intermediate FeO phase impurities. [45]

Composition

The density, saturation magnetization and magnetic anisotropy of MNPs can be controlled by changing their composition. Doping with different metal ions in Fe-oxide NPs is one of the most commonly used methods to tune the magnetic properties of MNPs. Transition metals such as Co, Mn and Zn with controlled distribution are typically doped into the crystalline structure of ferrites and described as $M_xFe_{3-x}O_4$. Sathya *et al.* synthesized a series of $Co_xFe_{3-x}O_4$ NCs with different Co/Fe ratio ($0.3 \leq x \leq 0.7$) and compared their SAR values at 105 kHz and 12-32 kAm^{-1}.[55] With same particle sizes of 20 ± 2 nm, SAR increased with increasing cobalt content regardless of the amplitude of AMF (from 600 ± 10 to 915 ± 10 $W/g_{(Co+Fe)}$). Jang *et al.* reported the doping of Zn and Mn in $M_xFe_{3-x}O_4$ with varied doping levels and the same size of 15 nm. The SLP value of $(Zn_{0.4}Mn_{0.6})Fe_2O_4$ obtained at 500 kHz and 3.7 kAm^{-1} was 432 W g^{-1}, which is significantly higher than that of commercial Feridex NPs (115 W g^{-1}).[64] With different magnetic moments and element radius, these cations partially occupy either octahedral or tetrahedral sites of $M_xFe_{3-x}O_4$, resulting in an increase in magnetic anisotropy. As discussed previously, the increase in magnetic anisotropy requires higher energy to flip both the magnetic and particle spins, which leads to higher SAR and SLP values.

Another strategy to alter the composition is the synthesis of heterostructures. By combining more than one domain with different composition, such as in bi-metal core-shell MNPs, the exchange coupling interaction results in the increase in SAR values.[65-67] An example of this approach was demonstrated by Lee *et al,* who tuned the magnetic properties and heating conversion efficiency with magnetically hard core and magnetically soft shell.[68] Due to the exchange coupling between different combinations of cores and shells, the SLP value could be maximized to 3034 W g^{-1}. Bordet *et al.* reported the carbidization process on the surface of their MNPs to form a core-shell structure (Fe@ICNPs),[69] which resulted in SAR of more than 1000 W/g after 4h of carbidization.

Aggregation state

In addition, to the described strategies that focus on the individual characteristics of NPs, another factor that influences the overall SLP is the aggregation state of MNPs. In biological environments like serum, blood, or other physiological fluids, MNPs naturally tend to cluster and form aggregates or agglomerates if they are not stabilized with specific coatings, due to their inherent physical interactions with surrounding components. The collective magnetic properties of MNPs may therefore be strongly influenced by exchange interactions and dipole-dipole interactions.[70] Exchange interactions refer to the quantum mechanical coupling of the magnetic moments from two neighboring atoms in either parallel or antiparallel directions. The exchange interactions between cores allow for cooperative behavior, and therefore, enhance susceptibility while maintaining superparamagnetic behavior. However, these exchange interactions are mainly related to multi-core nanoparticles that are directly formed with a controlled aggregation, such as nanoflowers.[71] For most MNPs that spontaneously form agglomerates or aggregates after synthesis, the impact on their magnetic properties is mainly influenced by dipole-dipole

interactions, which are highly dependent on the distance between MNPs.[72] A collective magnetic state is formed when the distances decrease, while the dipolar interactions increase. Since small Fe-oxide NPs are superparamagnetic and exhibit single domain character,[73] the orientation of each particle that forms the agglomerates or aggregates will strongly influence the collective magnetic properties. For instance, if the magnetic moments align and form chains, the collective magnetic properties will be much stronger than those oriented randomly.[74, 75]

Beyond MHT: secondary applications of MNPs

Aside from their magnetothermal performance in MHT, the magnetic and structural properties of MNPs have been intensively studied as enabling features for multimodal biomedical applications over the last decades. Thereby, substantial interest is centered on using MNPs to support and improve the outcomes of complementary therapeutic strategies, positioning them as versatile tools for imaging, targeted drug delivery, and multimodal cancer therapy.

Imaging

The magnetic properties of NPs specifically developed for MHT in fact match those responsible for contrast enhancement in magnetic resonance imaging (MRI) or magnetic particle imaging (MPI).[76-78] Moreover, MNPs can be combined with other imaging reporters to create multimodal probes that allow for their further application in other bioimaging modalities.[79-81]

Lu *et al.* reported ^{131}I conjugated Fe_3O_4 nanoparticles for combined MHT, MRI and single-photon emission computed tomography (SPECT) imaging.[82] The mesoporous Fe_3O_4 particles, prepared with thermal transformation of the precursor, were loaded with perfluoropentane and subsequently conjugated with ^{131}I to enable SPECT imaging. Similarly, Ince *et al.* reported the conjugation of ^{131}I to solid Fe_3O_4 NPs for multimodal SPECT and MR imaging.[83] Other examples include radiolabeling of MNPs with ^{111}In and ^{141}Ce for MRI/SPECT imaging-guided MHT.[84, 85] To enable optical imaging combined with MHT, MNPs are either combined with optical nanoparticles such as quantum dots (QDs)[86-88] and lanthanide based NPs,[89, 90] or modified with small molecule luminescent dyes.[91-93] Perton *et al.* designed a core-shell iron oxide@stellate mesoporous silica nanocomposites (IO@STMS NPs) with large pores grafted with CdSe/ZnS QDs, and as a result, in the presence of QDs, cellular endosomes displayed strong and photostable fluorescence signals.[94] Small molecular dyes, such such as Cyanine 5.5 and 7, can be easily attached to the surface of Fe_3O_4 NPs through the reaction with NHS (N-hydroxysuccinimide) ester and APTES ((3-aminopropyl)triethoxysilane) resulting in a strong fluorescence signal at 722 nm observed *in vivo* upon 662 nm excitation.[91]

MNPs-based synergistic therapies

The advantage of synergistic approaches in oncology is well-demonstrated. From this point of view, MNPs offer the possibility to be exploited for multiple therapeutic purposes based on their

intrinsic properties suitable for e.g. phototherapy next to MHP, or to provide heat during other treatments, such as radio- or chemotherapy, to enhance their efficacy.

Chemodynamic therapy (CDT) can be achieved with MNPs due to the existence of Fe^{2+} ions, which interact with H_2O_2 present in tumors and produce reactive oxygen species (ROS) through the Fenton reaction.[95] Du *et al.* reported the use of Fe^{2+}/Fe^{3+} pairs in hollow Fe_3O_4 mesocrystals as nanoenzymes to produce ROS for a self-augmented synergistic MHT-CDT.[96] The boosted reactive oxygen levels could not only induce cell apoptosis, but also reduce the expression of heat shock proteins, further improving the efficiency of MHT. The synergistic MHT-CDT was also demonstrated with MNPs containing Fe^{3+}, which could be reduced to Fe^{2+} by glutathione (GSH) overexpressed in tumor.[97]

The strong absorption of MNPs in the NIR region, together with their high photothermal conversion efficiency, enables their use in combined PTT and MHT,[98, 99] where a boosted heating effect can be achieved under AMF and NIR laser irradiation.[100] Due to their different heating mechanisms, the drawbacks of MHT, such as NPs diffusion or aggregation in tumor, could be overcome by combining it with PTT, while the limited tissue penetration of NIR light could be mitigated by the use of an AMF.[101]

Furthermore, mild MHT has been reported to accelerate blood flow, leading to increased oxygen supply and reduction of tumor hypoxia, which may help to overcome radiation resistance and improve the sensitivity for radiotherapy.[102-104] Moreover, internal radiotherapy can be applied using MNPs as nanocarriers.[105] By designing core-shell MNPs, applying radionuclide doping or functionalizing their surface with therapeutic radionuclides, MHT-RT can be achieved.[106, 107]

MHT-based drug delivery and controlled release

Similar to the benefits described for MHT-RT, the combination of MHT and chemotherapy can be achieved by using MNPs as nanocarriers for drug delivery. With the rational design of MNPs, the drugs can be either loaded into MNPs or conjugated to their surface.[108, 109] Benterrou *et al.* reported Fe-oxide NPs prepared by using mesoporous carbon as a hard template, which allowed for the loading of the pores with the anti-tumor drug doxorubicin (DOX),[110] whose further leakage from the pores was prevented by a polymer coating. Covalent attachment of the drugs to the MNPs, taking advantage of their large specific surface area, represents another option to enable combined MHT-chemotherapy.[111]

Moreover, the high temperature induced by MNPs is an ideal parameter for controlled drug release. After surface modification of thermal responsive materials, the loaded chemotherapeutics can be released only after the AMF is switched on.[112, 113] An example of this approach was demonstrated for Fe_3O_4 NPs modified with beta-cyclodextrin (β-CD) and heat responsive poly(N-isopropyl acrylamide) (PNIPAAm) that formed a hydrogel for the delivery of DOX through thermo-triggered release.[114] Other options for controlled drug release using MNPs include the use of pH/heat sensitive materials that help enhance the selectivity of chemotherapy.[115, 116]

Safety of MHT

While pursuing highly effective MHT through optimizing MNPs for greater SLP and achieving synergistic therapeutic effects, it is equally important to consider their impact on surrounding tissues. The drive to continually enhance MHT performance should not overshadow safety considerations, which are essential for clinical translation. Therefore, in view of future clinical translations, efforts should focus on systematic evaluations of the toxicity and biocompatibility of MNPs, improving the selectivity of MHT and developing strategies to prevent overheating. These aspects are crucial for ensuring treatment safety and minimizing damage to healthy tissues.

Biocompatibility and toxicity of MNPs

The biocompatibility and toxicity of NPs have always been the primary concern in all biomedical applications.[117, 118] Biocompatibility ensures that the NPs can deliver the desired performance without causing adverse effects, such as DNA damage, oxidative stress and apoptosis, while cytotoxicity concerns the oxidative stress and cell damage induced by the production of free radicals or ROS due to the high chemical reactivity of NPs.[119]

The physicochemical characteristics of NPs such as size, charge, morphology, composition and surface chemistry are the main factors influencing nanotoxicological reactions.[117, 119] As discussed previously, the MHT performance of MNPs is strongly related to their SLP values, which in turn are influenced by the size, morphology and composition of MNPs. Therefore, one of the commonly used methods to improve biocompatibility of MNPs while maintaining their heating efficiency, is surface modification. Surface coating with large biocompatible molecules, such as polyethylene glycol (PEG) provides a protective layer on the surface of NPs, which prevents them from aggregation, improves biocompatibility and increases their blood circulation time due to shielding from the immune system.[120] In addition to hydrophilic stealth polymers, alginate, chitosan and lipids are also good alternatives for improving biocompatibility.[120-127]

Studies also show that the toxicity of NPs is highly dose-dependent, suggesting that NPs can be only used safely below certain concentrations,[128, 129] while higher concentration may lead to increased cytotoxicity, oxidative stress and apoptosis. This is an important consideration, as achieving higher MHT efficacy often implies a critical mass/concentration of MNPs. From this perspective, enhancing the SLP, and thus the therapeutic effect, may present a good strategy for reducing MNPs dosage and, consequently, toxicity.

Selectivity of MHT

Therapeutic selectivity as a strategy to improve the safety of chemotherapy and PTT has been widely explored in studies, with the main focus being on limiting therapeutic action exclusively to the tumor region.[108, 109, 130] The mechanism of MHT involves heating MNPs through exposure to AMF, which penetrates deeply and acts specifically on NPs. This may inherently reduce safety concerns, provided that the MNPs remain well-localized within the tumor. Currently, the common

methods for delivering MNPs to tumors include intravenous administration of surface-functionalized particles bearing targeting vectors that recognize overexpressed cellular receptors, or direct intratumoral injection.[131-134] Although the latter approach appears more efficient for the precise delivery of MNPs, their post-injection fate, including their concentration and spatial distribution within the tumor tissue, remain uncertain. Furthermore, achieving accurate injection is a challenging task and poses the risk of damaging adjacent tissues.[135, 136]

Studies on tumors have proved that their abnormal growth often results in irregular features such as hypoxia, acidic pH and overexpression of glutathione.[137-141] These features are collectively referred as tumor microenvironment (TME) and have been extensively studied in the context of improving selective drug delivery to tumors for chemotherapy and PTT.[130, 142] By selecting specific features and designing TME-responsive materials accordingly, therapeutic selectivity can be effectively improved. For example, high level of endogenous H_2S in colorectal cancer has been used as a target for *in situ* synthesis of photothermal agent; [130, 143] H_2O_2 has been designed as a target to generate ·OH for chemodynamic therapy based on Fenton/Fenton-like reaction.[144]. Although TME is a good target for improving therapeutic selectivity and has also been mentioned in MHT-related research, it has only been used for TME-responsive synergistic therapy.[132, 133, 145, 146] The possibility of using TME to improve MHT selectivity remains to be explored.

Overheating problems

In ensure high efficacy and safety of MHT, the heating efficiency must be assessed and controlled.[147, 148] Even if MNPs are injected into the tumor center, once the temperature becomes too high, adjacent healthy tissues may still be damaged by heat due to heat diffusion within the body.[149] Therefore, the temperature during MHT should not only be carefully calculated and adjusted based on the size and morphology of the tumors, but also monitored and preferably controlled to minimize unnecessary damage.

Injection strategies and simulation

Limiting the effective temperature exclusively to the tumor region is challenging. Therefore, simulation studies were conducted to explore injection strategies for tumors of different sizes and shapes, and how to achieve an optimal delivery.[150-152] Hadadian *et al.* simulated the concentration of MNPs required to reach 45 °C in tumors of various sizes (80-700 mm^3) and demonstrated a non-linear relationship.[153] However, they were able to identify the minimum concentration for small tumors and volume-normalized concentrations for injections into large tumors. Further evaluation revealed that the critical size is associated with the fundamental limits of thermal diffusion, which forms a theoretical basis for determining injection doses depending on tumor volume.

For tumor with different shapes and morphologies, injection at multiple sites is necessary, rather than just in the center. In this respect, simulation studies represent a valuable asset, especially for tumors with a protrusion volume of more than 10% of the total.[151] Creating multiple hot-spots

within the tumor results in a more homogenous temperature distribution compared to the single-site injection strategy.[154, 155] An accompanying advantage is that each hot-spot requires a lower heating temperature due to heat diffusion, which can effectively reduce thermal damage to healthy tissues while maintaining a good MHT effect.[43, 156]

Thermometry

The damage to healthy tissues and death of necrotic cells can be minimized by precise and real-time control over therapeutic effects, which can be achieved through *in situ* thermometry.[157, 158] Infrared thermography is a non-invasive method for determining surface temperature and can be used for MHT, but its accuracy can be challenging. *In vivo* experiments calibrated with a fiber optical sensor indicated temperature errors up to 7 °C.[159] An alternative approach can be found in the rational design of MNPs, which contain components that allow them to act as nanothermometers, thus enabling *in situ* temperature monitoring of temperature, also known as nanothermometry.[149,157] Li *et al.* reported and optomagnetic heater-thermometer nanoplatform by combining lanthanide luminescent nanocrystals with Fe-oxide NPs.[158] The temperature-dependent luminescence lifetime, together with the depth-sensitive NIR-II luminescence intensity ratio, was exploited to achieve precise 3D thermographic mapping of tissues, reducing the measurement uncertainty to 0.12 °C. In addition, internal temperature can be also predicted via thermal distribution and simulation algorithms as part of pre-hyperthermia treatment planning.[160] With the guidance of real-time temperature monitoring and prediction, the accuracy and safety of MHT can be improved by preventing overheating and necrosis of normal tissues.

Temperature control

The precise and controllable temperature required for improving safety can be also achieved through self-regulating MNPs.[161] These smart MNPs have the ability to deliver MHT to tumors, but also to stop heating when a certain temperature is exceeded.[162] For all MNPs, Curie temperature (T_C) is the specific temperature at which they will lose their magnetic properties and become paramagnetic. Therefore, one way to prevent overheating is to use MNPs with a T_C in the range of 42-50 °C.[149, 162] Valente-Rodrigues *et al.* investigated the doping of Cr^{3+} into $Zn_{0.54}Co_{0.46}Cr_xFe_{2-x}O_4$ NPs to precisely tune their T_C.[162] As it was shown, the T_C of these hybrid NPs could be decreased from 78 °C (x = 0.1) to 27 °C (x = 0.6) by increasing the among of Cr^{3+}, while an optimal T_C of 42.3 °C could be achieved with the composition of $Zn_{0.54}Co_{0.46}Cr_xFe_{2-x}O_4$. By tuning T_C in a specific range, a temperature limit for MNPs is then determined regardless of their concentration. With a T_C of 57 °C, the highest temperature of 42 °C remained with increasing concentration from 6 to 60 mg/mL.[163]Although lowering T_C is a promising method to achieve self-regulating MHT, it usually results in lower M_S and heating efficiency due to the introduction of non-magnetic metal ions.[161] This requires new methods to achieve self-regulating MHT while maintaining the heating efficiency of MNPs.

Scope and outline of the thesis

This thesis investigates strategies to enhance the safety of MHT without compromising its therapeutic efficiency, building on the challenges and motivations outlined in **Chapter 1**.

Chapter 2 describes the enhancement of the magnetic properties of Pd/Fe-oxide NPs by doping with Mn. While Pd-core was necessary for the envisioned synergistic application in radiotherapy (^{103}Pd-doping), addition of paramagnetic Mn resulted in higher SLP and enabled an additional T_1-weighted MRI. A modified thermal decomposition method was used to prepare the hybrid NPs, and effects of Mn-doping on magnetic properties were thoroughly evaluated. Subsequently, the effect of this synthetic route on the resulting magnetic properties and heating efficiency was investigated in comparison to the commonly used cation-exchange method.

In **Chapter 3**, Mn was replaced with Ho to further investigate the potential of combining MHT and RT. Ho/Fe-oxide NPs were synthesized using co-precipitation method and the influence of Ho-doping ratio on their magnetic properties and heating efficiency was studied. It was demonstrated that the MHT efficiency of Ho-doped Fe-oxide NPs are strongly related to the amount of Ho, with the demonstrated optimum of 2.5%.

Subsequently, in **Chapter 4**, the MHT efficiency of the developed Ho/Fe-oxide NPs with a Ho-doping ratio of 2.5% and their potential to achieve synergistic MHT-RT at reduced therapeutic doses were studied. ^{165}Ho was irradiated with neutrons to ^{166}Ho and the ^{166}Ho/Fe-oxide NPs with the established Ho-doping ratio were synthesized. The therapeutic efficiency of MHT, RT and synergistic MHT-RT were investigated on cancerous cell lines U87 and U2OS. To investigate the possibility of reducing therapeutic doses, the efficient concentration/radiation doses for synergistic MHT-RT were determined and compared with those for MHT and RT performed separately.

Chapter 5 focused on the improvement of tumor-selectivity of MHT. To achieve this, pH-responsive ZIF-8 material was combined with Fe-oxide NPs to keep them aggregated, and thus unable to efficiently produce heat at physiological pH (7.4). First, the pH-responsive properties of the nanocomposites were investigated and the temperature behavior at higher (7.4) and lower pH (6.5), characteristic of the tumor environment, was compared. The AMF frequency was optimized to achieve maximal differences in temperature, and subsequently the tumor-selective effect was studied on cancerous and healthy cells.

References

1. Bray, F.; Laversanne, M.; Sung, H.; Ferlay, J.; Siegel, R. L.; Soerjomataram, I.; Jemal, A., Global cancer statistics 2022: GLOBOCAN estimates of incidence and mortality worldwide for 36 cancers in 185 countries. *CA: A Cancer Journal for Clinicians* **2024,** *74* (3), 229-263.
2. Jokhadze, N.; Das, A.; Dizon, D. S., Global cancer statistics: A healthy population relies on population health. *CA: A Cancer Journal for Clinicians* **2024,** *74* (3), 224-226.
3. Nguyen, K. T., Targeted nanoparticles for cancer therapy: promises and challenges. *J. Nanomed. Nanotechnol* **2011,** *2* (5), 1-2.
4. Jácome, A. A.; Johnson, B., Minimal Residual Disease in Colorectal Cancer: Are We Finding the Needle in a Haystack? *Cells* **2023,** *12* (7), 1068.
5. Dharap, S. B.; Barbaniya, P.; Navgale, S., Incidence and Risk Factors of Postoperative Complications in General Surgery Patients. *Cureus* **2022,** *14* (11), e30975.
6. Iversen, P.; Madsen, P. O.; Corle, D. K., Radical prostatectomy versus expectant treatment for early carcinoma of the prostate. Twenty-three year follow-up of a prospective randomized study. *Scandinavian journal of urology and nephrology. Supplementum* **1995,** *172*, 65-72.
7. Ingole, S.; Vasdev, N.; Tekade, M.; Gupta, T.; Pawar, B.; Mhatre, M.; Prasad, A. G.; Tekade, R. K., Chapter 13 - Toxic effects of cancer therapies. In *Public Health and Toxicology Issues in Drug Research*, Tekade, R. K., Ed. Academic Press: 2024; pp 353-379.
8. Citrin, D. E., Recent Developments in Radiotherapy. *New England Journal of Medicine* **2017,** *377* (11), 1065-1075.
9. Chargari, C.; Deutsch, E.; Blanchard, P.; Gouy, S.; Martelli, H.; Guérin, F.; Dumas, I.; Bossi, A.; Morice, P.; Viswanathan, A. N.; Haie-Meder, C., Brachytherapy: An overview for clinicians. *CA: A Cancer Journal for Clinicians* **2019,** *69* (5), 386-401.
10. Seniwal, B.; Thipe, V. C.; Singh, S.; Fonseca, T. C. F.; Freitas de Freitas, L., Recent Advances in Brachytherapy Using Radioactive Nanoparticles: An Alternative to Seed-Based Brachytherapy. *Frontiers in Oncology* **2021,** *11*, 766407.
11. Zafar, A.; Khatoon, S.; Khan, M. J.; Abu, J.; Naeem, A., Advancements and limitations in traditional anti-cancer therapies: a comprehensive review of surgery, chemotherapy, radiation therapy, and hormonal therapy. *Discov Oncol* **2025,** *16* (1), 607.
12. Miller, H.; Piness, G., Hyperthermia induced by high frequency electric current in the treatment of intractable asthma. *Jour Allergy* **1931,** *2* ((6)), 436-443.
13. Nicholls, E. E.; Hansson, K. G.; Stainsby, W. J., Treatment of rheumatoid arthritis with hyperthermia produced by a high-frequency current. *Journal of Bone and Joint Surgery* **1934,** *16*, 69-74.
14. King, A. J.; Williams, D. I.; Nicol, C. S., Hyperthermia in the Treatment of Resistant Gonococcal and non-Specific Urethritis. *The British journal of venereal diseases* **1943,** *19* (4), 141-54.
15. Hartmann, G. D., Experimental research on the treatment of cancer by raising the fever; effect of tetrahydro-beta-naphthylamine on the growth of benzopyrene tumors in rabbits and rats. *Bulletin de l'Association francaise pour l'etude du cancer* **1947,** *34* (2), 188-92.
16. Barth, G.; Garkisch, H., The effect of hyperthermy on tumors. Animal experimental investigations on the influence of a sound environment in tumor treatment with short-wave

hyperthermy, examination by means of injection of the carcinoma with hyaluronidase English summ. *Arztl Forsch* **1960,** *14* ((1)), 55-64.

17. Gilchrist, R. K., Potential Treatment of Cancer by Electromagnetic Heating. *Surgery Gynecology & Obstetrics* **1960,** *110* (4), 499-500.
18. Mori, K., Study on adjuvant therapies in cancer chemotherapy especially on the combination of hyperthermia and hyperbaric oxygenation. *Nagoya J Med Sci* **1967,** *29* ((4)), 275-316.
19. Vermel, E. M.; Kuznetsova, L. B., Hyper thermy in Treating Malignant Affections. *Voprosy Onkologii (St. Petersburg)* **1970,** *16* (2), 96-102.
20. Włodarczyk, A.; Gorgoń, S.; Radoń, A.; Bajdak-Rusinek, K., Magnetite Nanoparticles in Magnetic Hyperthermia and Cancer Therapies: Challenges and Perspectives. *Nanomaterials* **2022,** *12* (11), 1807.
21. Datta, N. R.; Ordonez, S. G.; Gaipl, U. S.; Paulides, M. M.; Crezee, H.; Gellermann, J.; Marder, D.; Puric, E.; Bodis, S., Local hyperthermia combined with radiotherapy and-/or chemotherapy: Recent advances and promises for the future. *Cancer Treatment Reviews* **2015,** *41* (9), 742-753.
22. Dutz, S.; Hergt, R., Magnetic nanoparticle heating and heat transfer on a microscale: Basic principles, realities and physical limitations of hyperthermia for tumour therapy. *International Journal of Hyperthermia* **2013,** *29* (8), 790-800.
23. Van der Zee, J., Heating the patient: a promising approach? *Annals of oncology* **2002,** *13* (8), 1173-1184.
24. Ahmed, K.; Tabuchi, Y.; Kondo, T., Hyperthermia: an effective strategy to induce apoptosis in cancer cells. *Apoptosis* **2015,** *20* (11), 1411-1419.
25. Abreu, M. M.; Chocron, A. F.; Smadja, D. M., From cold to hot: mechanisms of hyperthermia in modulating tumor immunology for enhanced immunotherapy. *Front Immunol* **2025,** *16*, 1487296.
26. Li, X.; Lovell, J. F.; Yoon, J.; Chen, X., Clinical development and potential of photothermal and photodynamic therapies for cancer. *Nature Reviews Clinical Oncology* **2020,** *17* (11), 657-674.
27. Xu, C.; Pu, K., Second near-infrared photothermal materials for combinational nanotheranostics. *Chemical Society Reviews* **2021,** *50* (2), 1111-1137.
28. Oei, A. L.; Vriend, L. E. M.; Crezee, J.; Franken, N. A. P.; Krawczyk, P. M., Effects of hyperthermia on DNA repair pathways: one treatment to inhibit them all. *Radiation Oncology* **2015,** *10* (1), 165.
29. Vrba, J.; Franconi, C.; Lapes, M., Theoretical limits for the penetration depth of intracavitary applicators. *International Journal of Hyperthermia* **1996,** *12* (6), 737-742.
30. Zhu, Y.; Li, Q.; Wang, C.; Hao, Y.; Yang, N.; Chen, M.; Ji, J.; Feng, L.; Liu, Z., Rational Design of Biomaterials to Potentiate Cancer Thermal Therapy. *Chemical Reviews* **2023,** *123* (11), 7326-7378.
31. Kok, H. P.; Cressman, E. N. K.; Ceelen, W.; Brace, C. L.; Ivkov, R.; Grüll, H.; ter Haar, G.; Wust, P.; Crezee, J., Heating technology for malignant tumors: a review. *International Journal of Hyperthermia* **2020,** *37* (1), 711-741.
32. Salomir, R.; Vimeux, F. C.; de Zwart, J. A.; Grenier, N.; Moonen, C. T., Hyperthermia by MR-guided focused ultrasound: accurate temperature control based on fast MRI and a

physical model of local energy deposition and heat conduction. *Magn Reson Med* **2000,** *43* (3), 342-7.

33. Quesson, B.; Vimeux, F.; Salomir, R.; de Zwart, J. A.; Moonen, C. T., Automatic control of hyperthermic therapy based on real-time Fourier analysis of MR temperature maps. *Magn Reson Med* **2002,** *47* (6), 1065-72.
34. Tillander, M.; Hokland, S.; Koskela, J.; Dam, H.; Andersen, N. P.; Pedersen, M.; Tanderup, K.; Ylihautala, M.; Köhler, M., High intensity focused ultrasound induced in vivo large volume hyperthermia under 3D MRI temperature control. *Med Phys* **2016,** *43* (3), 1539-49.
35. Zhu, L.; Altman, M. B.; Laszlo, A.; Straube, W.; Zoberi, I.; Hallahan, D. E.; Chen, H., Ultrasound Hyperthermia Technology for Radiosensitization. *Ultrasound Med Biol* **2019,** *45* (5), 1025-1043.
36. Diederich, C. J.; Hynynen, K., Ultrasound technology for hyperthermia. *Ultrasound Med Biol* **1999,** *25* (6), 871-87.
37. Rybak, L. D., Fire and ice: thermal ablation of musculoskeletal tumors. *Radiologic Clinics of North America* **2009,** *47* (3), 455-469.
38. Pearce, J.; Giustini, A.; Stigliano, R.; Jack Hoopes, P., Magnetic Heating of Nanoparticles: The Importance of Particle Clustering to Achieve Therapeutic Temperatures. *Journal of Nanotechnology in Engineering and Medicine* **2013,** *4* (1), 011005-1.
39. Hervault, A.; Thanh, N. T. K., Magnetic nanoparticle-based therapeutic agents for thermo-chemotherapy treatment of cancer. *Nanoscale* **2014,** *6* (20), 11553-11573.
40. Gossuin, Y.; Gillis, P.; Hocq, A.; Vuong, Q. L.; Roch, A., Magnetic resonance relaxation properties of superparamagnetic particles. *WIREs Nanomedicine and Nanobiotechnology* **2009,** *1* (3), 299-310.
41. Liu, D.; Yang, W.; Zhang, B., Magnetic Resonance Imaging and Its Molecular Probes in Evaluating the Response to Tumor Treatment. *Nano Biomedicine and Engineering* **2024,** *17* (1), 36-55.
42. Gazeau, F.; Lévy, M.; Wilhelm, C., Optimizing magnetic nanoparticle design for nanothermotherapy. *Nanomedicine (Lond)* **2008,** *3* (6), 831-44.
43. Cazares-Cortes, E.; Cabana, S.; Boitard, C.; Nehlig, E.; Griffete, N.; Fresnais, J.; Wilhelm, C.; Abou-Hassan, A.; Ménager, C., Recent insights in magnetic hyperthermia: From the "hot-spot" effect for local delivery to combined magneto-photo-thermia using magneto-plasmonic hybrids. *Advanced Drug Delivery Reviews* **2019,** *138*, 233-246.
44. Suriyanto; Ng, E. Y. K.; Kumar, S. D., Physical mechanism and modeling of heat generation and transfer in magnetic fluid hyperthermia through Néelian and Brownian relaxation: a review. *BioMedical Engineering OnLine* **2017,** *16* (1), 36.
45. Cullity, B. D.; Graham, C. D., *Introduction to magnetic materials*. John Wiley & Sons: 2011.
46. Kolhatkar, A. G.; Jamison, A. C.; Litvinov, D.; Willson, R. C.; Lee, T. R., Tuning the Magnetic Properties of Nanoparticles. *International Journal of Molecular Sciences* **2013,** *14* (8), 15977-16009.
47. Gavilán, H.; Avugadda, S. K.; Fernández-Cabada, T.; Soni, N.; Cassani, M.; Mai, B. T.; Chantrell, R.; Pellegrino, T., Magnetic nanoparticles and clusters for magnetic hyperthermia: optimizing their heat performance and developing combinatorial therapies to tackle cancer. *Chemical Society Reviews* **2021,** *50* (20), 11614-11667.

48. Goya, G. F.; Grazu, V.; Ibarra, M. R., Magnetic Nanoparticles for Cancer Therapy. *Current Nanoscience* **2008,** *4* (1), 1-16.

49. Ruta, S.; Chantrell, R.; Hovorka, O., Unified model of hyperthermia via hysteresis heating in systems of interacting magnetic nanoparticles. *Scientific Reports* **2015,** *5* (1), 9090.

50. Skumryev, V.; Stoyanov, S.; Zhang, Y.; Hadjipanayis, G.; Givord, D.; Nogués, J., Beating the superparamagnetic limit with exchange bias. *nature* **2003,** *423* (6942), 850-853.

51. Debye, P. J. W., *Polar molecules*. Dover publications: 1929.

52. Kötitz, R.; Weitschies, W.; Trahms, L.; Semmler, W., Investigation of Brownian and Néel relaxation in magnetic fluids. *Journal of Magnetism and Magnetic Materials* **1999,** *201* (1), 102-104.

53. Pankhurst, Q. A.; Connolly, J.; Jones, S. K.; Dobson, J., Applications of magnetic nanoparticles in biomedicine. *Journal of Physics D: Applied Physics* **2003,** *36* (13), R167-181.

54. Rosensweig, R. E., Heating magnetic fluid with alternating magnetic field. *Journal of Magnetism and Magnetic Materials* **2002,** *252*, 370-374.

55. Sathya, A.; Guardia, P.; Brescia, R.; Silvestri, N.; Pugliese, G.; Nitti, S.; Manna, L.; Pellegrino, T., CoxFe3–xO4 Nanocubes for Theranostic Applications: Effect of Cobalt Content and Particle Size. *Chemistry of Materials* **2016,** *28* (6), 1769-1780.

56. Guardia, P.; Nitti, S.; Materia, M. E.; Pugliese, G.; Yaacoub, N.; Greneche, J. M.; Lefevre, C.; Manna, L.; Pellegrino, T., Gold–iron oxide dimers for magnetic hyperthermia: the key role of chloride ions in the synthesis to boost the heating efficiency. *Journal of Materials Chemistry B* **2017,** *5* (24), 4587-4594.

57. Fortin, J.-P.; Wilhelm, C.; Servais, J.; Ménager, C.; Bacri, J.-C.; Gazeau, F., Size-Sorted Anionic Iron Oxide Nanomagnets as Colloidal Mediators for Magnetic Hyperthermia. *Journal of the American Chemical Society* **2007,** *129* (9), 2628-2635.

58. Mehdaoui, B.; Meffre, A.; Carrey, J.; Lachaize, S.; Lacroix, L.-M.; Gougeon, M.; Chaudret, B.; Respaud, M., Optimal Size of Nanoparticles for Magnetic Hyperthermia: A Combined Theoretical and Experimental Study. *Advanced Functional Materials* **2011,** *21* (23), 4573-4581.

59. Gehrke, N.; Briel, A.; Ludwig, F.; Remmer, H.; Wawrzik, T.; Wellert, S. In *New Perspectives for MPI: A Toolbox for Tracer Research*, Magnetic Particle Imaging, Berlin, Heidelberg, 2012//; Buzug, T. M.; Borgert, J., Eds. Springer Berlin Heidelberg: Berlin, Heidelberg, 2012; pp 99-103.

60. Shavel, A.; Liz-Marzán, L. M., Shape control of iron oxide nanoparticles. *Physical Chemistry Chemical Physics* **2009,** *11* (19), 3762-3766.

61. Ai, H.; Flask, C.; Weinberg, B.; Shuai, X.-T.; Pagel, M. D.; Farrell, D.; Duerk, J.; Gao, J., Magnetite-Loaded Polymeric Micelles as Ultrasensitive Magnetic-Resonance Probes. *Advanced Materials* **2005,** *17* (16), 1949-1952.

62. Sun, S.; Zeng, H.; Robinson, D. B.; Raoux, S.; Rice, P. M.; Wang, S. X.; Li, G., Monodisperse MFe2O4 (M = Fe, Co, Mn) Nanoparticles. *Journal of the American Chemical Society* **2004,** *126* (1), 273-279.

63. Salazar-Alvarez, G.; Qin, J.; Šepelák, V.; Bergmann, I.; Vasilakaki, M.; Trohidou, K. N.; Ardisson, J. D.; Macedo, W. A. A.; Mikhaylova, M.; Muhammed, M.; Baró, M. D.; Nogués, J., Cubic versus Spherical Magnetic Nanoparticles: The Role of Surface Anisotropy. *Journal of the American Chemical Society* **2008,** *130* (40), 13234-13239.

64. Jang, J.-t.; Nah, H.; Lee, J.-H.; Moon, S. H.; Kim, M. G.; Cheon, J., Critical Enhancements of MRI Contrast and Hyperthermic Effects by Dopant-Controlled Magnetic Nanoparticles. *Angewandte Chemie International Edition* **2009,** *48* (7), 1234-1238.

65. Vita, F.; Innocenti, C.; Secchi, A.; Albertini, F.; Grillo, V.; Fiore, A.; Cozzoli, P. D.; Fernandez, C. d. J., Colloidal Au/iron oxide nanocrystal heterostructures: magnetic, plasmonic and magnetic hyperthermia properties. *Journal of Materials Chemistry C* **2018,** *6* (45), 12329-12340.

66. Park, S. Y.; Perikamana, S. K. M.; Park, J. H.; Kim, S. W.; Shin, H.; Park, S. P.; Jung, H. S., Osteoinductive superparamagnetic Fe nanocrystal/calcium phosphate heterostructured microspheres. *Nanoscale* **2017,** *9* (48), 19145-19153.

67. Chen, B.-W.; Hatamie, S.; Chiu, H.-C.; Wei, Z.-H.; Hu, S.-H.; Yao, D.-J., Shape-Mediated Magnetocrystalline Anisotropy and Relaxation Controls by Cobalt Ferrite Core-Shell Heterostructures for Magnetothermal Penetration Delivery. *Advanced Materials Interfaces* **2022,** *9* (12), 2200022.

68. Lee, J.-H.; Jang, J.-t.; Choi, J.-s.; Moon, S. H.; Noh, S.-h.; Kim, J.-w.; Kim, J.-G.; Kim, I.-S.; Park, K. I.; Cheon, J., Exchange-coupled magnetic nanoparticles for efficient heat induction. *Nature Nanotechnology* **2011,** *6* (7), 418-422.

69. Bordet, A.; Landis, R. F.; Lee, Y.; Tonga, G. Y.; Asensio, J. M.; Li, C.-H.; Fazzini, P.-F.; Soulantica, K.; Rotello, V. M.; Chaudret, B., Water-Dispersible and Biocompatible Iron Carbide Nanoparticles with High Specific Absorption Rate. *ACS Nano* **2019,** *13* (3), 2870-2878.

70. Gutiérrez, L.; de la Cueva, L.; Moros, M.; Mazarío, E.; de Bernardo, S.; de la Fuente, J. M.; Morales, M. P.; Salas, G., Aggregation effects on the magnetic properties of iron oxide colloids. *Nanotechnology* **2019,** *30* (11), 112001.

71. Gavilán, H.; Sánchez, E. H.; Brollo, M. E. F.; Asín, L.; Moerner, K. K.; Frandsen, C.; Lázaro, F. J.; Serna, C. J.; Veintemillas-Verdaguer, S.; Morales, M. P.; Gutiérrez, L., Formation Mechanism of Maghemite Nanoflowers Synthesized by a Polyol-Mediated Process. *ACS Omega* **2017,** *2* (10), 7172-7184.

72. Haase, C.; Nowak, U., Role of dipole-dipole interactions for hyperthermia heating of magnetic nanoparticle ensembles. *Physical Review B* **2012,** *85* (4), 045435.

73. Wahajuddin; Arora, S., Superparamagnetic iron oxide nanoparticles: magnetic nanoplatforms as drug carriers. *Int J Nanomedicine* **2012,** *7*, 3445-71.

74. Guibert, C.; Dupuis, V.; Peyre, V.; Fresnais, J., Hyperthermia of Magnetic Nanoparticles: Experimental Study of the Role of Aggregation. *The Journal of Physical Chemistry C* **2015,** *119* (50), 28148-28154.

75. Fu, R.; Yan, Y.; Roberts, C.; Liu, Z.; Chen, Y., The role of dipole interactions in hyperthermia heating colloidal clusters of densely-packed superparamagnetic nanoparticles. *Scientific Reports* **2018,** *8* (1), 4704.

76. Du, Y.; Liu, X.; Liang, Q.; Liang, X.-J.; Tian, J., Optimization and Design of Magnetic Ferrite Nanoparticles with Uniform Tumor Distribution for Highly Sensitive MRI/MPI Performance and Improved Magnetic Hyperthermia Therapy. *Nano Letters* **2019,** *19* (6), 3618-3626.

77. Song, G.; Kenney, M.; Chen, Y.-S.; Zheng, X.; Deng, Y.; Chen, Z.; Wang, S. X.; Gambhir, S. S.; Dai, H.; Rao, J., Carbon-coated FeCo nanoparticles as sensitive magnetic-particle-imaging tracers with photothermal and magnetothermal properties. *Nature Biomedical Engineering* **2020,** *4* (3), 325.

78. Tay, Z. W.; Chandrasekharan, P.; Chiu-Lam, A.; Hensley, D. W.; Dhavalikar, R.; Zhou, X. Y.; Yu, E. Y.; Goodwill, P. W.; Zheng, B.; Rinaldi, C.; Conolly, S. M., Magnetic Particle Imaging-Guided Heating in Vivo Using Gradient Fields for Arbitrary Localization of Magnetic Hyperthermia Therapy. *Acs Nano* **2018,** *12* (4), 3699-3713.

79. Curcio, A.; Silva, A. K. A.; Cabana, S.; Espinosa, A.; Baptiste, B.; Menguy, N.; Wilhelm, C.; Abou-Hassan, A., Iron Oxide Nanoflowers @ CuS Hybrids for Cancer Tri-Therapy: Interplay of Photothermal Therapy, Magnetic Hyperthermia and Photodynamic Therapy. *Theranostics* **2019,** *9* (5), 1288-1302.

80. Ma, X.; Wang, Y.; Liu, X.-L.; Ma, H.; Li, G.; Li, Y.; Gao, F.; Peng, M.; Fan, H. M.; Liang, X.-J., Fe3O4-Pd Janus nanoparticles with amplified dual-mode hyperthermia and enhanced ROS generation for breast cancer treatment. *Nanoscale Horizons* **2019,** *4* (6), 1450-1459.

81. Rocha, G. N. d. S. A. O.; Silva, J. Y. R.; Santos, D. K. D. d. N.; Pereira, A. C. M. V.; Rocha, J. V. R.; Alves, C. d. S. C.; Almeida, J. R. G. d. S.; Gomes, A. S. L.; Bakuzis, A. F.; Alves Junior, S., Design of a magnetic nanocarrier containing phyllacanthone as delivery of anticancer phytochemical: Characterization and theranostic in vitro applications. *Journal of Alloys and Compounds* **2025,** *1010*, 117860.

82. Lu, D.; Chen, M.; Yu, L.; Chen, Z.; Guo, H.; Zhang, Y.; Han, Z.; Xu, T.; Wang, H.; Zhou, X.; Zhou, Z.; Teng, G., Smart-Polypeptide-Coated Mesoporous Fe3O4 Nanoparticles: Non-Interventional Target-Embolization/Thermal Ablation and Multimodal Imaging Combination Theranostics for Solid Tumors. *Nano Letters* **2021,** *21* (24), 10267-10278.

83. Ince, I.; Muftuler, Z. B.; Medine, E. I.; Guldu, O. K.; Takan, G.; Ergonul, A.; Parlak, Y.; Yildirim, Y.; Cakar, B.; Bilgin, E. S.; Aras, O.; Goker, E.; Unak, P., Thymoquinone Glucuronide Conjugated Magnetic Nanoparticle for Bimodal Imaging and Treatment of Cancer as a Novel Theranostic Platform. *Current Radiopharmaceuticals* **2021,** *14* (1), 23-36.

84. Dutta, B.; Shetake, N. G.; Patra, S.; Chakravarty, R.; Vimalnath, K. V.; Chakraborty, A.; Chakraborty, S.; Pandey, B. N.; Hassan, P. A.; Barick, K. C., pH-Responsive magnetic nanocarriers for chelator-free bimodal (MRI/SPECT-CT) image-guided chemo-hyperthermia therapy in human breast carcinoma. *Journal of Materials Chemistry B* **2024,** *12* (45), 11759-11777.

85. Patrick, P. S.; Stuckey, D. J.; Zhu, H.; Kalber, T. L.; Iftikhar, H.; Southern, P.; Bear, J. C.; Lythgoe, M. F.; Hattersley, S. R.; Pankhurst, Q. A., Improved tumour delivery of iron oxide nanoparticles for magnetic hyperthermia therapy of melanoma via ultrasound guidance and 111In SPECT quantification. *Nanoscale* **2024,** *16* (42), 19715-19729.

86. Ha, P. T.; Le, T. T. H.; Ung, T. D. T.; Do, H. D.; Doan, B. T.; Mai, T. T. T.; Pham, H. N.; Hoang, T. M. N.; Phan, K. S.; Bui, T. Q., Properties and bioeffects of magneto-near infrared nanoparticles on cancer diagnosis and treatment. *New Journal of Chemistry* **2020,** *44* (40), 17277-17288.

87. Mansur, A. A. P.; Carvalho, S. M.; Lobato, Z. I. P.; Leite, M. F.; Krambrock, K.; Mansur, H. S., Bioengineering stimuli-responsive organic-inorganic nanoarchitetures based on carboxymethylcellulose-poly-L-lysine nanoplexes: Unlocking the potential for bioimaging and multimodal chemodynamic-magnetothermal therapy of brain cancer cells. *International Journal of Biological Macromolecules* **2025,** *290*, 138985.

88. Yang, F.; Skripka, A.; Tabatabaei, M. S.; Hong, S. H.; Ren, F.; Benayas, A.; Oh, J. K.; Martel, S.; Liu, X.; Vetrone, F.; Ma, D., Multifunctional Self-Assembled Supernanoparticles for Deep-Tissue Bimodal Imaging and Amplified Dual-Mode Heating Treatment. *Acs Nano* **2019,** *13* (1), 408-420.

89. Das, A.; Meena, R.; Kumar, R.; Kuanr, B. K., Sensitizer-Passivated Magnetic Ferrite/Eu3+-Doped Oxide Nanocomposite: A Novel Luminescent Probe for Facile Bioimaging with Superior Magnetic Hyperthermia Performance. *Acs Applied Materials & Interfaces* **2025,** *17* (14), 20872-20884.

90. Nguyen Thanh, H.; Nguyen Manh, H.; Pham Thi, L.; Nguyen Duc, V.; Pham Hong, N.; Nguyen Thanh, B.; Le Quoc, M., Fabrication and Characterization of Luminescent Magnetic Bifunctional Nanocomposite Based on TbPO4•H2O Nanowires and Fe3O4 Nanoparticles. *Journal of Electronic Materials* **2016,** *45* (7), 3646-3650.

91. Phan, K. S.; Doan, B. T.; Wang, Y.; Le, T. T. H.; Mai, T. T. T.; Pham, H. N.; Bui, H. B. H.; Dang, L. H.; Tran, N. Q.; Ha, P. T., Harnessing for quantitative MRI, bioluminescence, chemo-magnetic hyperthermia, and near-infrared optical imaging of a magnetic nanotheranostic for in vivo passive targeted monitoring in colorectal cancer models. *Biomaterials Science* **2025,** *13* (19), 5402-5421.

92. Sheng, Y.; Li, S.; Duan, Z.; Zhang, R.; Xue, J., Fluorescent magnetic nanoparticles as minimally-invasive multi-functional theranostic platform for fluorescence imaging, MRI and magnetic hyperthermia. *Materials Chemistry and Physics* **2018,** *204*, 388-396.

93. Yan, H.; Shang, W.; Sun, X.; Zhao, L.; Wang, J.; Xiong, Z.; Yuan, J.; Zhang, R.; Huang, Q.; Wang, K.; Li, B.; Tian, J.; Kang, F.; Feng, S.-S., "All-in-One" Nanoparticles for Trimodality Imaging-Guided Intracellular Photo-magnetic Hyperthermia Therapy under Intravenous Administration. *Advanced Functional Materials* **2018,** *28* (9), 1705710.

94. Perton, F.; Tasso, M.; Munoz Medina, G. A.; Menard, M.; Blanco-Andujar, C.; Portiansky, E.; Fernandez van Raap, M. B.; Begin, D.; Meyer, F.; Begin-Colin, S.; Mertz, D., Fluorescent and magnetic stellate mesoporous silica for bimodal imaging and magnetic hyperthermia. *Applied Materials Today* **2019,** *16*, 301-314.

95. Ying, W.; Zhang, Y.; Gao, W.; Cai, X.; Wang, G.; Wu, X.; Chen, L.; Meng, Z.; Zheng, Y.; Hu, B.; Lin, X., Hollow Magnetic Nanocatalysts Drive Starvation-Chemodynamic-Hyperthermia Synergistic Therapy for Tumor. *Acs Nano* **2020,** *14* (8), 9662-9674.

96. Du, W.; Liu, T.; Xue, F.; Cai, X.; Chen, Q.; Zheng, Y.; Chen, H., Fe3O4 Mesocrystals with Distinctive Magnetothermal and Nanoenzyme Activity Enabling Self-Reinforcing Synergistic Cancer Therapy. *Acs Applied Materials & Interfaces* **2020,** *12* (17), 19285-19294.

97. Shen, J.; Rees, T. W.; Zhou, Z.; Yang, S.; Ji, L.; Chao, H., A mitochondria-targeting magnetothermogenic nanozyme for magnet-induced synergistic cancer therapy. *Biomaterials* **2020,** *251*, 120079.

98. Lopez-Mendez, R.; Lafuente-Gomez, N.; Cespedes, E.; Dhanjani, M.; Paris-Ogayar, M.; Jose Teran, F.; Serrano, A.; Camarero, J.; Salas, G.; Wilhelm, C.; Somoza, A.; Espinosa, A., Tri-Modal Anticancer Strategies with Doxorubicin-Loaded Iron Oxide Nanoparticles Integrating Chemo and Magneto-Photothermal Therapeutic Effects. *Advanced Nanobiomed Research* **2025**, 2500098.

99. Zhang, W.; Sun, D.; Yang, B.; Liu, J.; Yuan, Y.; Li, D.; Sun, Y.; Guan, G.; Liu, Y.; Wu, D.; Liao, H.; Lin, J.; Hu, J., Progressive-composition-transformation-induced enhanced hyperthermia-based nanozyme towards long-lasting and complete therapy of cancer. *Chemical Engineering Journal* **2025,** *507*, 160645.

100. Espinosa, A.; Di Corato, R.; Kolosnjaj-Tabi, J.; Flaud, P.; Pellegrino, T.; Wilhelm, C., Duality of Iron Oxide Nanoparticles in Cancer Therapy: Amplification of Heating Efficiency

by Magnetic Hyperthermia and Photothermal Bimodal Treatment. *Acs Nano* **2016,** *10* (2), 2436-2446.

101. Lu, Q.; Dai, X.; Zhang, P.; Tan, X.; Zhong, Y.; Yao, C.; Song, M.; Song, G.; Zhang, Z.; Peng, G.; Guo, Z.; Ge, Y.; Zhang, K.; Li, Y., Fe3O4@Au composite magnetic nanoparticles modified with cetuximab for targeted magneto-photothermal therapy of glioma cells. *International Journal of Nanomedicine* **2018,** *13*, 2491-2505.
102. Fagundes, D. A.; Leonel, L. V.; Fernandez-Outon, L. E.; Ardisson, J. D.; dos Santos, R. G., Radiosensitization Induced by Magnetic Hyperthermia of PEGylated Nickel Ferrite Nanoparticles on Breast Cancer Cells. *International Journal of Molecular Sciences* **2025,** *26* (6), 2706.
103. Heo, D.; Lokeshwar, B. L.; Barrett, J. T.; Mostafaei, F.; Kwon, S.-H.; Huh, C., Quantitative analysis of radiosensitizing effect for magnetic hyperthermia-radiation combined therapy on prostate cancer cells. *Medical Physics* **2024,** *51* (10), 7606-7618.
104. Mirzaghavami, P. S.; Khoei, S.; Khoee, S.; Shirvalilou, S.; Mahdavi, S. R.; Mahabadi, V. P., Radio-sensitivity enhancement in HT29 cells through magnetic hyperthermia in combination with targeted nano-carrier of 5-Flourouracil. *Materials Science & Engineering C-Materials for Biological Applications* **2021,** *124*, 112043.
105. Ognjanovic, M.; Boskovic, M.; Stanojkovic, T.; Dojcinovic, B. P.; Abeykoon, A. M. M.; Tomic, A.; Jankovic, D.; Vranjes-Duric, S.; Bozin, E. S.; Antic, B. V., From Structure to Function: Zn/Mn-Modified Maghemite as an Advanced Nanoplatform for Magnetic Hyperthermia and Radionuclide Therapy. *Acs Applied Materials & Interfaces* **2025,** *17* (33), 46836-46849.
106. Zuk, M.; Podgorski, R.; Ruszczynska, A.; Ciach, T.; Majkowska-Pilip, A.; Bilewicz, A.; Krysinski, P., Multifunctional Nanoparticles Based on Iron Oxide and Gold-198 Designed for Magnetic Hyperthermia and Radionuclide Therapy as a Potential Tool for Combined HER2-Positive Cancer Treatment. *Pharmaceutics* **2022,** *14* (8), 1680.
107. Vukadinovic, A.; Milanovic, Z.; Ognjanovic, M.; Jankovic, D.; Radovic, M.; Mirkovic, M.; Karageorgou, M.-A.; Bouziotis, P.; Eric, S.; Vranjes-Duric, S.; Antic, B.; Prijovic, Z., 90Y-CA/SPIONs for dual magnetic hyperthermia-radionuclide nanobrachytherapy of solid tumours. *Nanotechnology* **2022,** *33* (40), 405102.
108. Thirumurugan, S.; Muthiah, K. S.; Lin, Y.-C.; Dhawan, U.; Liu, W.-C.; Wang, A.-N.; Liu, X.; Hsiao, M.; Tseng, C.-L.; Chung, R.-J., NIR-Responsive Methotrexate-Modified Iron Selenide Nanorods for Synergistic Magnetic Hyperthermic, Photothermal, and Chemodynamic Therapy. *Acs Applied Materials & Interfaces* **2024,** *16* (20), 25622-25636.
109. Zhang, Q.; Liu, J.; Yuan, K.; Zhang, Z.; Zhang, X.; Fang, X., A multi-controlled drug delivery system based on magnetic mesoporous Fe3O4 nanopaticles and a phase change material for cancer thermo-chemotherapy. *Nanotechnology* **2017,** *28* (40), 405101.
110. Benyettou, F.; Flores, J. A. O.; Ravaux, F.; Rezgui, R.; Jouiad, M.; Nehme, S. I.; Parsapur, R. K.; Olsen, J.-C.; Selvam, P.; Trabolsi, A., Mesoporous γ-Iron Oxide Nanoparticles for Magnetically Triggered Release of Doxorubicin and Hyperthermia Treatment. *Chemistry-a European Journal* **2016,** *22* (47), 17018-17026.
111. Garcia-Soriano, D.; Milan-Rois, P.; Lafuente-Gomez, N.; Rodriguez-Diaz, C.; Navio, C.; Somoza, A.; Salas, G., Multicore iron oxide nanoparticles for magnetic hyperthermia and combination therapy against cancer cells. *Journal of Colloid and Interface Science* **2024,** *670*, 73-85.

112. Farzaneh, M.; Hassanzadeh-Tabrizi, S. A.; Mokhtarian, N., Preparation of an Injectable Thermosensitive Pluronic F127/ γ-Fe2O3 Hydrogel for Combined Hyperthermia and Localized Drug Delivery for Cancer Treatment. *Polymers for Advanced Technologies* **2024,** *35* (11), e6616.

113. Fernandes, S.; Fernandez, T.; Metze, S.; Balakrishnan, P. B.; Mai, B. T.; Conteh, J.; De Mei, C.; Turdo, A.; Di Franco, S.; Stassi, G.; Todaro, M.; Pellegrino, T., Magnetic Nanoparticle-Based Hyperthermia Mediates Drug Delivery and Impairs the Tumorigenic Capacity of Quiescent Colorectal Cancer Stem Cells. *Acs Applied Materials & Interfaces* **2021,** *13* (14), 15959-15972.

114. Eskandani, M.; Jahanban-Esfahlan, R.; Sadughi, M. M.; Jaymand, M., Thermal-responsive β-cyclodextrin-based magnetic hydrogel as a de novo nanomedicine for chemo/hyperthermia treatment of cancerous cells. *Heliyon* **2024,** *10* (11), e32183.

115. Pradhan, L.; Thakur, B.; Srivastava, R.; Ray, P.; Bahadur, D., Assessing Therapeutic Potential of Magnetic Mesoporous Nanoassemblies for Chemo-Resistant Tumors. *Theranostics* **2016,** *6* (10), 1557-1572.

116. Wang, L.; Yan, Y.; Wang, M.; Yang, H.; Zhou, Z.; Peng, C.; Yang, S., An integrated nanoplatform for theranostics via multifunctional core-shell ferrite nanocubes. *Journal of Materials Chemistry B* **2016,** *4* (10), 1908-1914.

117. Li, X.; Wang, L.; Fan, Y.; Feng, Q.; Cui, F.-z., Biocompatibility and Toxicity of Nanoparticles and Nanotubes. *Journal of Nanomaterials* **2012,** *2012* (1), 548389.

118. Nikzamir, M.; Akbarzadeh, A.; Panahi, Y., An overview on nanoparticles used in biomedicine and their cytotoxicity. *Journal of Drug Delivery Science and Technology* **2021,** *61*, 102316.

119. Yaşayan, G.; Alarcin, E.; Avci-Adali, M.; Ipek, T. C.; Nejati, O.; Özcan-Bülbül, E.; Karslı, S.; Bal-Öztürk, A.; Mostafavi, E., Chapter 27 - Biocompatibility and toxicity challenges of nanomaterials. In *Functionalized Nanomaterials for Cancer Research*, Barabadi, H.; Mostafavi, E.; Mustansar Hussain, C., Eds. Academic Press: 2024; pp 603-631.

120. Souto, C. A. Z.; de Souza Junior, F. G.; da Silva, A. R.; Pal, K., Magnetite Nanoparticles Encapsulated with PBS-PEG for AMF Hyperthermia. *Materials* **2025,** *18* (2), 258.

121. Garcia-Garcia, G.; Lazaro, M.; Urquiza, P.; Romacho, T.; Delgado, a. V.; Iglesias, G. R., Polydopamine Coated Nonspherical Magnetic Nanocluster for Synergistic Dual Magneto-Photothermal Cancer Therapy. *Polymers* **2025,** *17* (1), 85.

122. Tzavara, D.; Papadia, K.; Kolokithas-Ntoukas, A.; Antimisiaris, S. G.; Skouras, A., Engineered PAM-SPION Nanoclusters for Enhanced Cancer Therapy: Integrating Magnetic Targeting with pH-Responsive Drug Release. *Molecules* **2025,** *30* (13), 2785.

123. Mohan, A.; Suresh, R.; Ashwini, M.; Periyasami, G.; Guganathan, L.; Lin, M.-C.; Kumarasamy, K.; Kim, S.-C.; Santhamoorthy, M., Alginate functionalized magnetic-silica composites for pH-responsive drug delivery and magnetic hyperthermia applications. *Materials Letters* **2024,** *361*, 136088

124. Do, X.-H.; Nguyen, T. D.; Le, T. T. H.; To, T. T.; Bui, T. V. K.; Pham, N. H.; Lam, K.; Hoang, T. M. N.; Ha, P. T., High Biocompatibility, MRI Enhancement, and Dual Chemo- and Thermal-Therapy of Curcumin-Encapsulated Alginate/Fe3O4 Nanoparticles. *Pharmaceutics* **2023,** *15* (5), 1523.

125. Negri, A.; Conti, A.; Milan, E.; Forlin, E.; Gherlinzoni, F.; Morana, G.; Gottardi, M.; Matteazzi, P.; Speghini, A.; Bongers, A.; Marzola, P., Evaluation of Self-Regulating Doped Ferrite Nanoparticles with Glucose, Chitosan, and Poly-Ethylene Glycol Coatings for Hyperthermia and Dual. *International Journal of Nanomedicine* **2025,** *20*, 3891-3906.

126. Gogoi, M.; Jaiswal, M. K.; Sarma, H. D.; Bahadur, D.; Banerjee, R., Biocompatibility and therapeutic evaluation of magnetic liposomes designed for self-controlled cancer hyperthermia and chemotherapy. *Integrative Biology* **2017,** *9* (6), 555-565.

127. Patil-Sen, Y.; Torino, E.; De Sarno, F.; Ponsiglione, A. M.; Chhabria, V.; Ahmed, W.; Mercer, T., Biocompatible superparamagnetic core-shell nanoparticles for potential use in hyperthermia-enabled drug release and as an enhanced contrast agent. *Nanotechnology* **2020,** *31* (37), 375102.

128. Magdolenova, Z.; Drlickova, M.; Henjum, K.; Runden-Pran, E.; Tulinska, J.; Bilanicova, D.; Pojana, G.; Kazimirova, A.; Barancokova, M.; Kuricova, M.; Liskova, A.; Staruchova, M.; Ciampor, F.; Vavra, I.; Lorenzo, Y.; Collins, A.; Rinna, A.; Fjellsbo, L.; Volkovova, K.; Marcomini, A.; Amiry-Moghaddam, M.; Dusinska, M., Coating-dependent induction of cytotoxicity and genotoxicity of iron oxide nanoparticles. *NANOTOXICOLOGY* **2015,** *9*, 44-56.

129. Egbuna, C.; Parmar, V. K.; Jeevanandam, J.; Ezzat, S. M.; Patrick-Iwuanyanwu, K. C.; Adetunji, C. O.; Khan, J.; Onyeike, E. N.; Uche, C. Z.; Akram, M.; Ibrahim, M. S.; El Mahdy, N. M.; Awuchi, C. G.; Saravanan, K.; Tijjani, H.; Odoh, U. E.; Messaoudi, M.; Ifemeje, J. C.; Olisah, M. C.; Ezeofor, N. J.; Chikwendu, C. J.; Ibeabuchi, C. G., Toxicity of Nanoparticles in Biomedical Application: Nanotoxicology. *J Toxicol* **2021,** *2021*, 9954443.

130. Jia, Q.; Han, X.; Liu, Y.; Liao, X.; Zhou, J., Tumor–microenvironment activated programmable synergistic cancer therapy by bioresponsive rare-earth nanocomposite. *Journal of Rare Earths* **2022,** *40* (9), 1399-1406.

131. Udupi, A.; Shetty, S.; Aranjani, J. M.; Kumar, R.; Bharati, S., Anticancer therapeutic potential of multimodal targeting agent- "phosphorylated galactosylated chitosan coated magnetic nanoparticles" against N-nitrosodiethylamine-induced hepatocellular carcinoma. *Drug Delivery and Translational Research* **2025,** *15* (3), 1023-1042.

132. Yahya, S.; Pushpanathan, S.; Jan, S.; Chaudhary, N.; Parray, R.; Gandhi, K. A.; Thangavel, K.; Krishnan, K.; Sudhandiran, G., Development and characterization of pegylated Fe3O4-CAPE magnetic nanoparticles for targeted therapy and hyperthermia treatment of colorectal cancer. *Scientific Reports* **2025,** *15* (1), 26008.

133. Zong, Y.; He, J.; Wu, Y.; Qin, J.; Zhao, M.; Zhu, X.; Xie, J.; Yin, H., Multi-Functional Magnetic Nanocrystals for Tumor Mitochondria-Targeted Magnetic Hyperthermia Combined with Enhanced Radiotherapy. *International Journal of Nanomedicine* **2025,** *20*, 11127-11150.

134. Maier-Hauff, K.; Ulrich, F.; Nestler, D.; Niehoff, H.; Wust, P.; Thiesen, B.; Orawa, H.; Budach, V.; Jordan, A., Efficacy and safety of intratumoral thermotherapy using magnetic iron-oxide nanoparticles combined with external beam radiotherapy on patients with recurrent glioblastoma multiforme. *Journal of Neuro-Oncology* **2011,** *103* (2), 317-324.

135. Singh, A.; Kumar, N., Estimation of the injection criteria for magnetic hyperthermia therapy based on tumor morphology. *Biomed Phys Eng Express* **2024,** *10* (5), 055017.

136. Fatigate, G. R.; Martins, G. C.; Lobosco, M.; Reis, R. F., Impact of inaccuracies of injection positioning for hyperthermia treatment for cancer. *Journal of Computational and Applied Mathematics* **2026,** *472*, 116780.

137. Boedtkjer, E.; Pedersen, S. F., The Acidic Tumor Microenvironment as a Driver of Cancer. *Annual Review of Physiology* **2020,** *82* (Volume 82, 2020), 103-126.

138. Corbet, C.; Feron, O., Tumour acidosis: from the passenger to the driver's seat. *Nature Reviews Cancer* **2017,** *17* (10), 577-593.

139. Feng, Q.; Bennett, Z.; Grichuk, A.; Pantoja, R.; Huang, T.; Faubert, B.; Huang, G.; Chen, M.; DeBerardinis, R. J.; Sumer, B. D.; Gao, J., Severely polarized extracellular acidity around tumour cells. *Nature Biomedical Engineering* **2024,** *8* (6), 787-799.

140. Park, Y.; Jeong, E. M., Glutathione Dynamics in the Tumor Microenvironment: A Potential Target of Cancer Stem Cells and T Cells. *Int J Stem Cells* **2024,** *17* (3), 270-283.

141. Wang, Y.; He, J.; Feng, R.; Chen, J.; Xie, G.; Yu, S.; Wu, Y. X.; Tang, K., Lighting up endogenous H(2)O(2) in the tumor microenvironment using a dual-mode nanoprobe for long afterglow and MR bioimaging. *Analyst* **2024,** *149* (16), 4230-4238.

142. Cai, W. L.; Zhang, W.; Chen, Z. L., Magnetic Fe3O4@ZIF-8 nanoparticles as a drug release vehicle: pH-sensitive release of norfloxacin and its antibacterial activity. *Colloids and Surfaces B-Biointerfaces* **2023,** *223*, 113170.

143. Qiao, L.; Ou, Y.; Li, L.; Wu, S.; Guo, Y.; Liu, M.; Yu, D.; Chen, Q.; Yuan, J.; Wei, C.; Ou, C.; Li, H.; Cheng, D.; Yu, Z.; Li, Z., H(2)S-driven chemotherapy and mild photothermal therapy induced mitochondrial reprogramming to promote cuproptosis. *J Nanobiotechnology* **2024,** *22* (1), 205.

144. Wang, N.; Zeng, Q.; Zhang, R.; Xing, D.; Zhang, T., Eradication of solid tumors by chemodynamic theranostics with H(2)O(2)-catalyzed hydroxyl radical burst. *Theranostics* **2021,** *11* (5), 2334-2348.

145. Nagarajan, P.; Al-Najar, B.; Manoharan, R.; Bououdina, M.; Mohandas, M., Synergistic dual responsive chemo-hyperthermia anti-cancer treatment of Naringenin encapsulated nano vehicle for targeting non-small cell lung cancer. *Journal of Drug Delivery Science and Technology* **2025,** *109*, 106953.

146. Tavakoli, M.; Maghsoudian, S.; Rezaei-Aderiani, A.; Hajiramezanali, M.; Fatahi, Y.; Amani, M.; Sharifikolouei, E.; Ghahremani, M. H.; Raoufi, M.; Motasadizadeh, H.; Dinarvand, R., Synergistic effects of paclitaxel and platelet-superparamagnetic iron oxide nanoparticles for targeted chemo-hyperthermia therapy against breast cancer. *Colloids and Surfaces B-Biointerfaces* **2025,** *251*, 114584.

147. Bashir, A.; Khan, S.; Bashmal, S.; Iqbal, N.; Ullah, S.; Ali, L., Designing Highly Efficient Temperature Controller for Nanoparticles Hyperthermia. *Nanomaterials* **2022,** *12* (19), 3539.

148. Yamamoto, Y.; Itoh, T.; Irieda, T., A Heat Dissipation Study of Iron Oxide Nanoparticles Embedded an Agar Phantom for the Purpose of Magnetic Fluid Hyperthermia. *Journal of Nanoscience and Nanotechnology* **2019,** *19* (9), 5469-5475.

149. Vurro, F.; Gerosa, M.; Busato, A.; Muccilli, M.; Milan, E.; Gaudet, J.; Goodwill, P.; Mansfield, J.; Negri, A.; Gherlinzoni, F.; Morana, G.; Gottardi, M.; Matteazzi, P.; Wintermark, M.; Speghini, A.; Marzola, P., Doped Ferrite Nanoparticles Exhibiting Self-Regulating Temperature as Magnetic Fluid Hyperthermia Antitumoral Agents, with Diagnostic Capability in Magnetic Resonance Imaging and Magnetic Particle Imaging. *Cancers* **2022,** *14* (20), 5150.

150. Fatigate, G. R.; Lobosco, M.; Reis, R. F., A 3D Approach Using a Control Algorithm to Minimize the Effects on the Healthy Tissue in the Hyperthermia for Cancer Treatment. *Entropy* **2023,** *25* (4), 684.

151. Singh, A.; Kumar, N., Estimation of the injection criteria for magnetic hyperthermia therapy based on tumor morphology. *Biomedical Physics & Engineering Express* **2024,** *10* (5), 055017.

152. Montes-Robles, R.; Montanaro, H.; Capstick, M.; Ibanez-Civera, J.; Masot-Peris, R.; Garcia-Breijo, E.; Laguarda-Miro, N.; Martinez-Manez, R., Tailored cancer therapy by magnetic nanoparticle hyperthermia: A virtual scenario simulation method. *Computer Methods and Programs in Biomedicine* **2022,** *226*, 107185.

153. Hadadian, Y.; Kim, H.; Cao, T.-L.; Gong, J. E.; Ashfaq Ahmad, H.; Oh, S.; Umar Tahir, M.; Phu Bui, M.; Lee, Y.-S.; Kim, D.; Wiekhorst, F.; Kim, Y.-H.; Yoon, J., Tumor Size-Dependent Magnetic Hyperthermia Efficiency: A Simulation-Guided In Vivo Study. *Acs Applied Nano Materials* **2025,** *8* (34), 16643-16657.

154. Singh, G.; Kumar, N.; Avti, P. K., Computational evaluation of effectiveness for intratumoral injection strategies in magnetic nanoparticle assisted thermotherapy. *International Journal of Heat and Mass Transfer* **2020,** *148*, 119129.

155. Alamouti, A. K.; Raouf, I.; Zahabi, S.; Salimibani, M., Numerical study of magnetic nanoparticles injection into a brain tumor considering the effects of injection volume and location on the termination of cancerous cells. *Biointerphases* **2024,** *19* (6), 061005.

156. Shen, K.; Yan, Y.; Gao, W.; Li, L., Numerical simulation of the effect of injection sites arrangement on the thermal ablation in the magnetic fluid hyperthermia. *Journal of Magnetism and Magnetic Materials* **2022,** *555*, 169393.

157. Li, Z.; Lopez-Ortega, A.; Aranda-Ramos, A.; Luis Tajada, J.; Sort, J.; Nogues, C.; Vavassori, P.; Nogues, J.; Sepulveda, B., Simultaneous Local Heating/Thermometry Based on Plasmonic Magnetochromic Nanoheaters. *Small* **2018,** *14* (24), 1800868.

158. Li, D.; Jia, M.; Du, J.; Li, Y.; Jia, T.; Chen, G., Optomagnetic Heater-Thermometer Nanoplatform for Tumor Magnetothermal Therapy with Operando Temperature Feedback. *Acs Nano* **2025,** *19* (8), 8328-8337.

159. Rodrigues, H. F.; Capistrano, G.; Mello, F. M.; Zufelato, N.; Silveira-Lacerda, E.; Bakuzis, A. F., Precise determination of the heat delivery during in vivo magnetic nanoparticle hyperthermia with infrared thermography. *Physics in Medicine and Biology* **2017,** *62* (10), 4062-4082.

160. Hwang, J.; Seol, Y.; Oh, T.; An, N. Y.; Lee, J.; Kay, C.-S.; Jang, H. S.; Choi, B. O.; Kang, Y.-n., Evaluation of Developed Thermal Distribution Prediction Algorithm Using Mass Density Distribution with CT Image. *Journal of the Korean Physical Society* **2020,** *76* (1), 86-92.

161. Zuo, X.; Zhang, D.; Zhang, J.; Fang, T., Oxygen vacancy enhanced magnetic heating efficiency of ferrite nanoparticles for self-regulating temperature hyperthermia. *Ceramics International* **2023,** *49* (22), 36885-36893.

162. Valente-Rodrigues, C. L.; Caraballo-Vivas, R. J.; Santos, E. C. S.; Sharma, S. K.; Garcia, F., Investigation of Cr3+ doped Zn-Co nanoferrites as potential candidate for self-regulated magnetic hyperthermia applications. *Physica Scripta* **2023,** *98* (9), 095913.

163. Ahmad, A.; Bae, H.; Rhee, I., Silica-coated gadolinium-doped lanthanum strontium manganite nanoparticles for self-controlled hyperthermia applications. *Aip Advances* **2018,** *8* (1), 015108.

2 Enhancing Magnetic Hyperthermia Efficiency in Pd/Fe-oxide Hybrid Nanoparticles through Mn-Doping

Introduction

One of the most challenging innovations in medicine lies in multifunctional biocompatible nanoparticles (NPs) that can revolutionize cancer diagnosis and therapy.[1] Among various applied nanomaterials, magnetic nanoparticles (MNPs) are crucial for biomedical applications, such as drug delivery, cell marking, magnetic hyperthermia/thermal ablation (MH/TA), and magnetic resonance imaging (MRI).[2, 3] For example, one limitation of conventional MNPs in thermal treatments is their low heating capacity, expressed as specific loss power (SLP). This limitation requires the local injection of large quantities of MNPs.[1] Although toxicity is not necessarily a concern (FDA-approved magnetic iron oxide NPs (Ferumoxytol) are administered intravenously at doses as high as 510 mg for anemia treatment),[4] injecting large volumes directly into tumors remains a difficult task. Hence, to fully exploit the therapeutic potential of thermal treatments, it is crucial to design MNPs with high heating efficiency at clinically relevant doses (< 10 mg/kg). This would enable the generation of sufficient intratumoral and intralesional temperatures required for sensitization (40-44 °C) or the complete eradication (>60 °C) of cancer tissues.[2, 5] Furthermore, SLP requirements vary depending on the volume of tumors to be treated. In practice, this means that the concentration of the injected MNPs must be varied to achieve a certain therapeutic temperature increase.[6, 7] Therefore, optimization of the nanomaterials for MH/TA, while keeping an efficient heating power, has become a significant challenge in biomedicine. At the same time, optimized magnetic properties designed for thermal treatments may also lead to improved MRI performance, as both heating performance and contrast enhancement are directly related to saturation magnetization.[2, 8] These objectives can be achieved by tuning the MNPs parameters, such as size, shape and magnetocrystalline anisotropy.[1] Saturation magnetization (M_S) varies with the size of the MNPs until a threshold size is reached, beyond which the magnetization value plateaus and approaches the bulk magnetization value. Simultaneously, an increase in size alters the balance of magnetic interaction, causing the MNPs to transition from superparamagnetic to single-domain, and eventually, to multi-domain regimes.[8] Conveniently, the MNPs preferred in biomedical applications are sufficiently small to remain in the superparamagnetic regime, where magnetism disappears after removing an applied magnetic field, ensuring colloidal stability and resistance to aggregation.[9, 10] Additionally, it appears that MNPs with a size at the optimal threshold between superparamagnetic- and single-domain behavior are ideal for thermal treatment.[1, 11] Thus, tuning the efficiency of MNPs through size adjustments has limitations. On the other hand, tuning the anisotropy of the MNPs is a very promising alternative strategy to increase M_S leading to enhanced heating efficiency and relaxivities (r_i where i =1 and 2), which stands for relaxation rate enhancement per concentration of magnetic component - a parameter important for MRI.[1] Ways to influence the effective anisotropy of MNPs are via changes on shape anisotropy, or on magnetocrystalline anisotropy by doping or synthesizing core-shell MNPs.[12]

In the last years, ferrite nanoparticles with the general formula MFe_2O_4 (M = Fe, Mn, Co, Ni) have been in the spotlight due to their potential applications in biomedicine, and to their remarkable

magnetic properties, which can be modified by introducing the desired composition of the dopants.[13-15] An example is an increased saturation magnetization of $MnFe_2O_4$ NPs (110 emu/g) compared to Fe_3O_4 NPs of the same size (101 emu/g) due to magnetic engineering of the iron oxide nanocrystal by replacement of Fe^{2+} with Mn^{2+}.[16]

Lastly, the nanomedicine paradigm is shifting towards the development of therapeutic agents that can generate accompanying imaging signals. This advancement allows for the visualization of the drug delivery and distribution process, monitoring of therapy, and tracking the fate of NPs over time.[17] Iron oxide NPs are known for their ability to enhance the T_2 MRI contrast. When doped with paramagnetic ions, such as Mn^{2+}or Eu^{3+}, these MNPs may enable dual T_1/T_2 MRI contrast,[18] which is more desirable in certain clinical cases. While ultra-small Fe-oxide NPs (<10 nm) have been reported to also exhibit a T_1-effect,[19] achieving both high T_1 MRI performance and sufficient magnetization for MH/TA applications typically requires optimization strategies beyond mere size manipulations.[20] Therefore, engineering of magnetization values via the composition of MNPs is critical for developing sensitive magnetic probes for biomedical applications.[11]

In our previous work, we developed core-shell Pd/Fe-oxide NPs of 20 nm for MR-image assisted MH/TA applications combined with radiotherapy when ^{103}Pd-radioisotope is added to the core.[21-23] As previously mentioned, tuning the magnetic properties of NPs via their size, while maintaining superparamagnetism, has limitations, while influencing anisotropy presents a valuable alternative. This paper describes the attempt to enhance the magnetic properties of Pd/Fe-oxide NPs by tuning their magnetocrystalline anisotropy through doping the Fe-oxide coating with Mn. The literature reports the possibility of replacing Fe-cations in the crystal lattice with Mn-cations through the cation-exchange (CE) method,[24] which involves mixing and heating of the pre-made Fe-oxide NPs with additional precursors and surfactants. Therefore, in view of the eventual need for ^{103}Pd-radiolabeling, the MNPs in this study were synthesized using a seed-mediated thermal decomposition with varying amounts of Mn-precursor. The similar sizes and shapes of the obtained Pd/Fe|Mn-oxide NPs allowed to investigate the effect of Mn-doping on magnetic properties, heating and imaging performance.

Materials and methods

Reagents

Palladium (II) acetate, oleylamine (OAm), tert-butylamine-borane complex, ethanol, hexane, iron (III) acetylacetonate ($Fe(acac)_3$), manganese (II) acetylacetonate ($Mn(acac)_2$), 1,2-hexadecanediol, 1-octadecene (ODE), oleic acid (OA), chloroform, 1,2-distearoyl-sn-glycero-3-phosphoethanolamine-N-[carboxy(polyethylene glycol)-2000] sodium salt (DSPE-PEG_{2000}-COOH), ethylenediaminetetraacetic acid disodium salt dihydrate (EDTA), sodium hydroxide (NaOH), manganese(II) chloride tetrahydrate ($MnCl_2 \cdot 4H_2O$), toluene. All chemicals were purchased from Sigma Aldrich and used without further purification.

Preparation of oleylamine capped Pd NPs (seeds)

OAm capped Pd-seeds were prepared based on previously published protocols.[25, 26] Briefly, Pd(II) acetate (56 mg, 0.249 mmol) was added to 15 mL OAm in a 3-neck round-bottom flask. The reaction mixture was heated to 60 °C in 10 min under a stream of nitrogen gas and vigorous stirring. In parallel, *t*-butylamine-borane complex (130 mg, 1.495 mmol) was dissolved in 3 mL OAm and injected into the reaction mixture via a septum, once the temperature reached 60 °C. After addition, the reaction mixture was further heated to 90 °C with a heating rate of 3 °C/min and kept at this temperature for 60 min. After that, the reaction mixture was left to cool down to room temperature and the Pd NPs were collected by addition of 30 mL ethanol and centrifugation for 8 min at 10500 RPM (11830 × g). The Pd seeds were stored as such until further use. The final product was re-dispersible in organic solvents such as toluene, hexane, or chloroform.

Preparation of Pd/Fe|Mn-oxide via a seed-mediated method

The procedure employed to prepare Pd/Fe|Mn-oxide NPs for this study was adopted from protocols presented in previously published articles (Figure 2.1 A).[27, 28] $Fe(acac)_3$ (23.5 mg, 0.066 mmol) together with $Mn(acac)_2$ (8 mg, 0.033 mmol or 4 mg, 0.015 mmol) and 1,2-hexadecanediol (50 mg) were added to a 3-neck round bottom flask containing 20 mL ODE, 660 µL OA, and 65 µL OAm. OAm capped Pd NPs (5.3 mg, 0.05 mmol) were dispersed in approximately 0.4 mL hexane and sonicated for 5 min. Next, the Pd-seeds in hexane were added to the 3-neck round bottom flask. The reaction mixture was slowly heated to 120 °C under N_2 flow and vigorous stirring and left at this temperature for 20 min to ensure the complete removal of hexane. Subsequently, the reaction mixture was further heated to 205 °C with a heating rate of 5 °C/ min and kept at this temperature for 120 min. After that, the reaction mixture was further heated to 315 °C with a heating rate of 5 °C and kept at this temperature for 60 min. Next, the reaction mixture was left to cool down to room temperature and the Mn-doped Pd/Fe-oxide NPs with different Fe:Mn ratio ((Pd/Fe|(0.5Mn)-oxide and Pd/Fe|(0.25Mn)-oxide) were collected by addition of 30 mL ethanol and centrifugation at 10,500 RPM (11830 × g) for 4-6 min. The procedure was repeated several times with ethanol and one or two times with a combination of ethanol and hexane in equal volumes. Lastly, the NPs were dried by a gentle flow of N_2/compressed air and stored as such until further use. The final product could be redispersed in organic solvents such as toluene, hexane, chloroform.

Preparation of Pd/Fe|Mn-oxide via CE-method

Cation exchange of Mn^{2+} with Fe^{2+} was carried out using a previously published protocol (Figure 2.1 B).[29] Pd/Fe-oxide seeds were first prepared using the abovementioned method. 40 mg of these NPs were dispersed in 20 mL mixture of ODE and toluene (1:1 v/v), heated to 100 °C and kept at this temperature for 30 min. After cooling down to room temperature, 9.7 mg (0.4 mmol) $MnCl_2 \cdot 4H_2O$ were added into the flask directly. The mixture was then heated to 180 °C and maintained for 2 h under the N_2 atmosphere. After the solution was cooled naturally, the Mn-doped Pd/Fe-oxide NPs were collected by centrifugation at 10,500 RPM (11830 × g) for 4-6 min and washed three times with a mixture of ethanol and hexane in equal volumes. The NPs were dried by a gentle flow of N_2/compressed air and stored as such until further use. The final product could be redispersed in organic solvents such as toluene, hexane or chloroform.

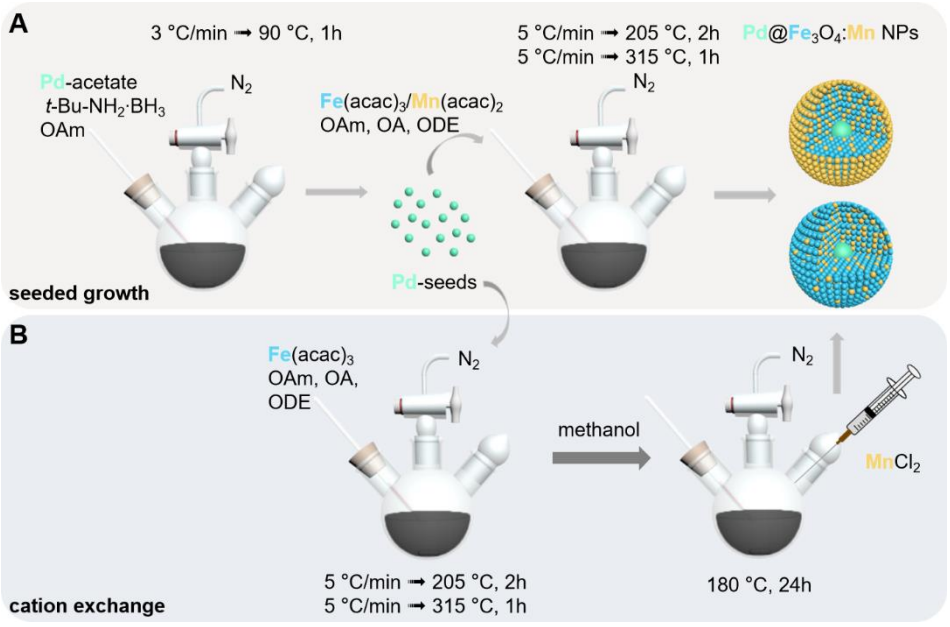

Figure 2.1 Illustration of (**A**) seeded growth and (**B**) cation exchange method for nanoparticle synthesis.

Dispersion of Pd/Fe|Mn-oxide NPs in aqueous media with DSPE-PEG$_{2000}$-COOH

The synthesized Pd/Fe|Mn-oxide NPs were transferred into water by means of functionalization with DSPE-PEG_{2000}-COOH following a slightly modified protocol presented elsewhere.[30] Firstly, 2 mg of Pd/Fe|Mn-oxide NPs were dispersed via ultrasonication in 1 mL of $CHCl_3$ containing 1.5 mg of PEG surfactant. The vial containing the mixture was left open for 24 h for the slow evaporation of the solvent, until a pasty precipitate remained at the bottom of the vial. The residual solid was heated to 80 °C for 10 min in a vacuum oven and subsequently flushed with a gentle N_2

flow to ensure complete removal of $CHCl_3$. Next, 1 mL of Milli-Q water was added to the precipitate and sonicated for 15 min until a colloidal aqueous suspension was obtained. The colloidal suspension of NPs was pipetted into Eppendorf vials and the unbound polymer and excess lipids were removed by two rounds of centrifugation for 1 h at 19,600 RPM (30,000 × g) and subsequent removal of the supernatant. Lastly, the NPs were collected in 1-2 mL of Milli-Q water and kept as such for further use.

Pd- and Mn-leakage study

Pd/Fe|Mn-oxide NPs (2.5 mg) with the surface covered with DSPE-PEG_{2000}-COOH surfactant were resuspended in 0.5 mL of different incubation media (1 mM EDTA (pH 7.4), acidified water (pH 6.5), saline, and serum). The NPs were left in suspension for a specified amount of time (24h for EDTA, and 48h for all other media), after which they were placed in an Amicon Ultra Centrifuge tube with a centrifugal concentrator Ultracel (30 kDa MWCO regenerated cellulose membrane) and centrifuged for 20 min at 4200 RPM. The filtrate was collected and analyzed with ICP-MS to determine the Pd and Mn content. The NPs were then resuspended in a fresh medium and incubated until the next time point, after which the same measurement procedure was applied.

Physical methods

Particle size, size distribution and morphology of the samples were determined by transmission electron microscopy (TEM), using a 120 kV Jeol-JEM1400 microscope. The samples were prepared by drop-casting a diluted NP's suspension in organic solvents such as hexane on a Quantifoil R1.2/1.3 Cu300 grid and evaporating the solvent at room temperature. The mean diameter and the size distribution of the samples were obtained by statistical analysis of around 500-1000 NPs, using TEM images and Image J software. The elemental mapping analysis was done with an Oxford Instruments EDS detector X-MAX^N 100TLE on the same grids used for TEM. Dynamic light scattering (DLS) was measured on a Malvern Pananalytical Zetasizer Pro (Worcestershire, UK) equipped with a 633 nm laser.

Magnetic characterization by superconducting quantum interference device (SQUID), was carried out on an MPMS XL magnetometer from Quantum Design, using about 1-2 mg of dry NPs. The hysteresis loops M(H) obtained under continuously varying applied magnetic field up to a maximum of ±60 kOe at 5 and 300 K were used for evaluation of saturation magnetization and coercivity. Transmission ^{57}Fe Mössbauer spectra were collected at 4.2 K with a conventional constant-acceleration spectrometer using a ^{57}Co(Rh) source. Velocity calibration was carried out using an α-Fe foil. The Mössbauer spectra were fitted using the Mosswinn 4.0 program. The heating power measurements were performed using the Magnetherm Digital device manufactured by Nanotherics, with either 50 mm or 60 mm coil, at alternating magnetic fields of 346 or 338 kHz and field strengths of 23 or 18 mT, respectively, used for the calculation of the SLP values. The device was equipped with two glass-fiber optic thermometers (Osensa PRB-G40_2.0-STM-

MRI) to measure the temperature at the core (used for SLP) and bottom (to check for a possible precipitation) of the sample. A sample of 1 mg/mL of NPs was inserted in an insulated sample holder to reduce heat loss to the environment and placed in the middle of the coil. The temperature was equilibrated until it varied less than 0.05 °C/min before the start of the measurement. The sample was then exposed to the magnetic field. The heating capacity of MNPs is described as specific loss power (SLP) or intrinsic loss power (ILP) expressed in W/g_{Fe+Mn} or nHm^2/kg, respectively.

Measurement of the longitudinal (T_1) and transverse (T_2) relaxation times were performed on a 1.5T at a 450W MR scanner (GE Healthcare, Waukesha, WI, USA) using phantoms prepared in Eppendorf vials by suspending 1 mg of NPs in an agar solution. T_1 relaxation times were measured with an inversion recovery turbo spin echo sequence with the following parameters: repetition time (TR) = 3000 ms, inversion time (TI) = 50, 100, 200, 250, 500, 750, 1000, and 1500 ms, echo time (TE) = 11.2 ms, field of view (FOV) = 192 × 192 mm^2, slice thickness = 4 mm, acquisition matrix = 192 × 192, and number of excitations (NEX) = 1. The data was analyzed with MATLAB script (R2018b, The MathWorks INC, Natick, USA) developed by Barral et al.[31] The T_2 relaxation times were measured with a spin echo sequence with the following parameters: TR = 200 ms, TE = 9, 15, 25, 35, 55, and 75 ms, FOV = 192 × 192 mm^2, slice thickness = 4 mm, acquisition matrix = 128 × 128, and number of excitations (NEX) = 1. The data was fitted with a mono-exponential signal decay model using the MATLAB nonlinear curve fitting function. Relaxation measurements were repeated once, and the obtained values were calculated per voxel and reported as the mean with standard deviation over approximately 120 voxels per sample.

The SLP values and the relaxivities ($1/T_i$, i=1,2) of the samples were calculated using the concentrations of Fe and Mn obtained from the Inductively Coupled Plasma Optical Emission spectroscopy (ICP-OES) data performed on the same samples after a microwave aided destruction of NPs dispersed in a 5% solution of HNO_3. The Electron Paramagnetic Resonance (EPR) spectra were obtained with Bruker EMXplus X-band EPR spectrometer using standard resonator (ST9107) at room temperature operating at microwave frequency of 9.78 GHz, microwave power of 0.002-63 mW (powerplot) or 20 mW, modulation frequency of 100 kHz, and modulation amplitude of 2.5 (powerplot) or 5 Gauss. NPs resuspended in hexane were added to an EPR tube and hexane was evaporated using N_2 flow. The EPR tube was placed in the cavity so that only part of the sample was in the measurement window.

Results and Discussion

Synthesis and characterization of Pd/Fe|Mn-oxide NPs

In our previous work, $Fe(CO)_5$ was used as iron precursor for the synthesis of Pd/Fe-oxide NPs to obtain a uniform core-shell structure.[21, 22] However, in this work, $Fe(acac)_3$ was considered a better option, as it can be easily adapted to the preparation of $MnFe_2O_4$ by simply adding $Mn(acac)_2$ to the reaction mixture along with the $Fe(acac)_3$ precursor.[11] Both $Fe(acac)_3$ and $Mn(acac)_2$ precursors are readily available, as acetylacetonate group coordinates to a range of metals, including Fe and Mn, with decomposition temperatures around 200 °C.[11, 28, 32] The synthesis method used to generate Pd/Fe|Mn-oxide NPs was a seed-mediated thermal decomposition, similar to that employed for Pd/Fe-oxide NPs, where pre-made OAm-capped Pd NPs were introduced into the reaction mixture to act as seeds on which the Fe|Mn-oxide simultaneously nucleates and grows as a coating. However, the newly introduced precursors failed to form core-shell structures, presumably because of the differences in nucleation/growth regimes of $Fe(acac)_3$ and $Mn(acac)_2$ as a consequence of their different chemical properties and reactivities. While $Fe(CO)_5$ favors heterogeneous nucleation on the seed's surface followed by successive growth rather than homogeneous nucleation, $Fe(acac)_3$ does not exhibit the same preference, with homogeneous nucleation being favored in this case. During the synthesis, this resulted in a mixture of single Fe|Mn-oxide NPs, uncoated Pd-seeds and incomplete core-shell morphology, as reported elsewhere.[27]

Therefore, new measures were employed during the synthesis with $Fe(acac)_3$ and $Mn(acac)_2$ precursors to promote heterogeneous nucleation and the formation of Pd/Fe|Mn-oxide NPs. These measures included: i) using smaller amounts of Fe-Mn precursors to avoid supersaturation conditions that promote homogeneous nucleation, ii) adding less OAm-surfactant during the reaction, iii) incorporating an intermediate temperature step at approximatively 200 °C for an extended period of time to stimulate the formation of Fe(III)-complex with surfactants, iv) using a long-chain diol (1,2-hexadecanediol) as an accelerant in the formation of Fe-O-Fe bonds and as a mild reducing agent, and v) increasing the temperature of 315 °C for the growth stage. Similar measures to promote the heterogeneous nucleation of $Fe(acac)_3$ on pre-made seeds have been proposed in other studies.[27]

After tuning the synthetic protocol accordingly, Pd/Fe|Mn-oxide NPs were successfully prepared via thermal decomposition of Fe and Mn acetylacetonate precursors forming a heterogeneous coating on preformed OAm-capped 5 mm Pd-seeds (Figure 2.1 A), leading to hybrid MNPs with spherical-squared morphology and sizes around 22 nm, as can be seen in the TEM images presented in Figure 2.2 B, C. Two experiments were conducted, in which different amounts of $Mn(acac)_2$ relative to $Fe(acac)_3$ were employed during the synthesis: 1[Mn]:2[Fe] and 1[Mn]:4[Fe]. The two batches of NPs will be referred as Pd/Fe|(0.5Mn)-oxide and Pd/Fe|(0.25Mn)-oxide, respectively. Independent of the precursor ratio introduced in the reaction,

the hybrid MNPs obtained the same spherical-squared morphology (Figure 2.2 B, C). In the bright-field TEM images, the darker areas correspond to Pd, whereas lighter contrast represents Fe|Mn-oxide, as result of the different electron density of Pd compared to Fe and Mn, which both exhibit a similar density and cannot be differentiated via different contrast in TEM images, making it impossible to confirm the presence of the two metals in the targeted composition of the hybrid MNPs. For this, EDS elemental mapping analysis was performed on the two batches of synthesized Pd/Fe|Mn-oxide NPs visualizing the individual signals for Pd, Fe, and Mn to confirm their localization within the NP (Figure 2.2 D, E).

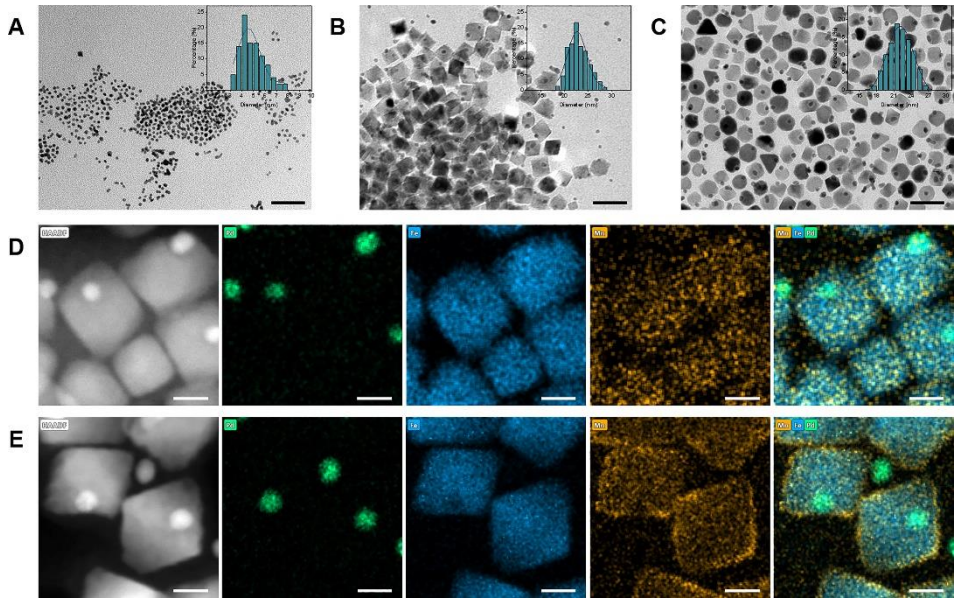

Figure 2.2 TEM images and size distribution of (**A**) Pd, (**B**) Pd/Fe|(0.25Mn)-oxide, (**C**) Pd/Fe|(0.5Mn)-oxide (scal bar: 50 nm) and EDS mapping of (**D**) Pd/Fe|(0.25Mn)-oxide and (**E**) Pd/Fe|(0.5Mn)-oxide NPs (scale bar: 10 nm).

Interestingly, in NPs prepared with higher amount of Mn (Pd/Fe|(0.5Mn)-oxide), the Mn was found to be dispersed within the Fe-oxide coating with most of the Mn atoms located at the surface, forming an outer rim (Figure 2.2 E). This effect was not observed in the particles prepared with lower Mn amount (Pd/Fe|(0.25Mn)-oxide), most probably due to an insufficient amount of Mn atoms (Figure 2.2 D). The EDS mapping analysis confirmed the successful synthesis of Pd/Fe|Mn-oxide hybrid MNPs, with spherical-square morphologies, relevant sizes (±) and different amount of Mn-doping, which increased with the higher [Mn]:[Fe] precursor ratio introduced in the synthesis.

To get insight into the effects of Mn-doping on the Fe-oxide framework, which is crucial for interpreting the magnetic properties of the NPs, Mössbauer spectroscopy was performed at 4.2 K, revealing the hyperfine parameters of Fe ions in both Pd/Fe|Mn-oxide NPs (Table 2.1). The advantage of performing the measurements at this temperature is that magnetite undergoes Verwey transition,[33] where signals of all three components (tetrahedral Fe^{3+}, octahedral Fe^{3+} and octahedral Fe^{2+}) can be observed separately, with a typical ratio of 1:1:1. Indeed, this ratio was observed for Pd/Fe|(0.25Mn)-oxide NPs, where 28% of their components could be fitted with the contributions from magnetite species. A paramagnetic doublet (16%) observable in the spectrum (Figure 2.3 A) can be explained as the result of the interaction of Fe with paramagnetic Mn dispersed in the lattice without taking part in the crystal structure.

Table 2.1 The Mössbauer fitted parameters of the Pd/Fe|Mn-oxide samples at 4.2 K.

Sample	IS (mm s^{-1})	QS (mm s^{-1})	Hyperfine field (T)	Γ (mm s^{-1})	Phase [a]	Spectral contribution (%)
Pd/Fe|(0.25Mn)-oxide	0.30	-0.05	51.0	0.41	Fe^{3+} (Fe_3O_4,A) yellow	9
	0.40	0.08	52.3	0.41	Fe^{3+} (Fe_3O_4,B) cyan	9
	0.85	-0.32	46.0	0.74	Fe^{2+} (Fe_3O_4,B) magenta	10
	0.57	1.03	-	0.42	Fe^{3+} green	16
	0.48	-0.02	51.3	0.46	Fe^{3+} (Fe_3O_4,A)* blue	29
	0.50	-0.01	53.4	0.41	Fe^{3+} (Fe_3O_4,B)* red	27
Pd/Fe|(0.5 Mn)-oxide	0.42	-0.03	50.7	0.77	Fe^{3+} (Fe_3O_4,A)* blue	50
	0.47	0.01	53.1	0.59	Fe^{3+} (Fe_3O_4,B)* red	50

Experimental uncertainties: Isomer shift: IS ± 0.02 mm s^{-1}; Quadrupole splitting: QS ± 0.02 mm s^{-1}; Line width: Γ ± 0.03 mm s^{-1}; Hyperfine field: ± 0.1T; Spectral contribution: ± 3%; [a] Tetrahedral (A) and octahedral (B) sites of magnetite, the color code is used in Figure 2.3; *influenced by Mn^{2+} dopants.

Interestingly, another 27% and 29% of the contributions were also fitted with the functions for the tetrahedral and octahedral Fe^{3+} of magnetite, with slight differences in IS and magnetic field due to the influence of Mn and Pd dopants. However, about 28% of octahedral Fe^{2+}, typically present in a magnetite spectrum, was absent, likely due to the replacement by Mn^{2+}. Since Mössbauer spectroscopy focuses solely on the state of Fe, the effect of Mn interaction was observed indirectly through the exclusive presence of tetrahedral and octahedral Fe^{3+}. As Mn^{2+} doping increases, Fe^{2+} ions are progressively replaced, leading to a gradual disappearance of octahedral Fe^{2+} from the spectrum (Figure 2.3 B). A similar pattern was observed in the spectrum of Pd/Fe|(0.5Mn)-oxide NPs, where both tetrahedral and octahedral Fe^{3+} contributed equally (50%), indicating complete replacement of Fe^{2+}. Consequently, the excess of Mn^{2+} accumulated at the surface, forming an outer rim.

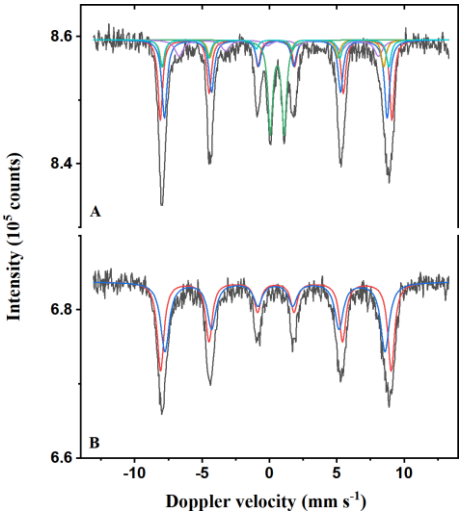

Figure 2.3 Mössbauer spectra obtained at 4.2 K with the Pd/Fe|(0.25Mn)-oxide (**A**) and Pd/Fe|(0.5Mn)-oxide NPs (**B**). The color codes are indicated in Table 2.1.

X-ray diffraction (XRD) performed on both Pd/Fe|(0.25Mn)-oxide and Pd/Fe|(0.5Mn)-oxide NPs confirmed further the appearance of Mn in the lattice by demonstrating cubic phase ferrite, corresponding to the standard card of $Fe_{2.8}Mn_{0.2}O_4$ (JCPDS: 04-024-5003) and Fe_2MnO_4 (JCPDS: 01-071-4919), respectively (Figure 2.4). The average grain size of both nanoparticles was calculated using Scherrer Equation.[34] The grain size of Pd/Fe|(0.5Mn)-oxide NPs (19.34 nm) is comparable to the overall nanoparticle size, while the grain size of Pd/Fe|(0.25 Mn)-oxide NPs is slightly smaller (14.68 nm). Following DSPE-PEG_{2000}-COOH coating, necessary to transfer the NPs into aqueous media, the morphology remained unchanged (Figure 2.5 A). The hydrodynamic size was measured to be 159.4 nm, which is of a similar magnitude compared to that of the undoped Pd/Fe-oxide (113.8 nm) (Figure 2.5 B), and the colloidal stability of the NPs remained good across various buffer solutions and pH lower than physiological (Figure 2.5 C, Table 2.2).

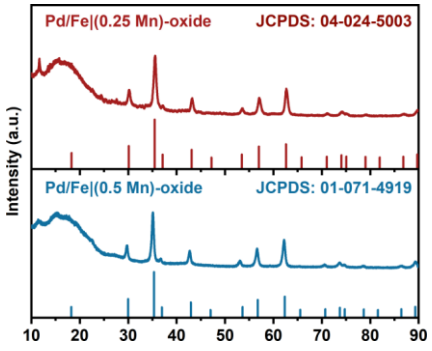

Figure 2.4 XRD patterns of Pd/Fe|Mn-oxide NPs.

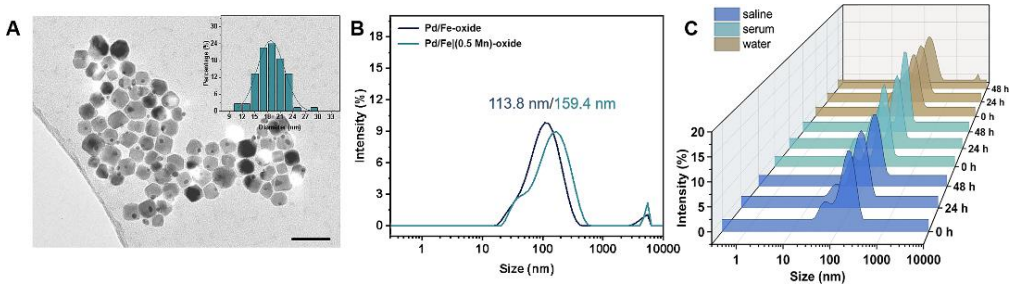

Figure 2.5 (**A**) TEM images of Pd/Fe|Mn-oxide NPs after DSPE-PEG2000-COOH coating, (**B**) hydrodynamic sizes of Mn-doped and undoped Fe-oxide NPs, and (**C**) DLS spectra of Pd/Fe|Mn-oxide NPs dispersed in saline, serum and acidified water after 0, 24 and 48h.

Table 2.2 Hydrodynamic sizes of Pd/Fe|Mn-oxide NPs dispersed in saline, serum and acidified water after 0, 24 and 48 hours measured by DLS.

Time (h)	Saline		Serum		Water (pH 6.5)	
	Size (nm)	POD	Size (nm)	POD	Size (nm)	POD
0	189.2	0.3316	192.7	0.3566	183	0.3678
24	179.5	0.3188	202.6	0.3719	169.4	0.2987
48	295	167.4	0.3309	197.3	0.3589	188.2

Magnetic properties of Pd/Fe|Mn-oxide MNPs

The static magnetic behavior of the Pd/Fe|Mn-oxide MNPs was investigated by SQUID magnetometry directly after the synthesis, which means that the MNPs were coated with OA after the thermal decomposition and the subsequent cleaning procedure. The magnetization curves resulting from the alignment of the MNPs in the presence of an increasing magnetic field (up to 50 kOe) were measured at 5 K and 300 K, as shown in Figure 2.6 A and 2.6 B, respectively.

The saturation magnetization was determined by extrapolating the highest magnetization values (40 kOe) to the ordinate axis, where the field approaches zero (Table 2.3). The M_S values obtained for the two batches of Pd/Fe|Mn-oxide MNPs were corrected for the presence of Pd-core and organic layer at the surface, hence expressed as emu/g_{Fe+Mn}. For both temperatures, 5 and 300 K the saturation magnetization values were higher for the Pd/Fe|(0.5Mn)-oxide, which are NPs with higher Mn content (Figure 2.6, Table 2.3). It is important to note that the hysteresis loops present small dips at high fields because of the strong diamagnetic interaction of the plastic capsule used during the measurements.

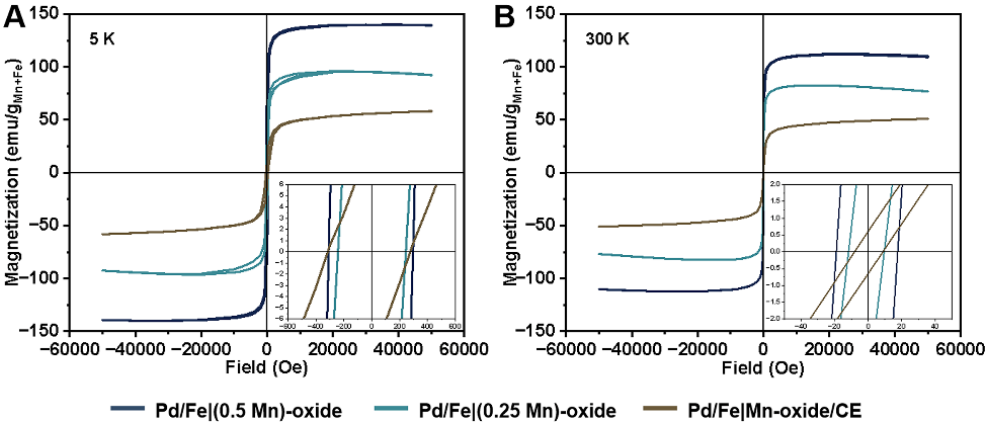

Figure 2.6. SQUID magnetometry of Pd/Fe|Mn-oxide MNPs: **(A)** $M(H)_T$ curves at T = 5 K; **(B)** $M(H)_T$ curves at T = 300 K; the insets represent 120´ (**A**) and 1200´ (**B**) magnification of the x-axis showing coercivities.

As both batches of MNPs possess similar sizes, the differences in M_S values can be attributed to the content of doping material in their composition. According to multiple literature data, doping Fe-oxide crystal structures with paramagnetic cations, such as Mn or Co, results in an increase in magnetic anisotropy due to the replacement of Fe^{2+}/Fe^{3+} cations with more anisotropic Mn^{2+} or Co^{2+}. Additionally, the same studies observed that an increased magnetic anisotropy ensured higher M_S values, which translates in more effective magnetic properties. As the M_S values obtained for Pd/Fe-oxide NPs described previously were not corrected for Pd-core and surfactants,[21] a relevant comparison could not be made in this case. Nevertheless, it is clear that adjusting the composition of the MNPs is indeed a better strategy to increase the M_S of the NPs than size manipulations.

Table 2.3 Overview of the magnetic properties of Pd/Fe|Mn-oxide and Pd/Fe-oxide NPs: saturation magnetization (M_S) at 40 kOe, T = 5 K and 300 K, coercivity (H_C) at T = 5 K and 300 K, and calculated SLP, r_1 and r_2 values.

MNPs	M_S (emu/g_{Fe+Mn})		H_C (O_e)		SLP[a] (W/g_{Fe+Mn})	r_1[b] (mM_{Fe+Mn}^{-1} s^{-1})	r_2[b] (mM_{Fe+Mn}^{-1} s^{-1})
	5K	300K	5K	300K			
Pd/Fe|(0.5 Mn)-oxide	140	112	308	20	386	8.74 ± 0.3	443
Pd/Fe|(0.25 Mn)-oxide	95	83	240	12	352	5.95± 0.4	404
Pd/Fe-oxide[c]	69	61	67	12	233	-[d]	440

[a] Measured at 346 kHz, 23 mT with STD ≤ 5-10%; [b] measured at 1.5 T and 25 °C; [c] from previous work;[21] [d] not measured.

Both magnetization curves at 5 K display hysteresis with substantial coercivity (Table 2.3), which indicates a typical behavior of superparamagnetic MNPs below their blocking temperature. On the other hand, the MNPs exhibit characteristics of the superparamagnetic state at 300 K, with some low remained coercivity that can be attributed to complex interactions, such as frustrated order or spin canting phenomena. Interestingly, the coercivity values at both 5 K and 300 K are also higher for the Pd/Fe|(0.5Mn)-oxide MNPs, which is in line with the increased anisotropy, generally higher for higher Mn-content.[13, 24, 27]

Pd/Fe|Mn-oxide MNPs as hyperthermia/thermal ablation agents

Thermal therapies in oncology include hyperthermia, which involves increasing *in vivo* temperatures to 41-46 °C to sensitize other treatments such as chemo- and radiotherapy, or thermal ablation where the temperatures are >60 °C or at least exceed at least 46 °C to induce targeted ablation and cell death, potentially replacing surgery.[35] Two main mechanisms contribute to dissipation of heat produced by MNPs when exposed to an alternating magnetic field (AMF), depending on their sizes. In larger MNPs, which enter a multi-domain regime, heating results from hysteresis losses. In smaller MNPs, like Pd/Fe|Mn-oxide NPs in this study, which exhibit superparamagnetism, the heat production is attributed to Néel and Brownian relaxation mechanisms.[1, 5, 32]

It is known that magnetic anisotropy plays a critical role in SLP enhancement,[11] thus the heating efficacy of the two Pd/Fe|Mn-oxide batches with different amounts of Mn-doping was evaluated (Figure 2.7). The samples containing 1 mg of Pd/Fe|Mn-oxide MNPs dispersed in 1 mL of water were subjected to an alternating magnetic field at the frequency of 346 kHz and a field strength of 23 mT. The SLP values were determined for both Pd/Fe|Mn-oxide NPs based on the Eq. 1:

$$SLP = \frac{C}{m_{Fe+Mn}} \frac{\Delta T}{\Delta t} \quad (1)$$

where C is the heat capacity of the sample, m_{Fe+Mn} is the sum of the masses (g) of Fe and Mn in the colloidal NPs suspension, determined by ICP-OES, and $\Delta T/\Delta t$ is the temperature increase measured over time. Compared to the previously reported SLP value for Pd/Fe-oxide NPs of 233 W/g_{Fe},[21] the SLPs of Pd/Fe|(0.25Mn)-oxide and Pd/Fe|(0.5Mn)-oxide NPs were determined to be 352 and 386 W/g_{Fe+Mn}, respectively.

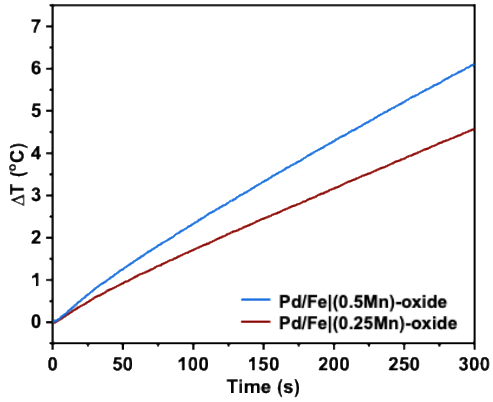

Figure 2.7 Comparison of the temperature change within aqueous suspensions of Pd/Fe|(0.5Mn)-oxide and Pd/Fe|(0.25Mn)-oxide NPs measured over 5 min.

The SLP is directly influenced by extrinsic parameters such as the frequency and amplitude of the applied magnetic field, as well as the viscosity of the surrounding medium.[12] It is also affected by intrinsic parameters, including size of the MNPs, their magnetocrystalline or shape anisotropy, and surface functionalization, which alters local magnetization at the surface of the MNPs. Since all these parameters were consistent across the three investigated MNPs, the superior heating efficiency (increase by 51-66 %) of Pd/Fe|Mn-oxide NPs over the Pd/Fe-oxide NPs can be attributed to the presence and amount of Mn in the Fe-oxide coating. This observation aligns with literature reporting that such doping increases crystalline anisotropy leading to enhanced SLP.[1, 11, 12]

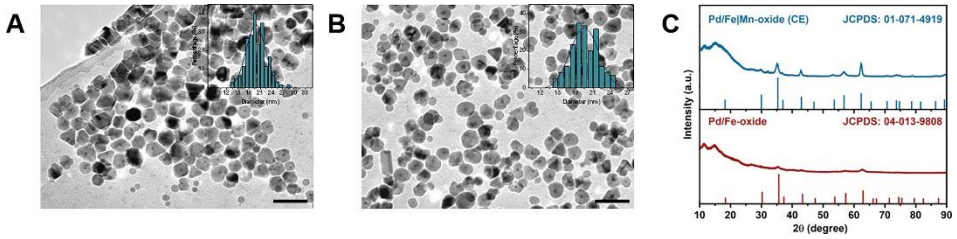

Figure 2.8 TEM images and size distribution of(**A**) Pd/Fe-oxide, (**B**) Pd/Fe|Mn-oxide(CE) (scale bar: 50 nm), and (C) XRD patterns of Pd/Fe-oxide (red) and Pd/Fe|Mn-oxide(CE) (blue) NPs.

To further investigate the effects of Mn-doping, a batch of pre-made Pd/Fe-oxide NPs was doped with Mn via a cation exchange procedure[24] yielding Pd/Fe|Mn-oxide(CE) NPs with spherical-squared morphology and size of 19 nm (Figures 2.8 A and B). The XRD patterns (Figure 2.8 C) confirmed the successful incorporation of Mn into the lattice, showing highly crystalline cubic phase, corresponding to the standard card of Fe_2MnO_4 (JCPDS: 01-071-4919). The heating efficacy of Pd/Fe|Mn-oxide(CE) NPs was compared with that of Pd/Fe|(0.5 Mn)-oxide NPs by calculating their intrinsic loss power (ILP) values (Eq. 2), which are independent of experimental conditions (i.e. frequency (*f*) and magnetic field (*H*)).

$$ILP = \frac{SLP}{f \cdot H^2} \qquad (2)$$

The ILP values of CE NPs have previously been shown to be higher than those of Fe NPs due to Mn^{2+} exchange.[29] However, the ILP value of Pd/Fe|Mn-oxide(CE) NPs (1.289 nHm^2/kg) was lower than that of the developed Pd/Fe|(0.5Mn)-oxide NPs (3.083 nHm^2/kg) (Figure 2.9). This can be attributed to a lower fraction of Fe^{2+} (4%) that has been replaced with Mn^{2+} in the CE-procedure, as revealed by Mössbauer spectroscopy (Figure 2.10 and Table 2.3). These results indicate that the seeded growth method is a better choice for Mn^{2+} doping, not only for achieving higher heating efficiency, but also because it eliminates the need for an additional synthetic step.

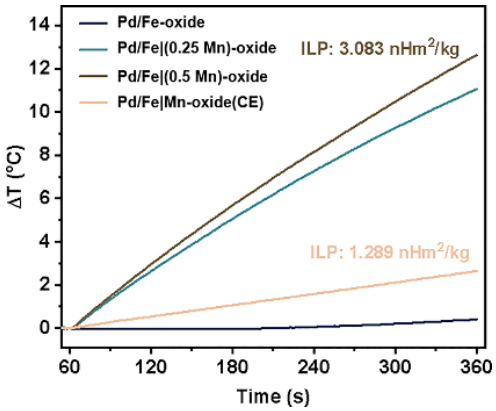

Figure 2.9 Comparison of the temperature change within aqueous suspensions of Pd/Fe|(0.5Mn)-oxide and Pd/Fe|Mn-oxide(CE) NPs measured over 6 min.

Table 2.3 The Mössbauer fitted parameters of the Pd/Fe|Mn-oxide/CE samples at 4.2 K.

IS (mm s^{-1})	QS (mm s^{-1})	Hyperfine field (T)	Γ (mm s^{-1})	Phase [a]	Spectral contribution (%)
0.40	0.01	50.7	0.41	Fe^{3+}(Fe_3O_4,A) dark-yellow	31
0.50	-0.02	52.8	0.54	Fe^{3+} (Fe_3O_4, B1) cyan	30
0.80	-0.63	47.8	0.72	Fe^{2+} (Fe_3O_4, B2) magenta	19
0.94	0.74	46.9	0.72	Fe^{2+} (Fe_3O_4, B3) green	6
1.47	1.50	38.7	0.72	Fe^{2+} (Fe_3O_4, B4) brown	6
0.40	0.01	50.5	0.41	Fe^{3+} (Fe_3O_4, A)* blue	4
0.51	0.00	52.7	0.52	Fe^{3+} (Fe_3O_4, B)* red	4

Experimental uncertainties: Isomer shift: IS ± 0.02 mm s^{-1}; Quadrupole splitting: QS ± 0.02 mm s^{-1}; Line width: Γ ± 0.03 mm s^{-1}; Hyperfine field: ± 0.1T; Spectral contribution: ± 3%; [a] Tetrahedral (A) and octahedral (B) sites of magnetite; *influenced by Mn^{2+} dopants.

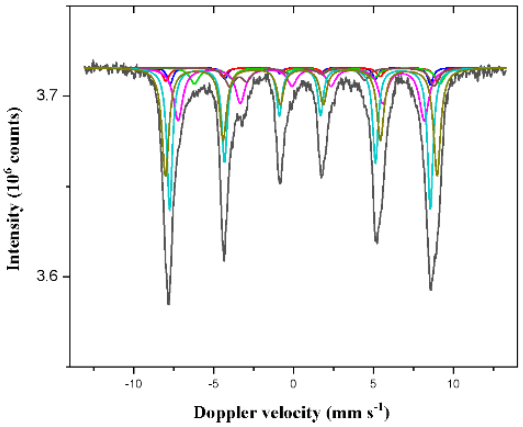

Figure 2.10 Mössbauer spectrum obtained at 4.2 K with Pd/Fe|Mn-oxide/CE NPs.

Pd/Fe|Mn-oxide MNPs as MR imaging agents

MRI is a well-known, non-invasive high-resolution imaging technique in medicine that generates anatomical images based on the differences in relaxation of water protons around solid tissue and the surrounding biological media in the presence of a magnetic field. The proton relaxation rates can be altered by administration of contrast agents (CAs), enhancing MRI sensitivity and contrast of the images. MRI CAs function by reducing either the longitudinal (T_1) or the transversal (T_2) relaxation times of protons in the target tissue, generating T_1-weighted images that give positive (bright) image contrast and T_2-weighted images that result in negative (dark) contrast, respectively.[8, 11, 36] T_1 CAs are typically based on paramagnetic ions like Gd^{3+} and Mn^{2+}, often in the form of ion-complexes, whereas T_2 CAs generally rely on superparamagnetic NPs. However, since MNPs designed for MH/TA are intended for intratumoral injection, they are expected to reach much higher local concentrations compared to intravenous administration. At these concentrations, the elevated r_2-values could introduce artifacts in T_2-weighted imaging, limiting its effectiveness until the MNPs diffuse and their local concentration diminishes. By doping Pd/Fe-oxide with paramagnetic Mn, the resulting MNPs may exhibit both T_1 and T_2 contrast effects. To assess this potential dual-contrast capability, T_1 and T_2 measurements were performed on both batches of Pd/Fe|Mn-oxide NPs after transferring them to an aqueous medium with DSPE-PEG_{2000}-COOH. Results in Table 2.4 demonstrate that the r_2-relaxivities of both Pd/Fe|(0.25Mn)-oxide and Pd/Fe|(0.5Mn)-oxide are comparable to that of Pd/Fe-oxide NPs alone. Interestingly, the r_1 value for Pd/Fe|(0.5 Mn)-oxide (8.74 mM_{Fe+Mn} s^{-1}) is higher than for Pd/Fe|(0.25 Mn)-oxide (5.95 m_{MFe+Mn} s^{-1}), as expected due to higher Mn-content. Additionally, according to Li et al., T_1-effects are driven by Mn^{2+}-ions at the MNPs surface,[37] which is consistent with our Pd/Fe|(0.5Mn)-oxide NP's as confirmed by EDS analysis. Figure 2.11 A shows an indication of T_1 contrast enhancement generated by both Pd/Fe|Mn-oxide NPs, with a more substantial effect for Pd/Fe|(0.5 Mn)-oxide. Clearly, the T_1-contrast enhancement produced by the latter MNPs is insufficient and is unlikely to enable them to function as dual T_1/T_2 CAs in practical applications, which would require the r_1/r_2 ratio close to 1.[38] However, understanding how surface Mn-doping affects relaxivity, might potentially guide further modifications to optimize contrast characteristics and tune NPs design for other multimodal imaging context, where even slight T_1 contributions might enhance overall imaging performance.

Table 2.4 The EPR parameters of Pd/Fe|(0.5Mn)-oxide and Pd/Fe|(0.25Mn)-oxide NPs.

MNPs	H_r[a] (mT)	DH_{pp}[b](mT)	P_{asy}[c]	g_{peak}[d]	$g_{crossover}$[f]	g_{valley}[g]
Pd/Fe|(0.25 Mn)-oxide	250	147	2.03	3.35	2.44	1.96
Pd/Fe|(0.5 Mn)-oxide	326	155	0.82	2.78	2.07	1.72
Pd/Fe-oxide	295	163	1.86	3.14	2.38	1.81

[a] Resonance field; [b] line width; [c] the ratio of the amplitude of the peak above and below the baseline; [d] g-factor at the positive peak the EPR signal; [f] g-factor at H_r; [g] g-factor at the negative peak the EPR signal. $g = \frac{h \cdot \nu}{\mu_B \cdot B}$ with h = Planck constant, ν = microwave frequency (9.78 Hz), μB = Bohr magneton, B = magnetic field (T). The g-factor for a free electron in vacuum $g_e = 2.00232$.

To gain more insight into the interplay of the magnetic components constituting the MNPs (i.e. Fe and Mn), EPR spectra of dry Pd/Fe|Mn-oxide NPs with different Mn-content were recorded at room temperature and the obtained parameters are summarized in Table 2.4. As shown in Figure 2.11 B, the EPR active spins of both samples resulted in broad spectra ranging from 1500 to 4500 Gauss. The power saturation behavior of the EPR signals in both cases shows almost no saturation, confirming the fast relaxation of the spins (Figure 2.11 C). The slight decrease in signal intensity at maximal power (200 mW), being more pronounced for Pd/Fe|(0.25Mn)-oxide NPs, indicates slower relaxation for the less Mn-containing MNPs. This is consistent with the larger ΔH_{pp} due to shorter spin lifetime for more Mn-containing NPs, Pd/Fe|(0.5Mn)-oxide. The EPR spectra of the Pd/Fe-oxide NPs with and without Mn-doping obtained at powers corresponding to each data point in the power saturation curves, are shown in Figure 2.11 D-F.

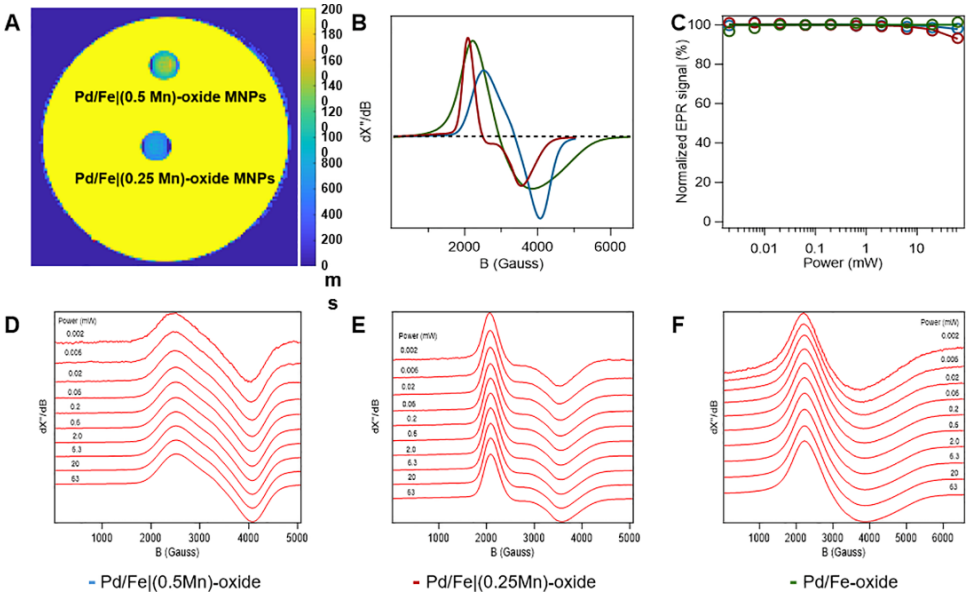

Figure 2.11 T_1-mapping measured at 1.5 T and 25 °C on agar phantoms containing Pd/Fe|(0.25Mn)-oxide (top) and Pd/Fe|(0.5Mn)-oxide (bottom) NPs (**A**); EPR spectra of the powder samples, with the signal intensity of the two spectra normalized to their maximal signal amplitude **(B)**; Power saturation curves **(C)**. EPR conditions: microwave frequency, 9.78 GHz; microwave power, 20 mW (A) and 0.002-63 mW (B), modulation frequency, 100 kHz, modulation amplitude, 5 Gauss (A) and 2.5 Gauss (B); room temperature. And (**D-F**) EPR spectra of Pd/Fe-oxide NPs with and without Mn-doping corresponding to each data point in power saturation curve.

The line shape of Pd/Fe|(0.25 Mn)-oxide NPs corresponds to a so-called Dysonian line, which is determined by the diffusion of electrons, the penetration depth of the microwaves and relaxation time, while the more symmetrical line shape of Pd/Fe|(0.25 Mn)-oxide NPs resembles those observed for superparamagnetic Fe-oxide NPs in general,[38] as well as the control Pd/Fe-oxide NPs

in this study (Figure 2.11 B). According to Dyson theory, the symmetry parameter P_{asy} is correlated with the ratio of electron diffusion and spin lifetime T_D/T_{spin}. Since the spin lifetime T_{spin} (inversely proportional to the ΔH_{pp}) contains both T_1 and T_2 relaxation in metals, the calculated P_{asy} value for Pd/Fe|(0.5Mn)-oxide is significantly lower compared to the less Mn-containing NPs.

Pd- and Mn-leakage studies

Since the designed Pd/Fe|Mn-oxide NPs are intended for biomedical applications, their biocompatibility is of great importance. Palladium is considered toxic for the human body, with the hypothesized mechanism being the release of Pd ions, which can elicit a range of cytotoxic effects *in vivo*.[39] Manganese toxicity (*manganism*) is rare but poses a serious health hazard, potentially leading to severe central nervous system pathologies.[40, 41] The Mn cytotoxicity arises from the triggering of apoptosis in cells accumulating toxic doses of Mn. Depending on comorbid disease state or dietary variations, bodily efflux and pancreatic elimination may become dysfunctional, potentially affecting the cellular efflux of Mn as well. Changes in glutamate and glutamine metabolism, mitochondrial function, and the triggering of cellular apoptosis and necrosis are key cellular responses to manganism, eventually leading to the neuropsychiatric manifestations of Mn toxicity.[40] Therefore, with biomedical applications in mind, a study was conducted to determine the amount of Pd and Mn released from the MNPs. To assess this, Pd/Fe|Mn-oxide NPs functionalized with DSPE-PEG_{2000}-COOH were exposed to 1mM EDTA (a compound typically used in leakage studies as it strongly binds di- and trivalent metal ions),[42] and incubated for 24h, 48h and 7d. Since only negligible amounts of Mn and Pd (µg), close to the detection limit and below toxic levels[39,40] were found by ICP-OES (Table 2.5), it could be assumed that Fe-oxide coating encapsulating the Pd-core and the surfactant layers create a sufficient barrier to prevent any Pd or Mn leakage. Similar results were obtained from MNPs incubated with acidified water (pH 6.5), saline and serum after 48 h (Table 2.5). Therefore, the Pd/Fe|Mn-oxide NPs can be considered stable for biomedical use.

Table 2.5 Pd and Mn leakage from Pd/Fe|Mn-oxide NPs in different buffers and pH conditions.

Media	Pd		Mn	
	µg	%	µg	%
EDTA (24h)a	0.019	0.00081	0.196	0.0081
EDTA (48h) a	0.017	0.00071	0.113	0.0047
EDTA (7d) a	0.016	0.00066	0.096	0.0039
water (pH 6.5)b	0.021	0.00105	0.200	0.00999
salineb	0.009	0.00044	0.112	0.00559
serumb	0.017	0.00086	0.199	0.00993

[a] pH 7.4; [b] measured at 48h.

Conclusion

In conclusion, this study demonstrates the significant impact of Mn-doping on the magnetocrystalline anisotropy of Pd/Fe-oxide NPs, positioning them as promising candidates for theranostic applications. Using a seed-mediated thermal decomposition method, Pd/Fe|Mn-oxide NPs with varied Mn-doping levels were synthesized, while preserving the morphology of their undoped counterparts and thoroughly investigated. The successful incorporation of Mn was confirmed through EDS analysis, while SQUID magnetometry revealed that the Mn-doped NPs are superparamagnetic, displaying high saturation magnetization and low coercivity values. These enhancements translated into superior performance in hyperthermia/thermal ablation therapy, where Mn-doped NPs, especially those with higher Mn-content, exhibited up to 1.7 times greater SLP values under AMF exposure compared to their undoped analogues.

Notably, NPs with higher Mn-content showed significant Mn accumulation on their surface, prompting an investigation of their T_1 MRI contrast properties, alongside their evident T_2 enhancement and demonstrated therapeutic potential. Relaxivity measurements and MRI phantom assessments of the Mn-doped NPs provided with a hydrophilic DSPE-PEG_{2000}-COOH layer revealed elevated r_1-values in the samples with the highest Mn-content, reflecting the surface accumulation of Mn. Although the increase in r_1 is insufficient to qualify these NPs as dual T_1/T_2 MRI CAs, these findings emphasize the role of structural modifications in improving both imaging and therapeutic performance of nanomaterials.

Overall, this work provides valuable insights into the design of multifunctional MNPs as cancer theranostics, offering a promising direction for developing more effective probes for thermal therapy, coupled with accurate MRI-based monitoring. This approach is expected to contribute to the further advancement of these materials in personalized therapies.

References

1. Blanco-Andujar, C.; Walter, A.; Cotin, G.; Bordeianu, C.; Mertz, D.; Felder-Flesch, D.; Begin-Colin, S., Design of iron oxide-based nanoparticles for MRI and magnetic hyperthermia. *Nanomedicine* **2016,** *11* (14), 1889-910.
2. Jang, J. T.; Nah, H.; Lee, J. H.; Moon, S. H.; Kim, M. G.; Cheon, J., Critical enhancements of MRI contrast and hyperthermic effects by dopant-controlled magnetic nanoparticles. *Angew Chem Int Ed Engl* **2009,** *48* (7), 1234-8.
3. Song, L.; Yan, C.; Zhang, W.; Wu, H.; Jia, Z.; Ma, M.; Xie, J.; Gu, N.; Zhang, Y., Influence of Reaction Solvent on Crystallinity and Magnetic Properties of MnFe2O4 Nanoparticles Synthesized by Thermal Decomposition. *Journal of Nanomaterials* **2016,** *2016* (1), 4878935.
4. Provenzano, R.; Schiller, B.; Rao, M.; Coyne, D.; Brenner, L.; Pereira, B. J., Ferumoxytol as an intravenous iron replacement therapy in hemodialysis patients. *Clin J Am Soc Nephrol* **2009,** *4* (2), 386-93.
5. Park, Y.; Demessie, A. A.; Luo, A.; Taratula, O. R.; Moses, A. S.; Do, P.; Campos, L.; Jahangiri, Y.; Wyatt, C. R.; Albarqi, H. A.; Farsad, K.; Slayden, O. D.; Taratula, O., Targeted Nanoparticles with High Heating Efficiency for the Treatment of Endometriosis with Systemically Delivered Magnetic Hyperthermia. *Small* **2022,** *18* (24), e2107808.
6. Dutz, S.; Hergt, R., Magnetic nanoparticle heating and heat transfer on a microscale: Basic principles, realities and physical limitations of hyperthermia for tumour therapy. *Int J Hyperther* **2013,** *29* (8), 790-800.
7. Adibzadeh, F.; Paulides, M. M.; van Rhoon, G. C., SAR thresholds for electromagnetic exposure using functional thermal dose limits. *Int J Hyperther* **2018,** *34* (8), 1248-1254.
8. Kolhatkar, A. G.; Jamison, A. C.; Litvinov, D.; Willson, R. C.; Lee, T. R., Tuning the Magnetic Properties of Nanoparticles. *International Journal of Molecular Sciences* **2013,** *14* (8), 15977-16009.
9. Issa, B.; Obaidat, I. M.; Albiss, B. A.; Haik, Y., Magnetic Nanoparticles: Surface Effects and Properties Related to Biomedicine Applications. *Intl J Mol Sci* **2013,** *14* (11), 21266-21305.
10. Lavorato, G. C.; Das, R.; Alonso Masa, J.; Phan, M.-H.; Srikanth, H., Hybrid magnetic nanoparticles as efficient nanoheaters in biomedical applications. *Nanoscale Adv* **2021,** *3* (4), 867-888.
11. Wu, L.; Mendoza-Garcia, A.; Li, Q.; Sun, S., Organic Phase Syntheses of Magnetic Nanoparticles and Their Applications. *Chem Revs* **2016,** *116* (18), 10473-10512.
12. Cotin, G.; Perton, F.; Blanco-Andujar, C.; Pichon, B.; Mertz, D.; Bégin-Colin, S., Chapter 2 - Design of Anisotropic Iron-Oxide-Based Nanoparticles for Magnetic Hyperthermia. In *Nanomaterials for Magnetic and Optical Hyperthermia Applications*, Fratila, R. M.; De La Fuente, J. M., Eds. Elsevier: 2019; pp 41-60.
13. Jalili, H.; Aslibeiki, B.; Ghotbi Varzaneh, A.; Chernenko, V. A., The effect of magneto-crystalline anisotropy on the properties of hard and soft magnetic ferrite nanoparticles. *Beilstein J Nanotechnol* **2019,** *10*, 1348-1359.
14. Fantechi, E.; Campo, G.; Carta, D.; Corrias, A.; de Julián Fernández, C.; Gatteschi, D.; Innocenti, C.; Pineider, F.; Rugi, F.; Sangregorio, C., Exploring the Effect of Co Doping in Fine Maghemite Nanoparticles. *Jf Phy Chem C* **2012,** *116* (14), 8261-8270.

15. Dogan, N.; Dogan, O. M.; Irfan, M.; Ozel, F.; Kamzin, A. S.; Semenov, V. G.; Buryanenko, I. V., Manganese doped-iron oxide nanoparticles and their potential as tracer agents for magnetic particle imaging (MPI). *J Magn Magn Mater* **2022,** *561*, 169654.

16. Lee, J.-H.; Huh, Y.-M.; Jun, Y.-w.; Seo, J.-w.; Jang, J.-t.; Song, H.-T.; Kim, S.; Cho, E.-J.; Yoon, H.-G.; Suh, J.-S.; Cheon, J., Artificially engineered magnetic nanoparticles for ultra-sensitive molecular imaging. *Nat Med* **2007,** *13* (1), 95-99.

17. Liu, D.; Yang, W.; Zhang, B., Magnetic Resonance Imaging and Its Molecular Probes in Evaluating the Response to Tumor Treatment. *Nano Biomed Eng* **2024,** *17* (1), 36-55.

18. Yang, L.; Zhou, Z.; Liu, H.; Wu, C.; Zhang, H.; Huang, G.; Ai, H.; Gao, J., Europium-engineered iron oxide nanocubes with high T1 and T2 contrast abilities for MRI in living subjects. *Nanoscale* **2015,** *7* (15), 6843-6850.

19. Jeon, M.; Halbert, M. V.; Stephen, Z. R.; Zhang, M., Iron Oxide Nanoparticles as T(1) Contrast Agents for Magnetic Resonance Imaging: Fundamentals, Challenges, Applications, and Prospectives. *Adv Mater* **2021,** *33* (23), e1906539.

20. Jeun, M.; Lee, S.; Kyeong Kang, J.; Tomitaka, A.; Wook Kang, K.; Il Kim, Y.; Takemura, Y.; Chung, K.-W.; Kwak, J.; Bae, S., Physical limits of pure superparamagnetic Fe3O4 nanoparticles for a local hyperthermia agent in nanomedicine. *Appl Phys Lett* **2012,** *100* (9).

21. Maier, A.; van Oossanen, R.; van Rhoon, G. C.; Pignol, J.-P.; Dugulan, I.; Denkova, A. G.; Djanashvili, K., From Structure to Function: Understanding Synthetic Conditions in Relation to Magnetic Properties of Hybrid Pd/Fe-Oxide Nanoparticles. *Nanomaterials* **2022,** *12* (20), 3649.

22. van Oossanen, R.; Maier, A.; Godart, J.; Pignol, J. P.; Denkova, A. G.; van Rhoon, G. C.; Djanashvili, K., Magnetic hybrid Pd/Fe-oxide nanoparticles meet the demands for ablative thermo-brachytherapy. *Int J Hyperthermia* **2024,** *41* (1), 2299480.

23. Maier, A.; Djanashvili, K.; Denkova, A. G.; van Rhoon, G. C.; Pignol, J.-P.; van Oossanen, R., Synthesis of Hybride Palladium(103)/Iron Oxide Nanoparticles for Thermobrachy Therapy. *European Patent Application No. 2029314* **2021**.

24. Sytnyk, M.; Kirchschlager, R.; Bodnarchuk, M. I.; Primetzhofer, D.; Kriegner, D.; Enser, H.; Stangl, J.; Bauer, P.; Voith, M.; Hassel, A. W.; Krumeich, F.; Ludwig, F.; Meingast, A.; Kothleitner, G.; Kovalenko, M. V.; Heiss, W., Tuning the Magnetic Properties of Metal Oxide Nanocrystal Heterostructures by Cation Exchange. *Nano Letters* **2013,** *13* (2), 586-593.

25. Lin, F.-h.; Chen, W.; Liao, Y.-H.; Doong, R.-a.; Li, Y., Effective approach for the synthesis of monodisperse magnetic nanocrystals and M-Fe3O4 (M = Ag, Au, Pt, Pd) heterostructures. *Nano Res* **2011,** *4* (12), 1223-1232.

26. Mazumder, V.; Sun, S., Oleylamine-Mediated Synthesis of Pd Nanoparticles for Catalytic Formic Acid Oxidation. *J Am Cheml Soc* **2009,** *131* (13), 4588-4589.

27. Fantechi, E.; Roca, A. G.; Sepúlveda, B.; Torruella, P.; Estradé, S.; Peiró, F.; Coy, E.; Jurga, S.; Bastús, N. G.; Nogués, J.; Puntes, V., Seeded Growth Synthesis of Au–Fe_3O_4 Heterostructured Nanocrystals: Rational Design and Mechanistic Insights. *Chem Mater* **2017,** *29* (9), 4022-4035.

28. Sun, S.; Zeng, H.; Robinson, D. B.; Raoux, S.; Rice, P. M.; Wang, S. X.; Li, G., Monodisperse MFe2O4 (M = Fe, Co, Mn) Nanoparticles. *J Am Chem So* **2004,** *126* (1), 273-279.

29. Mohapatra, J.; Xing, M.; Liu, J. P., Magnetic and hyperthermia properties of CoxFe3-xO4 nanoparticles synthesized via cation exchange. *AIP Advances* **2018,** *8* (5).

30. Jin, Y.; Jia, C.; Huang, S.-W.; O'Donnell, M.; Gao, X., Multifunctional nanoparticles as coupled contrast agents. *Nat Commun* **2010,** *1* (1), 41.

31. Barral, J. K.; Gudmundson, E.; Stikov, N.; Etezadi-Amoli, M.; Stoica, P.; Nishimura, D. G., A robust methodology for in vivo T1 mapping. *Magn Reson Med* **2010,** *64* (4), 1057-67.

32. Song, Q.; Ding, Y.; Wang, Z.; John, Z., Tuning the Thermal Stability of Molecular Precursors for the Nonhydrolytic Synthesis of Magnetic $MnFe_2O_4$ Spinel Nanocrystals. *Cheminform* **2007,** *38*.

33. Verwey, E. J. W., Electronic Conduction of Magnetite (Fe_3O_4) and its Transition Point at Low Temperatures. *Nature* **1939,** *144* (3642), 327-328.

34. He, K.; Chen, N.; Wang, C.; Wei, L.; Chen, J., Method for Determining Crystal Grain Size by X-Ray Diffraction. *Cryst. Res. Technol.* **2018,** *53* (2), 1700157.

35. Mornet, S.; Vasseur, S.; Grasset, F.; Duguet, E., Magnetic nanoparticle design for medical diagnosis and therapy. *J Mater Chem.* **2004,** *14* (14), 2161-2175.

36. Ganapathe, L. S.; Mohamed, M. A.; Mohamad Yunus, R.; Berhanuddin, D. D., Magnetite (Fe3O4) Nanoparticles in Biomedical Application: From Synthesis to Surface Functionalisation. *Magnetochemistry* **2020,** *6* (4), 68.

37. Li, M.; Bao, J.; Zeng, J.; Huo, L.; Shan, X.; Cheng, X.; Qiu, D.; Miao, W.; Zhu, X.; Huang, G.; Ni, K.; Zhao, Z., Engineering manganese ferrite shell on iron oxide nanoparticles for enhanced T1 magnetic resonance imaging. *J Coll Interface Sci* **2022,** *626*, 364-373.

38. Stefani, C.; Langenberg, E.; Cordero-Edwards, K.; Schlom, D. G.; Catalan, G.; Domingo, N., Mechanical reading of ferroelectric polarization. *J Appl Phys* **2021,** *130* (7).

39. Kielhorn, J.; Melber, C.; Keller, D.; Mangelsdorf, I., Palladium--a review of exposure and effects to human health. *Int J Hyg Environ Health* **2002,** *205* (6), 417-32.

40. Evans, G. R.; Masullo, L. N., Manganese Toxicity. In *StatPearls*, StatPearls Publishing

Copyright © 2024, StatPearls Publishing LLC.: Treasure Island (FL) ineligible companies. Disclosure: Lawrence Masullo declares no relevant financial relationships with ineligible companies., 2024.

41. Keen, C. L.; Zidenberg-Cherr, S., MANGANESE. In *Encyclopedia of Food Sciences and Nutrition (Second Edition)*, Caballero, B., Ed. Academic Press: Oxford, 2003; pp 3686-3691.

42. Mohammadi, Z.; Shalavi, S.; Jafarzadeh, H., Ethylenediaminetetraacetic acid in endodontics. *Eur J Dent* **2013,** *7* (Suppl 1), S135-s142.

3

Adaptive Design of Ho-doped Iron Oxide Nanoparticles: Composition-Structure-Property Insights for Enhanced Magnetic Heating

Introduction

The superior heating properties of magnetic nanoparticles (MNPs) when exposed to alternating magnetic fields (AMF) have led to extensive research into the mechanisms governing this process. This in turn has attracted interest in superparamagnetic iron oxide (Fe-oxide) NPs consisting of magnetite (Fe_3O_4) and/or maghemite (Fe_2O_3),[1] as excellent candidates for magnetic hyperthermia (MHT), a promising treatment method based on raising the temperature in cancer tissue to approximately 42 ºC.[2, 3] Another method using elevated temperatures generated by MNPs is thermal ablation, which involves higher local temperatures (>50 ºC) capable of destroying tumor cells in a non-invasive way, unlike traditional surgery. One way to achieve this goal is to inject rationally designed MNPs directly into the tumor, which significantly lowers toxicity to healthy organs and decreases general side effects compared to the intravenous administration of therapeutics.[4, 5]

To evaluate the heating efficiency of MNPs, the specific heat absorption rate (SAR) and specific loss power (SLP), both expressed in watts per gram of magnetic material, [1] are key parameters that quantify energy dissipation via Brownian and Néel relaxation mechanisms.[6, 7] The subsequent temperature increase triggers a series of biological responses, including upregulation of heat shock proteins, irreversible cell necrosis, vessel thrombosis and ischaemia.[8, 9] Furthermore, hyperthermia can sensitize cells to other therapeutic modalities, such as chemo- or radiotherapy. An example of such an adjuvant application of hyperthermia is blood flow modulation, which not only accelerates the delivery of cytostatic drugs and improves the effect on chemotherapy, but also increases the availability of oxygen in cancer cells.[10] Since tumor hypoxia is associated with radio-resistance, higher oxygen levels in turn sensitize tumors to radiotherapy.[11] Hyperthermia may also enhance the immune response by stimulating the recruitment of immune effector cells into the tumor, increasing the cytotoxicity of immune cells against malignant cells, and upregulating various proinflammatory cytokines and cell surface molecules.[12] Therefore, in addition to serving as a standalone therapeutic modality, MHT also holds potential for use in combination with other treatments in a synergistic approach.

Previously, we have developed core-shell Pd/Fe-oxide NPs for combined hyperthermia and radiotherapy envisioned by incorporation of ^{103}Pd radioisotope.[13, 14] In addition to the safe encapsulation of the radioisotopes, the advantage of a core-shell structure is the ability to combine two functional elements in one NP without interference with their individual properties, which is especially important for magnetic properties that are sensitive to even minor structural/morphological alternations.[15] However, the preparation of core-shell structures requires harsh conditions and extra surface-exchange steps in order to make them water dispersible. Doping the Fe-oxide lattice represents an attractive alternative that eliminates the need for additional synthesis steps, although it carries the risk of degrading the magnetic properties when using a non-magnetic dopant.[16] An elegant solution is to dope the Fe-oxide NPs with other magnetic ions, which may lead to enhanced magnetic properties, as shown by

doping Fe-oxide with Co^{2+}, which increased the saturation magnetization saturation (M_S) of the resulting $CoFe_2O_4$ NPs to 92 emu/g.[17] In our hands, doping with paramagnetic Mn^{2+} increased the M_S and SLP values of Pd/Fe-oxide NPs 1.7 times compared to the undoped analogs.[13]

In this study, we investigate the effectiveness of holmium (Ho) doping in Fe-oxide NPs via an optimized coprecipitation method and examine how varying Ho-doping levels influence their magnetic properties. As a member of the lanthanide series, holmium possesses one of the highest magnetic moments (μ_{eff} = 10.6μB per Ho^{3+} ion), which can substantially enhance magnetic anisotropy in ferrites through strong 4*f*-3*d* exchange interactions.[18] The paramagnetic properties of Ho have been considered for the application in magnetic resonance imaging (MRI),[19] while its high density makes it useful for computed tomography (CT). The radiotherapeutic potential Ho-doped NPs lies in the ability to incorporate ^{166}Ho, which is a therapeutic radioisotope ($T_{1/2}$ = 26.8 h) that decays to stable ^{166}Er, emitting high-energy β-particles ($E_{max} \approx$ 1.85 MeV) with an average soft tissue penetration depth of ~ 3.2 mm, along with γ-emission at 80.57 keV (6.7%) suitable for imaging purposes.[20-22]

However, the larger radius of Ho^{3+} ion (1.01 Å) compared to the Fe^{3+} ion (0.79 Å) can lead to core anisotropy and alterations in the crystallographic lattice with the subsequent deterioration of the magnetic properties. Doping of Fe-oxide with Ho^{3+} ions therefore requires a thorough understanding of the process and the resulting magnetic/heating properties of hybrid Ho/Fe-oxide NPs with improved morphology and dispersity. Understanding the interplay between key parameters such as size, morphology and composition leads to an adaptive design that takes these essential parameters into account.

Materials and methods

Chemicals

Iron (II) chloride tetrahydrate ($FeCl_2 \cdot 4H_2O$), iron (III) chloride hexahydrate ($FeCl_3 \cdot 6H_2O$), 25% ammonia, sodium hydroxide (NaOH), polyvinylpyrrolidone (PVP) and ethanol were purchased from Sigma Aldrich (Merck, St. Louis, MO, USA), holmium chloride hexahydrate ($HoCl_3 \cdot 6H_2O$) was purchased from Strem (Newburyport, USA). All chemicals were of analytical grade and were used without further purification.

Synthesis of Ho doped iron oxide nanoparticles (Ho/Fe-oxide NPs)

Iron oxide NPs were prepared based on previously published protocols with minor modification[23-25]. In a typical method, $FeCl_2 \cdot 4H_2O$ (198.8 mg, 1 mmol) and PVP (250 mg) were dispersed in 10 mL water and ultrasonicated for 15 min, after which $FeCl_3 \cdot 6H_2O$ (540.6 mg, 2 mmol) in 5 mL water was added and the mixture was heated to 60 °C under vigorous stirring. After the subsequent drop-wise addition of 1.25 mL ammonia and stirring the mixture for another 60 min, the NPs were

collected with a magnet, washed with water/ethanol several times and dispersed in water (10 mg/mL) for further use. The same procedure was applied to synthesize Ho/Fe-oxide NPs where x% of $FeCl_3 \cdot 6H_2O$ was replaced by $HoCl_3 \cdot 6H_2O$ (x = 0.1, 0.25, 0.5, 1 , 2.5, and 5%). The obtained Ho/Fe-oxide NPs were denoted as x% Ho/Fe-oxide NPs. Three selected compositions with x = 0, 2.5, and 5% were used to prepare NPs at room temperature (x% Ho/Fe-oxide-rt NPs).

Physical methods

Particle size, size distribution and morphology of the samples were determined by transmission electron microscopy (TEM), using a 120 kV Jeol-JEM1400 microscope. The samples were prepared by drop-casting a diluted NP suspension on a Quantifoil R1.2/1.3 Cu300 grid and evaporating the solvent at room temperature. Statistical analysis of around 100-500 NPs, using TEM images and Nano Measurer 1.2 software was performed to calculate the mean diameter and the size distribution of the samples. The high resolution-TEM images and elemental mapping analysis were done with Titan aberration-corrected Transmission Electron Microscope (Thermo Fisher, FEI) on the same grids used for TEM.

The heating measurements were performed using the Magnetherm Digital device manufactured by Nanotherics, with a 60 mm coil at alternating magnetic field with a frequency of 338 kHz and a field strength of 18 mT, used for the calculation of the SLP values. The device was equipped with two glass-fiber optic thermometers (Osensa PRB-G40_2.0-STM-MRI) to measure the temperature at the core (used for SLP) and bottom (to check for a possible precipitation) of the sample. For the heating measurement, an Eppendorf tube containing approximately 5 mg/mL of NPs was inserted in an insulated sample holder to reduce heat loss to the environment, which was then placed in the middle of the coil. The temperature was allowed to equilibrate until it varied less than 0.5 °C/min before the start of the measurement. The SLP values of the samples, expressed in W/g_{Fe+Ho}, were calculated using the concentrations of Fe and Ho obtained from the Inductively Coupled Plasma-Mass Spectrometry (ICP-MS) data performed on the same samples after microwave destruction of NPs dispersed in a 5% solution of HNO_3.

Magnetic properties were assessed by superconducting quantum interference device (SQUID), using an MPMS XL magnetometer (Quantum Design) with 2-3 mg of dry NPs. Continuously varying magnetic field up to a maximum of ±60 kOe at 5 and 300 K was applied to obtain saturation magnetization and coercivity. Transmission ^{57}Fe Mössbauer spectra were obtained using a ^{57}Co(Rh) source at 4.2 K with a conventional constant-acceleration spectrometer. Velocity calibration was carried out using an α-Fe foil and the final Mössbauer spectra were fitted using the Mosswinn 4.0 program. Powder X-ray diffraction (XRD) pattern was measured with a PANalytical X'Pert Pro PW3040/60 diffractometer from 10° to 90° at 45 kV and 40 mA (Cu Kα radiation, λ = 1. 54 Å).

Results and Discussion

Synthesis and characterization of Ho/Fe-oxide NPs

Within the different strategies to fuse iron oxide with other metals in one nanoparticle (NP), two main synthesis routes, each offering specific advantages, can be distinguished: thermal decomposition and co-precipitation. Thermal decomposition typically produces crystalline NPs of uniform size and well-defined morphologies, and enables the construction of core-shell architectures if required by the application, as was the case with our previously reported Mn-doped Pd/Fe-oxide NPs.[13] However, this method is characterized by low yields and involves the use of high temperatures, organic solvents and surfactants, which in turn necessitates additional steps of surface modification with hydrophilic groups to impart water dispersibility to the final NPs. In the present study, which is aimed at generating homogeneous hybrid NPs, the co-precipitation method proved particularly suitable, as it promotes the simultaneous nucleation and growth of both Ho and Fe ions within a single lattice. Such atomic-level mixing enables a reliable correlation between composition, structure, and magnetic heating performance, while the yield of water dispersible Ho/Fe-oxide NPs can be readily increased by adjusting reagent rations. A known drawback of this method is the production of particles with less uniform morphology.[26] Our initial attempt to apply a conventional co-precipitation procedure to achieve Ho-doping into Fe-oxide resulted in NPs with the size of 12.5±5.3 nm (1% Ho) and a relatively broad size distribution (Figure 3.1A,B). For 10% Ho-doped NPs, determination of size and its distribution was not possible due to heavy aggregation, as shown in TEM images (Figure 3.1C).

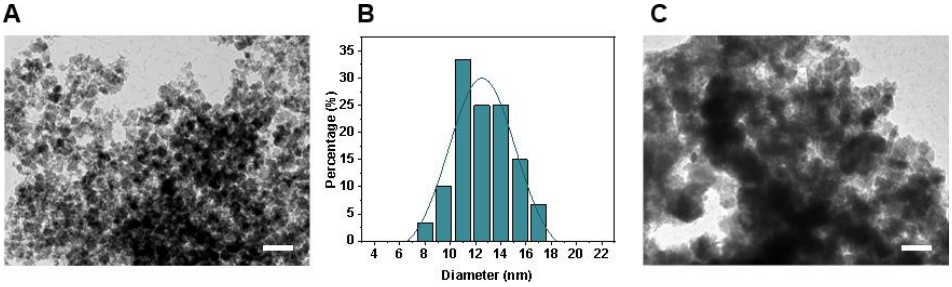

Figure 3.1. Analysis of Ho/Fe-oxide NPs prepared by conventional co-precipitation procedure ($FeCl_2$/$FeCl_3$, H_2O/NH_4OH, RT): TEM image of 1% Ho-doping (**A**) with determined size-distribution (**B**) and 10% Ho-doping (**C**) without size-distribution due to the severe aggregation. The scale bars are set to 50 nm.

Mitigation of this problem becomes very important considering magnetic properties of the NPs and the associated heating effect, which are known to depend on size, crystallinity, and dispertion.[5] Although the reported optimal diameter of iron oxide NPs varies in the literature and depends on the amplitude of the applied magnetic field, particles in the 12-20 nm range are generally considered to exhibit the best heating performance.[5, 27, 28] Low crystallinity in MNPs, caused by surface and internal defects, induces magnetic disorder and effectively reduces their magnetic

volume relative to crystal volume. This can lead to diminishing the SLP and overall heating efficiency. Aggregation can further compromise performance through interparticle interactions. Unless a chain-like assembly is formed, these interactions are typically detrimental.[5, 29] Strong antiferromagnetic coupling within aggregated MNPs leads to magnetic frustration during the relaxation of individual magnetic moments, causing a demagnetization effect that ultimately inhibits their thermal efficiency. Based on the co-precipitation synthesis mechanism, improvement of these factors can be tackled through several approaches: i) increasing reaction temperatures and reaction times are to facilitate better ripening of NPs, and thus, better crystallinity; ii) increasing stirring rates to induce smaller NPs; and iii) adding surfactants to prevent aggregation.

Based on these considerations, x% Ho/Fe-oxide NPs (x = 0, 0.1, 0.25, 0.5, 1, 2.5 and 5%) were synthesized at 60 °C under vigorous stirring in the presence of a PVP-surfactant. The obtained undoped NPs exhibited a similar size (11.2 vs 10.2 nm) but showed markedly improved size distribution and dispersibility compared to those prepared by the conventional co-precipitation method (Figure 3.2). Increasing Ho-doping from 0.1 to 2.5% (Figure 3.3A-E) yielded NPs ranging from 10.2 to 13.6 nm, with good dispersity attributed to the presence of PVP. However, at the highest Ho-doping level of 5% , the particle size increased substantially (17.9±4.9 nm), and both size distribution and morphology were notably poorer (Figure 3.1F).

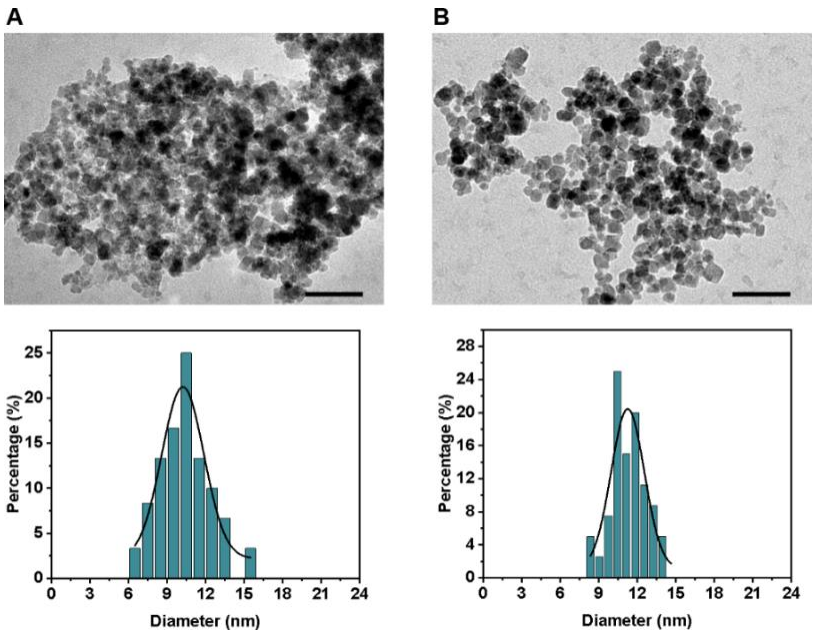

Figure 3.2. TEM images and size distributions of Fe-oxide NPs prepared by (**A**) conventional and (**B**) modified co-precipitation method (60 °C, vigorous stirring, PVP). The scale bars are set to 50 nm.

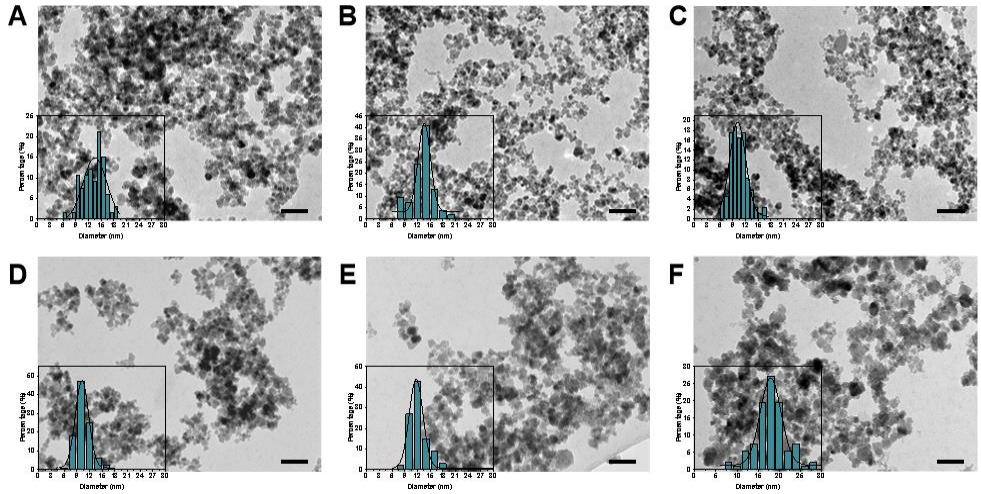

Figure 3.3. TEM images of Ho/Fe-oxide NPs prepared by a modified co-precipitation method (60 °C, vigorous stirring, PVP) with the Ho-doping varied as: 1% (**A**), 0.25% (**B**) 0.5% (**C**), 1% (**D**), 2.5% (**E**), 5% (**F**). The scale bars are set to 50 nm.

Heating performance of Ho/Fe-oxide NPs

Following the synthesis and characterization of Ho-doped Fe-oxide NPs, the effect of varying Ho-content on their magnetic heating performance under AMF was investigated. For this purpose, 1 mL of x% Ho/Fe-oxide NPs dispersions (5 mg/mL) were pipetted into Eppendorf tubes and placed in the Nanotherm device, set to a frequency of 338 kHz and a maximum field strength of 18 mT. The temperature increase in the presence of the NPs was monitored for 10 min, and the resulting curves, representing the temperature difference (ΔT) and the corresponding SLP values calculated using Ho- and Fe-concentrations obtained with ICP-MS, are shown in Figure 3.4 and Table 3.1. As expected, the lowest ΔT of ±19 ºC was observed for the 0% Ho/Fe-oxide NPs. However, no clear relationship was found between ΔT and Ho-content (Figure 3.4A). Interestingly, considering the average particle size as an accompanying parameter (Figure 3.4B), it can be seen that up to 0.5% Ho-doping increases in both ΔT and SLP are primarily correlated with the corresponding increase in NP size. Since NPs size is a dominant intrinsic factor affecting SLP, Ho-incorporation at levels ≤0.5% does not significantly influences heating performance, which remains size-governed. At 1% Ho-doping, both SLP and ΔT exhibit slight enhancements despite a reduction in NP size, suggesting a growing contribution of Ho. Notably, the highest SLP (176.38 W/g_{Fe+Ho}) is observed for 2.5% Ho-doping, where NP size (11.7 ± 3.3 nm), magnetocrystalline/shape anisotropy and surface functionalization are comparable to those of undoped 0% Ho/Fe-oxide NPs (11.2 ± 2.6 nm). This strongly indicates that the improved heating performance at this level is primarily attributable to Ho-incorporation rather than size effects. At 5% Ho-doping, however, the observed increase in SLP cannot be unambiguously assigned to either Ho-content of particle size, as both parameters vary significantly, complicating interpretation.

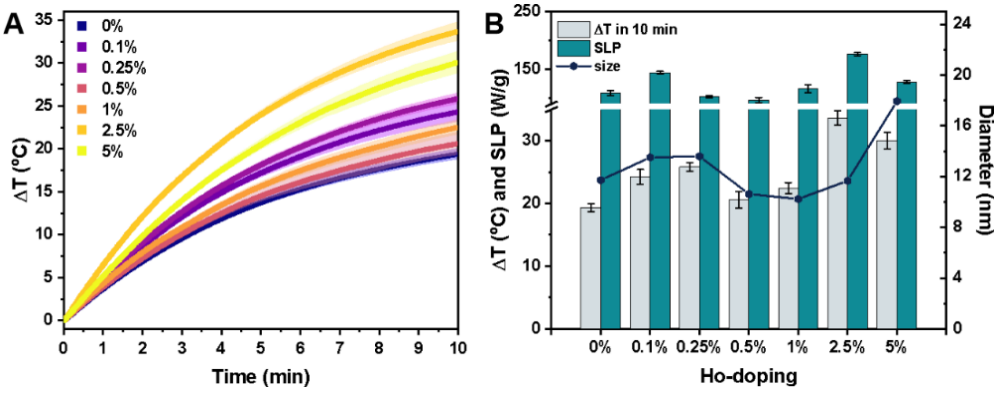

Figure 3.4. Investigation of magnetic heating performance of x% Ho/Fe-oxide NPs (1 mg/mL) under AMF (338 kHz/18mT): (**A**) temperature change (ΔT) in 10 min and (**B**) correlation between ΔT, SLP and size within the series of Ho-doped NPs. The line connecting the sizes serves as a guide for the eyes.

Table 3.1. Overview of the magnetic properties of % Ho/Fe-oxide NPs: saturation magnetization (M_s) at 50 kOe, T = 5 K and 300 K, and coercivity (H_c) at T = 5 K and 300 K.

Ho/Fe-oxide NPs (% Ho)	Size (nm)	Saturation Magnetization (M_s) (emu/g)		Coercivity (H_c) (Oe)		SLP[a] ($W/g_{Ho,Fe}$)
		5 K	300 K	5 K	300 K	
0	11.2±2.6	62.0	54.1	51.7	11.5	109.18
0.1	13.5±5.7	61.4	53.7	78.9	12.3	144.09[b]
0.25	13.6±3.0	72.8	63.1	91.5	11.1	102.61
0.5	10.2±3.8	66.2	56.7	207.8	10.4	96.69
1	10.2+3.2	69.8	58.9	169.9	11.9	116.45
2.5	11.7±3.3	79.0	64.9	134.2	7.3	176.38
5	17.9±4.9	71.1	55.2	83.2	9.0	128.06

[a] Calculated considering a collective contribution of Ho- and Fe-content determined by ICP-MS; [b] the relatively high SLP can be attributed to the inaccuracy of the ICP-measurement at low Ho-content.

Physical property studies

To understand the abovementioned phenomena, the static magnetic behavior of x% Ho/Fe-oxide NPs was investigated by SQUID magnetometry. Dry MNPs with varied Ho-doping were exposed to a magnetic field increasing in the range of –50 to 50 kOe and their saturation magnetization (M_S) was measured at 5 and 300K. Compared to the M_S of the Fe-oxide NPs (62.0 and 54.1 emu/g at 5K and 300K, respectively), slightly higher M_S were obtained for all Ho-doped NPs, with the highest values of 79.0 and 64.9 emu/g for 2.5% Ho/Fe-oxide NPs at 5 and 300K, respectively (Figure 3.5). Similar to the SLP and ΔT correlations, the same dependence on NP size was observed for M_S values within the Ho-doping range of 0 - 0.5% (Figure 3.6). This suggests that the size and composition of NPs have a profound influence on their magnetic properties and heating characteristics.

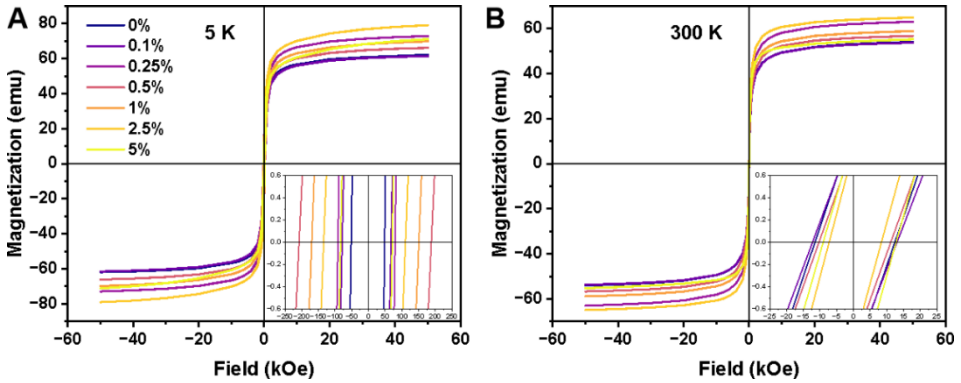

Figure 3.5. SQUID magnetometry performed with dry powders of Ho/Fe-oxide NPs to obtain magnetizations (emu/g) and coercivities (H_c) in the insets): **(A)** $M(H)_T$ curves measured at 5 K (the inset represents 240× magnification of the y-axis); **(B)** $M(H)_T$ curves at 300 K; the inset represents 2400× magnification of the y-axis.

To investigate the interplay between Ho and Fe-oxide that leads to the distinctly superior magnetic and thus heating behavior of the 2.5% Ho/Fe-oxide NPs despite their smaller size, Mössbauer spectroscopy and XRD analysis were performed. The hyperfine parameters of Fe in 0% , 2.5% and 5% Ho/Fe-oxide NPs obtained at 4.2 K (Table 3.2), together with the Mössbauer spectra (Figure 3.7A) fitted with two Fe^{3+} contributions, both indicated the presence of maghemite (γ-Fe_2O_3) species. The different hyperfine magnetic fields (Γ) observed for all NPs can be explained by the coexistence of both bigger larger and smaller species, consistent with the TEM images obtained after co-precipitation synthesis. Compared to 0% Ho/Fe-oxide NPs, a remarkable decrease in the hyperfine magnetic field was observed for 2.5% Ho-doped NPs, which may indicate the substitution of Ho in the Fe-lattice leading to stronger interactions between magnetic ions, which in turn causes an increase in the corresponding line widths.[30]

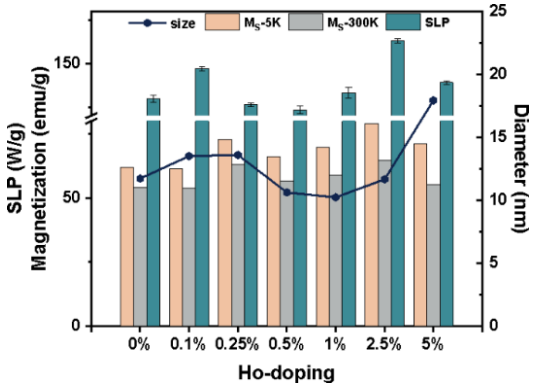

Figure 3.6. Correlation between the size and magnetic properties of x% Ho/Fe-oxide NPs expressed as saturation magnetization (M_s) at 50 kOe, measured at 5/300 K and calculated SLP. The line connecting the sizes serves as a guide for the eyes.

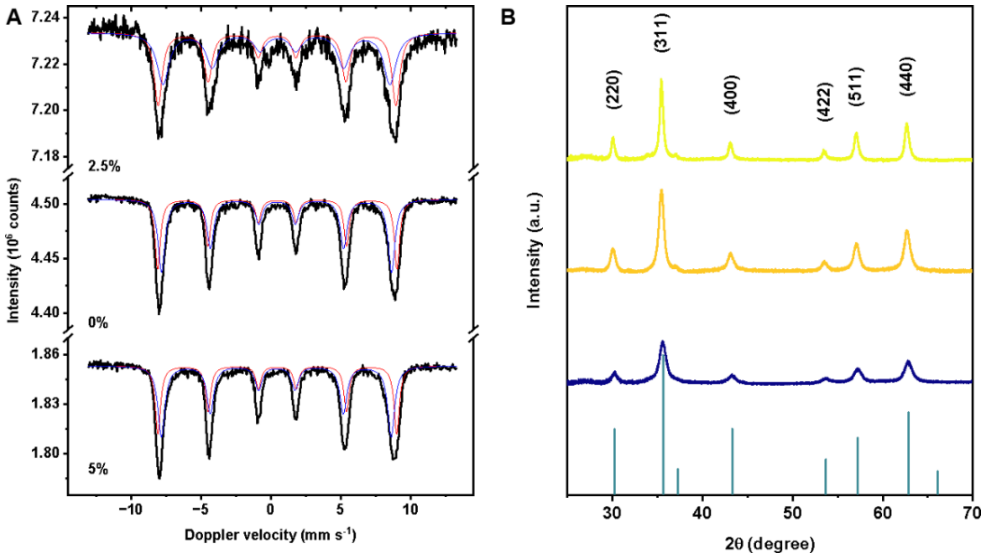

Figure 3.7. Characterization of x% Ho/Fe-oxide NPs (x= 0, 2.5, 5%): (**A**) Mössbauer spectra obtained at 4.2 K and **(B)** XRD patterns.

Table 3.2. The Mössbauer fitted parameters of the Ho/Fe-oxide samples at 4.2 K.

Ho/Fe-oxide NPs (% Ho)	IS (mm s^{-1})	QS (mm s^{-1})	Hyperfine field (T)	Γ (mm s^{-1})	Phase	Spectral contribution (%)
0	0.47	0.01	53.18	0.45	γ-Fe_2O_3	42.4
	0.43	-0.03	51.12	0.59	γ-Fe_2O_3 (smaller)	57.6
2.5	0.45	0.00	58.82	0.69	γ-Fe_2O_3	48.2
	0.46	-0.10	40.43	1.05	γ-Fe_2O_3 (smaller)	51.8
5	0.47	0.00	53.07	0.45	γ-Fe_2O_3	42.0
	0.41	-0.04	51.07	0.60	γ-Fe_2O_3 (smaller)	58.0

Experimental uncertainties: Isomer shift: IS ± 0.02 mm s^{-1}; Quadrupole splitting: QS ± 0.02 mm s^{-1}; Line width: Γ ± 0.03 mm s^{-1}; Hyperfine field: ± 0.1 T; Spectral contribution: ± 3%.

Both of these features were however not observed in the spectrum of 5% Ho/Fe-oxide NPs, suggesting that Ho incorporation into the Fe-oxide lattice is very limited. While ICP-MS analysis confirmed that 5% Ho is indeed present in the NPs and likely in contact with Fe, it does not necessarily mean the presence of a fully mixed phase. This estimation is consistent with our previous work on Mn|Pd/Fe-oxide NPs, where higher Mn-doping levels led to segregation of Mn and the formation of a rim on the NP surface.[13] This effect could also be observed by elemental mapping, which showed a uniform distribution of Ho within 2.5% Ho/Fe-oxide NPs in contrast to aggregation of Ho at the surface at a higher doping level of 5% (Figure 3.8).

In addition to the dopant concentration and its substitution mode in the Fe-oxide lattice, particle size can also influence hyperfine magnetic field.[31] To examine this effect, we considered both the sizes of the Ho-doped NPs from TEM images and the grain sizes calculated from XRD. The XRD

patterns (Figure 3.7B) suggested that all three samples were typical maghemite, corresponding to the standard card of γ-Fe_2O_3 (JCPDS: 01-078-6916). The grain sizes of 0% , 2.5% and 5% Ho/Fe-oxide NPs calculated using Scherrer equation with the peaks in 2θ=30-50º,[32] amounted 9.3, 11.3, and 16.6 nm, respectively, which is comparable to the statistical results from TEM (11.2, 11.7, and 17.9 nm). Unfortunately, XRD proved to be less useful for observing Ho-aggregation at the surface of 5% -doped NPs, which was previously seen in elemental mapping images, likely due to the amorphous nature or insufficient thickness of the layer.

These findings yield a hypothesis that, for 0% and 2.5% Ho/Fe-oxide NPs with similar particle and grain sizes, the observed decrease in hyperfine magnetic field of the latter can be primarily attributed to the Ho-substitution, which increases magnetic anisotropy and, consequently, enhances magnetic properties and heating performance. In the case of 5% Ho/Fe-oxide NPs, the higher Ho-doping level and the larger NPs and grain size are likely to cause a decrease and an increase in the hyperfine magnetic field, respectively, resulting in mutually offsetting effects.

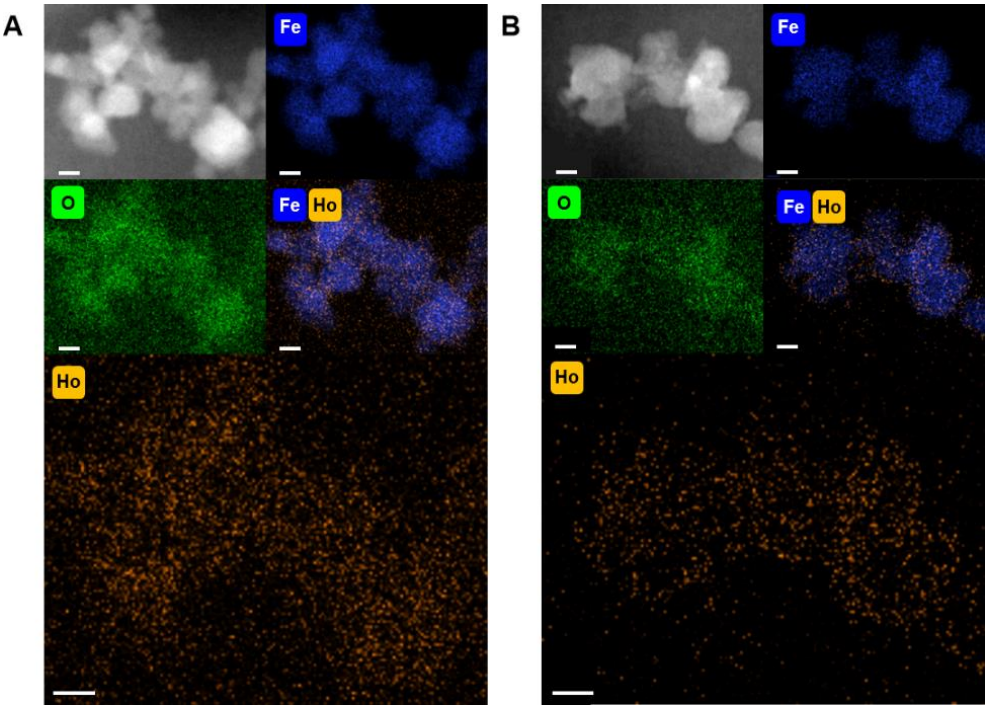

Figure 3.8. HR-TEM and EDS elemental mapping with individual signals for Fe (blue), O (green), and Ho (orange) of **(A)** 2.5% Ho/Fe-oxide and **(B)** 5% Ho/Fe-oxide NPs.

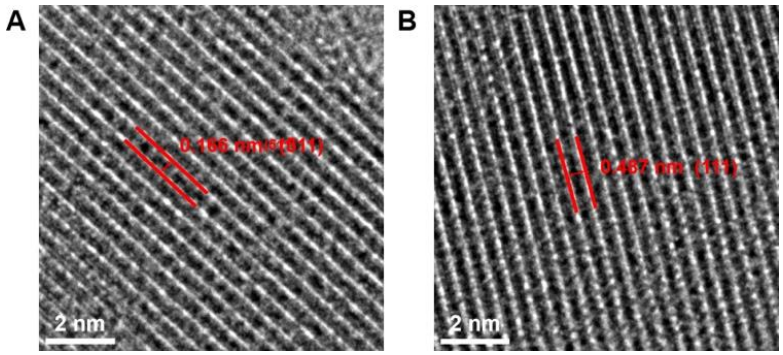

Figure 3.9. HR-TEM images of **(A)** 2.5% Ho/Fe-oxide and **(B)** 5% Ho/Fe-oxide NPs.

The High-Resolution Transmission Electron Microscopy (HR-TEM) revealed (111) and (511) face of γ-Fe_2O_3 for 2.5% Ho/Fe-oxide NPs and 5% Ho/Fe-oxide NPs, respectively (Figure 3.9). While the higher interplanar distance of 0.166 nm (A) compared to 0.487 nm (B) could be attributed to the higher Ho-doping, the elemental mapping analysis suggested that both samples contained Fe, O and Ho (Figure 3.8).

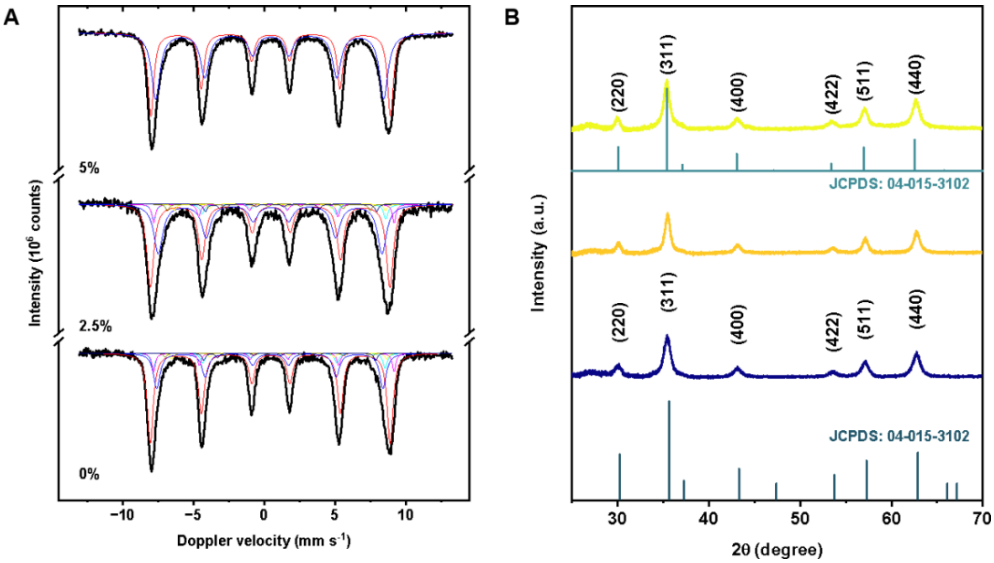

Figure 3.10. Characterization of % Ho/Fe-oxide-rt NPs (% = 0, 2.5, 5): (**A**) Mössbauer spectra obtained at 4.2 K and **(B)** XRD patterns.

Having established the structural, magnetic, and heating properties of the Ho-doped Fe-oxide NPs, we then attempted to address a rather unexpected resulting composition of the NPs that predominantly contained maghemite rather than expected magnetite. To clarify this discrepancy, we returned to the synthesis and looked into possible effects of the temperature on the maghemite formation, since Fe^{2+} is known to be sensitive to heat, which in our case was applied during 1h. Therefore, new batches of 0% , 2.5% and 5% Ho/Fe-oxide NPs were synthesis at room temperature (Ho/Fe-oxide-rt NPs) and the Mössbauer spectra showed the presence of 20.28% and 16.77% of magnetite next to maghemite in 0% and 2.5% Ho/Fe-oxide-rt NPs, respectively (Figure 3.10A). This, however, was not the case for 5% Ho/Fe-oxide-rt NPs.

Interestingly, the grain sizes of 0% and 2.5% Ho/Fe-oxide-rt NPs, calculated with from the XRD patterns (Figure 3.10B), were comparable to those of the NPs prepared under heating, whereas the 5% Ho/Fe-oxide-rt NPs exhibited a smaller grain size (9.9 nm). this comparison made it possible to separate the effects of particle size and Ho-doping level, identifying the latter as the primary factor influencing the hyperfine magnetic field. However, this relatively small decrease observed despite a 2-fold Ho-content further supports the earlier hypothesis that Ho-incorporation into the Fe-oxide lattice is only partial in the 5% Ho-doped NPs.

Table 3.3. The Mössbauer fitted parameters of the Ho/Fe-oxide-rt samples at 4.2 K.

Ho/Fe-oxide-rt NPs (% Ho)	IS (mm s^{-1})	QS (mm s^{-1})	Hyperfine field (T)	Γ (mm s^{-1})	Phase	Spectral contribution (%)
0	0.45	-0.04	52.63	0.50	γ-Fe_2O_3	55.16
	0.43	-0.06	49.63	0.57	γ-Fe_2O_3 (smaller)	24.56
	0.37	-0.04	50.91	0.37	Fe^{3+} (Fe_3O_4, A)	9.91
	0.51	0.34	52.75	0.30	Fe^{3+} (Fe_3O_4, B_1)	6.90
	0.81	0.50	47.21	0.30	Fe^{2+} (Fe_3O_4, B_2)	2.22
	0.84	-1.10	45.21	0.30	Fe^{2+} (Fe_3O_4, B_2)	1.59
	1.02	1.57	37.72	0.30	Fe^{2+} (Fe_3O_4, B_3)	2.67
2.5	0.46	-0.07	52.55	0.59	γ-Fe_2O_3	47.05
	0.45	-0.05	49.09	0.76	γ-Fe_2O_3 (smaller)	36.18
	0.37	0.05	50.91	0.37	Fe^{3+} (Fe_3O_4, A)	5.39
	0.49	0.40	52.75	0.30	Fe^{3+} (Fe_3O_4, B_1)	5.46
	0.78	0.66	46.36	0.30	Fe^{2+} (Fe_3O_4, B_2)	1.87
	0.89	-1.10	44.49	0.30	Fe^{2+} (Fe_3O_4, B_2)	1.91
	1.15	1.49	37.56	0.30	Fe^{2+} (Fe_3O_4, B_3)	2.14
5	0.46	0.00	52.57	0.49	γ-Fe_2O_3	46.17
	0.43	-0.07	50.02	0.73	γ-Fe_2O_3 (smaller)	53.83

Experimental uncertainties: Isomer shift: IS ± 0.02 mm s^{-1}; Quadrupole splitting: QS ± 0.02 mm s^{-1}; Line width: Γ ± 0.03 mm s^{-1}; Hyperfine field: ± 0.1 T; Spectral contribution: ± 3%.

Surprisingly, the M_S values of the NPs prepared at room temperature were found to be significantly lower than those of the analogues prepared under 1h heating (Figure 3.11 and Table 3.4). For the 5% Ho-Fe-oxide-rt NPs with the same γ-Fe_2O_3 composition as the 5% Ho-Fe-oxide-NPs, this decrease in M_S can be explained by their smaller size (9.9 vs 17.9 nm). However, this is not the case for 0% and 2.5% Ho/Fe-oxide-rt NPs, since their sizes were unaffected when synthesized at room temperature. This leads to the conclusion that maghemites are more prone to improvements in magnetic properties and heating capacity upon Ho-doping than magnetites.

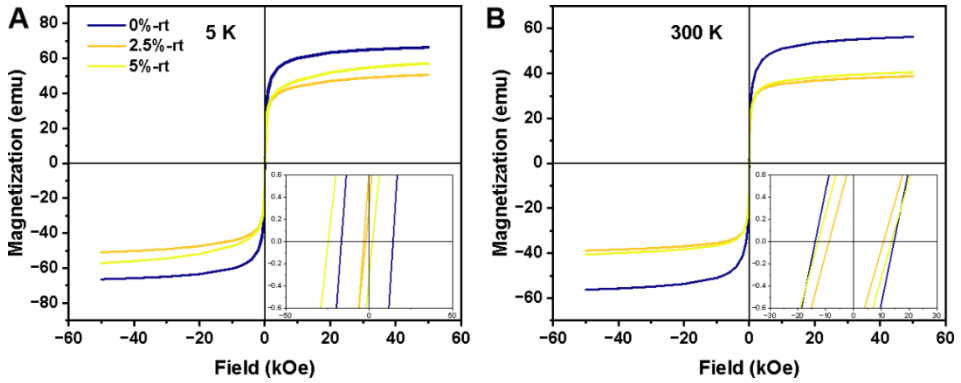

Figure 3.11. SQUID magnetometry performed with dry powders of Ho/Fe-oxide-rt NPs to obtain magnetizations (emu/g) and coercivities (H_c) in the insets): **(A)** $M(H)_T$ curves measured at 5 K (the inset represents 240× magnification of the y-axis); **(B)** $M(H)_T$ curves at 300 K; the inset represents 2400× magnification of the y-axis.

Table 3.4. Overview of the magnetic properties of x% Ho/Fe-oxide NPs: saturation magnetization (M_s) at 50 kOe, T = 5 K and 300 K, and coercivity (H_c) at T = 5 K and 300 K.

Ho/Fe-oxide NPs (%Ho)	Grain Size (nm)	Saturation Magnetization (Ms) (emu/g)		Coercivity (Hc) (Oe)	
		5 K	300 K	5 K	300 K
0[a]	9.3	62.0	54.1	51.7	11.5
2.5[a]	11.3	79.0	64.9	134.2	7.3
5[a]	16.6	71.1	55.2	83.2	9.0
0[b]	8.2	66.1	56.3	16.6	13.8
2.5[b]	11.1	50.7	38.7	3.2	8.8
5[b]	9.9	57.0	40.5	24.5	12.8

a Prepared with 1h heating at 60 °C; b Prepared at room temperature.

Conclusion

In summary, this study demonstrates that Ho-doping in Fe-oxide NPs exhibits a complex interplay with particle size, magnetic ordering, and hyperfine interactions. We showed that at the doping levels below 0.5% , the impact of Ho incorporation is negligible, with heating performance primarily governed by the particle size. The highest M_S values, and hence the best heating capacity, were achieved at 2.5% Ho-doping, and since the size of these NPs was similar to that of the undoped Fe-oxide NPs, it was confirmed that this enhancement arises directly from Ho-incorporation. At higher doping (5%), the effects of Ho-content and particle size become difficult to differentiate, while structural analysis indicates only partial substitution of Ho into the Fe-oxide

lattice. Detailed Mössbauer spectroscopy and XRD analysis further identified subtle changes in hyperfine fields and Fe-phases as the cause of magnetic anisotropy and its importance for tuning heating performance. Finally, a slight modification of the synthesis by performing the co-precipitation reaction at room temperature yielded NPs of the same size, which allowed to exclude this parameter from the factors contributing to the increase in M_S and showing that the Ho-doping level dominates the magnetic properties in magnetite. Future studies with the radioactive ^{166}Ho doped in Fe-oxide will demonstrate the potential of this hybrid NPs for combined hyperthermia and radiotherapy of tumors.

References

1. Liu, X.; Zhang, Y.; Wang, Y.; Zhu, W.; Li, G.; Ma, X.; Zhang, Y.; Chen, S.; Tiwari, S.; Shi, K.; Zhang, S.; Fan, H. M.; Zhao, Y. X.; Liang, X.-J., Comprehensive understanding of magnetic hyperthermia for improving antitumor therapeutic efficacy. *Theranostics* **2020,** *10* (8), 3793-3815.
2. Jones, E. L.; Oleson, J. R.; Prosnitz, L. R.; Samulski, T. V.; Vujaskovic, Z.; Yu, D.; Sanders, L. L.; Dewhirst, M. W., Randomized Trial of Hyperthermia and Radiation for Superficial Tumors. *J Clin Oncol***2005,** *23* (13), 3079-3085.
3. Ahmed, K.; Tabuchi, Y.; Kondo, T., Hyperthermia: an effective strategy to induce apoptosis in cancer cells. *Apoptosis* **2015,** *20* (11), 1411-1419.
4. Wang, B.; Hu, S.; Teng, Y.; Chen, J.; Wang, H.; Xu, Y.; Wang, K.; Xu, J.; Cheng, Y.; Gao, X., Current advance of nanotechnology in diagnosis and treatment for malignant tumors. *Sign TransducTarg Ther* **2024,** *9* (1), 200.
5. Gavilán, H.; Avugadda, S. K.; Fernández-Cabada, T.; Soni, N.; Cassani, M.; Mai, B. T.; Chantrell, R.; Pellegrino, T., Magnetic nanoparticles and clusters for magnetic hyperthermia: optimizing their heat performance and developing combinatorial therapies to tackle cancer. *Chem Soc Rev* **2021,** *50* (20), 11614-11667.
6. Debye, P. J. W., *Polar molecules*. Dover publications: 1929.
7. Kötitz, R.; Weitschies, W.; Trahms, L.; Semmler, W., Investigation of Brownian and Néel relaxation in magnetic fluids. *J Magnet Magn Mater* **1999,** *201* (1), 102-104.
8. Li, X.; Lovell, J. F.; Yoon, J.; Chen, X., Clinical development and potential of photothermal and photodynamic therapies for cancer. *Nat Rev Clin Oncol* **2020,** *17* (11), 657-674.
9. Knavel, E. M.; Brace, C. L., Tumor Ablation: Common Modalities and General Practices. *Techniques in Vascular and Interventional Radiology* **2013,** *16* (4), 192-200.
10. Włodarczyk, A.; Gorgoń, S.; Radoń, A.; Bajdak-Rusinek, K., Magnetite Nanoparticles in Magnetic Hyperthermia and Cancer Therapies: Challenges and Perspectives. *Nanomaterials* **2022,** *12* (11), 1807.
11. Chang, D.; Lim, M.; Goos, J. A. C. M.; Qiao, R.; Ng, Y. Y.; Mansfeld, F. M.; Jackson, M.; Davis, T. P.; Kavallaris, M., Biologically Targeted Magnetic Hyperthermia: Potential and Limitations. *Front Pharm* **2018,** *9*, 831.
12. Abreu, M. M.; Chocron, A. F.; Smadja, D. M., From cold to hot: mechanisms of hyperthermia in modulating tumor immunology for enhanced immunotherapy. *Front Immunol* **2025,** *16*, 1487296.
13. Maier, A.; Jia, Q.; Shukla, K.; Dugulan, A. I.; Hagedoorn, P.-L.; van Oossanen, R.; van Rhoon, G.; Denkova, A. G.; Djanashvili, K., Enhancing Magnetic Hyperthermia Efficiency in Pd/Fe-Oxide Hybrid Nanoparticles through Mn-Doping. *ACS App Nano Mater* **2024,** *7* (23), 27465-27475.
14. Maier, A.; Djanashvili, K.; Denkova, A. G.; van Rhoon, G. C.; Pignol, J.-P.; van Oossanen, R., Synthesis of Hybride Palladium(103)/Iron Oxide Nanoparticles for Thermobrachy Therapy. *European Patent Application No. 2029314* **2021**.
15. van Oossanen, R.; Godart, J.; Brown, J. M. C.; Maier, A.; Pignol, J.-P.; Denkova, A. G.; Djanashvili, K.; van Rhoon, G. C., Feasibility Study on the Radiation Dose by Radioactive

Magnetic Core-Shell Nanoparticles for Open-Source Brachytherapy. *Cancers* **2022,** *14* (22), 5497.

16. Rajenimbalkar, R. S.; Deshmukh, V. J.; Patankar, K. K.; Somvanshi, S. B., Effect of multivalent ion doping on magnetic, electrical, and dielectric properties of nickel ferrite nanoparticles. *SciRep* **2024,** *14* (1), 29547.
17. Sahayaraj, R.; Enoch, K.; Pati, S. S.; Somasundaram, A. A., Cobalt doped Fe3O4 nanoparticles with improved magnetic anisotropy and enhanced hyperthermic efficiency. *Ceramics International* **2025,** *51* (15), 20786-20797.
18. Upadhyay, R. V.; Gupta, A.; Sudakar, C.; Rao, K. V.; Parekh, K.; Desai, R.; Mehta, R. V., Effect of rare-earth Ho ion substitution on magnetic properties of Fe3O4 magnetic fluids. *J Appl Phys* **2006,** *99* (8), 08m906.
19. Norek, M.; Peters, J. A., MRI contrast agents based on dysprosium or holmium. *Prog. Nucl. Magn Reson Spectrosc* **2011,** *59* (1), 64-82.
20. Chakraborty, S.; Sharma, K. S.; Rajeswari, A.; Vimalnath, K. V.; Sarma, H. D.; Pandey, U.; Jagannath; Ningthoujam, R. S.; Vatsa, R. K.; Dash, A., Radiolanthanide-loaded agglomerated Fe3O4 nanoparticles for possible use in the treatment of arthritis: formulation, characterization and evaluation in rats. *J Mater Chem B* **2015,** *3* (27), 5455-5466.
21. Klaassen, N. J. M.; Arntz, M. J.; Gil Arranja, A.; Roosen, J.; Nijsen, J. F. W., The various therapeutic applications of the medical isotope holmium-166: a narrative review. *EJNMMI Radiopharmacy and Chemistry* **2019,** *4* (1), 19.
22. Vimalnath, K. V.; Chakraborty, S.; Rajeswari, A.; Sharma, K. S.; Sarma, H. D.; Ningthoujam, R. S.; Vatsa, R. K.; Dash, A. In *Formulation, Characterization and Bio-evaluation of Holmium-166 labeled Agglomerated Iron Oxide Nanoparticles for Treatment of Arthritis of Knee Joints*, International Symposium on Photonics Applications and Nanomaterials (ISPAN), Trivandrum, INDIA, 2017

Oct 28-30; Trivandrum, INDIA, 2015; pp 4329-4338.

23. Ba-Abbad, M. M.; Benamour, A.; Ewis, D.; Mohammad, A. W.; Mahmoudi, E., Synthesis of Fe3O4 Nanoparticles with Different Shapes Through a Co-Precipitation Method and Their Application. *JOM* **2022,** *74* (9), 3531-3539.
24. Gawęda, W.; Osial, M.; Żuk, M.; Pękała, M.; Bilewicz, A.; Krysinski, P., Lanthanide-Doped SPIONs Bioconjugation with Trastuzumab for Potential Multimodal Anticancer Activity and Magnetic Hyperthermia. *Nanomaterials* **2020,** *10* (2), 288.
25. Osial, M.; Rybicka, P.; Pekala, M.; Cichowicz, G.; Cyranski, M. K.; Krysinski, P., Easy Synthesis and Characterization of Holmium-Doped SPIONs. *Nanomaterials* **2018,** *8* (6), 430.
26. Cruz, I. F.; Freire, C.; Araújo, J. P.; Pereira, C.; Pereira, A. M., Chapter 3 - Multifunctional Ferrite Nanoparticles: From Current Trends Toward the Future. In *Magnetic Nanostructured Materials*, El-Gendy, A. A.; Barandiarán, J. M.; Hadimani, R. L., Eds. Elsevier: 2018; pp 59-116.
27. Fortin, J.-P.; Wilhelm, C.; Servais, J.; Ménager, C.; Bacri, J.-C.; Gazeau, F., Size-Sorted Anionic Iron Oxide Nanomagnets as Colloidal Mediators for Magnetic Hyperthermia. *J Am Chem Soc* **2007,** *129* (9), 2628-2635.
28. Mehdaoui, B.; Meffre, A.; Carrey, J.; Lachaize, S.; Lacroix, L.-M.; Gougeon, M.; Chaudret, B.; Respaud, M., Optimal Size of Nanoparticles for Magnetic Hyperthermia: A Combined Theoretical and Experimental Study. *Adv Func Mater* **2011,** *21* (23), 4573-4581.

29. Fu, R.; Yan, Y.; Roberts, C.; Liu, Z.; Chen, Y., The role of dipole interactions in hyperthermia heating colloidal clusters of densely-packed superparamagnetic nanoparticles. *Sci Rep* **2018,** *8* (1), 4704.

30. Newkirk, L. R.; Tsuei, C. C., M\"ossbauer Study of Hyperfine Magnetic Interactions in Fe-Ga Solid Solutions. *Phys Rev B* **1971,** *4* (11), 4046-4053.

31. Siddique, M.; Ahmed, E.; Butt, N. M., Particle size effect on Mössbauer parameters in γ-Fe2O3 nanoparticles. *Physica B: Condensed Matter* **2010,** *405* (18), 3964-3967.

32. He, K.; Chen, N.; Wang, C.; Wei, L.; Chen, J., Method for Determining Crystal Grain Size by X-Ray Diffraction. *Cryst Res Technol* **2018,** *53* (2), 1700157.

4

In Vitro Investigation of the Synergistic effects of Magnetic Hyperthermia and Radiotherapy Enabled with ^{166}Ho:Ho/Fe-Oxide Nanoparticles

Introduction

Radiotherapy (RT) is an essential modality in modern oncology, alongside with surgery and systemic treatments such as chemo- and immune-therapy. It uses ionizing radiation to cause DNA damage, leading to cell death or the prevention of cell division.[1, 2] This rapidly developing therapeutic modality can be broadly divided into an external therapy, which uses external beams to deliver radiation to the localized tumors (EBRT), and internal radiotherapy, where radioactive sources are placed inside or near the tumor. The latter can be further classified into targeted radionuclide therapy (TRT), which involves the systemic administration of radionuclides coupled with tumor-specific targeting vectors suitable for metastases treatment, and brachytherapy (BT),[3] in which sealed radioactive sources are placed close to or within the tumor.[24]Therefore, BT can minimize unnecessary radiation exposure to healthy tissues and organs.[4] Today, BT has become a standard of care, used either as a single modality or as a boost after EBRT for tumors that benefit from highly localized radiation doses, as well as in postoperative settings where additional local control is needed, especially when the risk of local recurrence is high.[5] Moreover, combining BT with other treatments, such as chemotherapy,[5, 6] or hyperthermia (HT) offers the possibility of enhancing the overall therapeutic effect by increasing radiosensitivity and improving oxygenation[7-11] within the tumor microenvironment.[6]

Advances in nanotechnology have given impulse to the development of a new form of BT, which involves the use of nanoparticles (NPs) as miniature radiation sources, known as nano-brachytherapy (nano-BT). The advantage of nano-BT stems from the properties of nanomaterials, such as their large surface area, which allows for conjugation with various functional molecules, e.g., targeting vectors, imaging reporters, and chemotherapeutic drugs, as well as the incorporation of radionuclides. By selecting appropriate radioisotopes and nanocarriers, nano-BT systems can be assembled and delivered to the patient via intratumoral injection as an alternative to conventional BT (Figure 4.1). Furthermore, the potential of NPs to penetrate the tumor microenvironment more uniformly compared to conventional BT-sources, may provide improved dose distribution while minimizing radiation exposure to surrounding healthy tissues.[4, 12]

Various radioisotopes with specific properties in terms of half-life and energy can be used for BT.[3] For therapeutic purposes, the preferred half-lives of radionuclides are above 6 h to ensure practical handling and logistics.[13 14] β^--emitting radionuclides are interesting in this respect, as they often exhibit favorable combination of suitable half-lives and relatively long penetration ranges of electrons in tissue (≈0.05 - 12 mm), which is particularly important for treatment of large or bulky tumors.[4] One such radionuclide is holmium-166 (^{166}Ho), which can be produced via thermal neutron irradiation of the monoisotopic ^{165}Ho (100% natural abundance; $\sigma_{n,\gamma} \approx 59$ barns) (Scheme 1). As a β^--emitter with a half-life of 26.8 h, ^{166}Ho is a promising candidate for various applications in nuclear medicine and BT. Next to high-energy therapeutic β-particles (1.8 MeV with average soft tissue penetration of 3.2 mm), ^{166}Ho also emits γ-rays of 80.57 keV that can be used for single photon emission tomography (SPECT) imaging. Moreover, Ho possesses

one of the highest magnetic moments of all elements (μ = 10.6 μB), giving it unique paramagnetic properties that enable the use of Ho as a contrast agent in magnetic resonance imaging (MRI) as well as a dopant in magnetic nanoparticles (MNPs) for magnetic hyperthermia (MHT).[15-18] The latter two applications are in fact dominated by superparamagnetic iron oxide nanoparticles (Fe-oxide NPs),[19] whose exposure to an alternating magnetic field (AMF) generates heat through Néel and Brownian relaxation processes.[20] Fe-oxide NPs have attracted considerable attention due to their superior magnetic properties in combination with good biocompatibility, low toxicity, and relatively simple manufacturing. This includes facile surface functionalization and radiolabeling, the latter being especially important for the intended application in nano-BT.

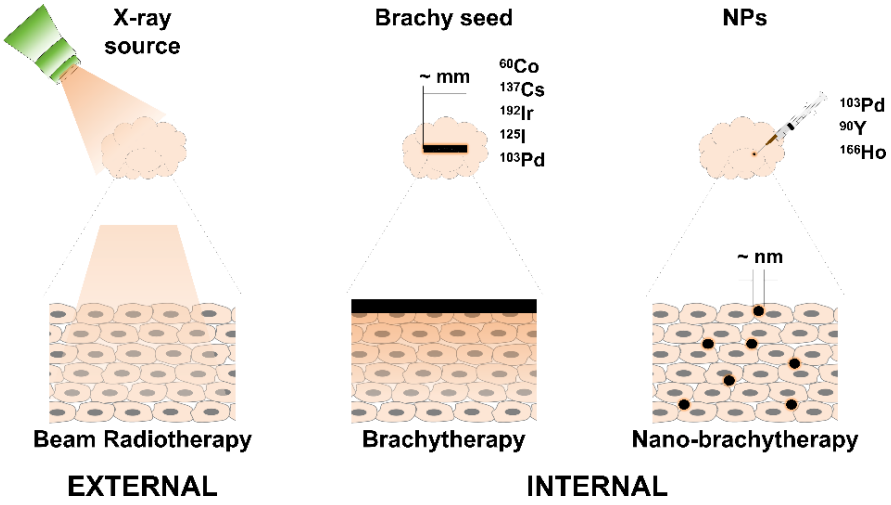

Figure 4.1. Schematic representation of different radiotherapeutic approaches for the treatment of localized tumors.

The preparation and characterization of Fe-oxide NPs doped with ^{165}Ho was studied in Chapter 3. Ho-doping of 2.5% was found to be the most optimal to enhance the magnetic properties, and thus, to improve the heating capacity of MNPs. However, their *in vitro* MHT performance had yet to be demonstrated. Furthermore, by easily replacing ^{165}Ho with ^{166}Ho, the combination of MHT with RT could be realized to demonstrate the synergistic effects of both therapeutic modalities. This chapter represents a systematic evaluation of the effect of Ho/Fe-oxide NPs and their radioactive analogues ^{166}Ho:Ho/Fe-oxide NPs on two cancer cell lines (U87 and U2OS) with and without application of AMF.

Materials and methods

Materials and methods

Iron (II) chloride tetrahydrate ($FeCl_2 \cdot 4H_2O$), iron (III) chloride hexahydrate ($FeCl_3 \cdot 6H_2O$), 25% ammonia, sodium hydroxide (NaOH), polyvinylpyrrolidone (PVP) and ethanol were purchased from Sigma Aldrich, holmium chloride hexahydrate ($HoCl_3 \cdot 6H_2O$) was purchased from Strem. All chemicals were used without further purification.

$HoCl_3 \cdot 6H_2O$ irradiation

The $^{166}HoCl_3 \cdot 6H_2O$ was prepared through neutron irradiation of $HoCl_3 \cdot 6H_2O$ (Scheme 4.1) at the BP2/BP3 pneumatic irradiation facility of Hoger Onderwijs Reactor (HOR) of the TU Delft | Reactor Institute. Typically, 5 mg of $HoCl_3 \cdot 6H_2O$ were sealed in a polyethylene capsule and irradiated for 1-5 h. The neutron fluxes in the facilities were: $\Phi_{th} = 3.64 \times 10^{16}$ s^{-1} m^{-2}, $\Phi_{epi} = 7.14 \times 10^{14}$ s^{-1} m^{-2}, and $\Phi_{fast} = 2.59 \times 10^{15}$ s^{-1} m^{-2} for BP2; $\Phi_{th} = 4.6 \times 10^{16}$ s^{-1} m^{-2}, $\Phi_{epi} = 8.28 \times 10^{14}$ s^{-1} m^{-2}, and $\Phi_{fast} = 3.25 \times 10^{15}$ s^{-1} m^{-2} for BP3. After irradiation, the samples were cooled for 16-65 h (depending on the irradiation facility used and irradiation time) to ensure the decay of short-lived activation products and achieve a final activity of ~50 MBq. The obtained $^{166}HoCl_3 \cdot 6H_2O$ samples in capsules were then transferred into a glass vial containing 2 mL of milli-Q.

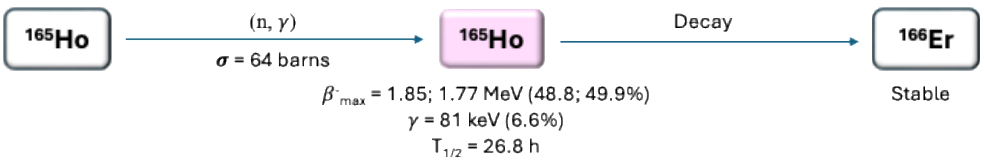

Scheme 4.1. Diagram for the production route of ^{166}Ho through neutron activation of ^{165}Ho.

Synthesis of ^{166}Ho-doped iron oxide nanoparticles (^{166}Ho:Ho/Fe-oxide NPs)

Ho/Fe-oxide NPs were prepared based on the method described in Chapter 3. In a typical procedure, $FeCl_2 \cdot 4H_2O$ (49.7 mg, 0.25 mmol) and PVP (62.5 mg) were dispersed in 10 mL water under ultrasonication for 15 min. Then, $FeCl_3 \cdot 6H_2O$ (131.82 mg, 0.4875 mmol) and 1.896 mL of $HoCl_3$ solution (2.5 mg mL^{-1}) were added into the mixture. After heating to 60 °C under 700 rpm stirring, 0.313 mL ammonia was added into the mixture drop wise. The reaction mixture was kept as such for 60 min. The Ho/Fe-oxide NPs were collected with a magnet, washed with water and culture medium several times and dispersed in culture medium (5 mg mL^{-1}) for further use. For the synthesis of ^{166}Ho:Ho/Fe-oxide NPs, the 2.5 mg mL^{-1} $HoCl_3$ solution were replaced by $^{166}HoCl_3$ solution, and the activity was corrected with instrumental neutron activation analysis (INAA) after the synthesis.

In vitro experiments

Cell culture

Human glioblastoma astrocytoma cell line (U87) and human osteosarcoma cell line (U2OS) were provided by ATCC and Erasmus MC, respectively. Cells were grown in DMEM (Dulbecco's modified Eagle's medium, Avantor Biowest) supplemented with 10% of FEB (fetal bovine serum) and 1% penicillin-streptomycin (Avantor Biowest) at 37 ºC with 5% CO_2.

Cell studies

Cell viability was measured using a modified Cell Counting Kit-8 (CCK-8) protocol. U87/U2OS cells (5×10^4 mL^{-1}, 90 µL well^{-1}) were seeded into a 96-well plate and incubated at 37 ºC with 5% CO_2 for 24 h to allow cell attachment. Then, 10 µL of Ho/Fe-oxide NPs suspension was added to each well (0, 1, 2, 3, 4, 5 mg mL^{-1}) and the cells were incubated for 24 and 48 h. At the end of each incubation period, 10 µL CCK-8 solution was added to each well, followed by a further 4h incubation. Subsequently, 50 µL of PBS (phosphate-buffered saline) was added to each well. The NPs were held in place at the bottom of the wells using a magnet, while 100 µL of the liquid was transferred to a new plate, and 10 µL of 1% HCl was added to each well. The absorbance of each well was measured at 450 nm using a microplate reader, with background subtraction applied.

Treatment Experiments

For the MHT and RT treatments, both cell types were seeded in 35 mm cell culture dishes containing 2 mL of culture medium at concentrations of 1×10^5 and 5×10^4 cell mL^{-1}, respectively. The cells were then incubated for 24 h at 37 ºC with 5% CO_2 to allow attachment.

MHT experiment

Heating experiments were performed with the MagneTherm Digital device (NanoTherics) by placing the culture dishes in the 50 mm coil with 20 °C cooling at the operating frequency of 338 kHz and the field strength of 18 mT. 1 mL suspension of Ho/Fe-oxide NPs with different concentrations (0, 1, 2, 3, 4, 5 mg mL^{-1}) was added to each dish. Two groups of cells were denoted as AMF(+) and AMF(-), corresponding to the cells subjected to an alternating magnetic field and those that were not (control), respectively. After 15 min, the liquid in each dish was aspirated and the cells were washed with PBS three times to remove all NPs and treated with Trypsin for 5 min. After this, the suspensions of cells from each group were transferred into a 96-well plate (100 µL well^{-1}) and seeded cells were incubated at 37 ºC with 5% CO_2 for 72 h. Then, CCK-8 (10 µL well^{-1}) was added to each well and incubated for another 4 h. The absorbance at 450 nm (OD_{450}) of each well was measured using a microplate reader with background subtraction. The viability of each group was calculated based on the following equation (Eq 1).

Viability (%) = Average $OD_{450(\text{sample})}$/Average $OD_{450(\text{blank})}$ × 100% (1)

MHT-RT experiment

1 mL suspension of ^{166}Ho:Ho/Fe-oxide NPs with the activity varied from 0 to 2 MBq were added to the dishes with U87 (2 mg mL^{-1}) and U2OS cells (2.5 mg mL^{-1}). After 15 min, the NPs were removed by washing with PBS three times and cells in each dish were treated with Trypsin for 5 min. The cells were then seeded into a 96-well plate (100 µL well^{-1}) and incubated for 5 days. 10 µL CCK-8 was added to each well and their absorbance at 450 nm were measured using a microplate reader after 1 h incubation. The viability of each group was calculated using Eq. 1. The IC_{50} values were calculated using sigmoidal dose–response curve in Origin 2024.

Results and Discussion

The effect of ^{166}Ho:Ho/Fe-oxide NPs designed for nano-brachytherapy combined with hyperthermia was investigated on two human tumor cell lines: U87 and U2OS. U87 is a brain tumor (glioblastoma) cell line that adopts an epithelial-like, adherent morphology when cultured *in vitro*, which is generally convenient for the studies.[21] Moreover, U87 is known to exhibit both high radioresistance and high heat tolerance due to strong DNA repair/antioxidant mechanisms and overexpression of heat shock proteins (HSPs), respectively.[22] On the contrary, U2OS, a bone tumor (osteosarcoma) cell line of mesenchymal origin, is less efficient in DNA repair and expresses less HSPs.[23] Consequently, using these distinct cell lines allows to test the effect of ^{166}Ho:Ho/Fe-oxide NPs in both resistant and sensitive tumor cell types and to make an initial comparison of cell-specific differences that may influence the therapeutic outcome.

Cytotoxicity of Ho/Fe-oxide NPs in U87 and U2OS cells

Assessment of the cellular safety of the nanomaterials designed for therapeutic applications is the first step to ensure that engineered formulations will not induce undesired adverse effects.[24] Therefore, before testing the *in vitro* therapeutic efficiency, the cytotoxicity of Ho/Fe-oxide NPs was investigated on both U2OS and U87 cells. For this, cells were incubated with increasing concentrations of Ho/Fe-oxide NPs (0 - 5 mg mL^{-1}) for 24 and 48 h. As shown in Figure 4.2, the viability in both cells after 24h of incubation remained >90%, even at the highest concentration of 5 mg mL^{-1}, while increasing the incubation time to 48h resulted in a notable decrease by 20% in both cell types for the NPs concentrations >3 mg mL^{-1}. These results indicate the subtoxic concentrations Ho/Fe-oxide NPs, suggesting that they could be used as a safe range to continue investigations of their therapeutic efficacy.

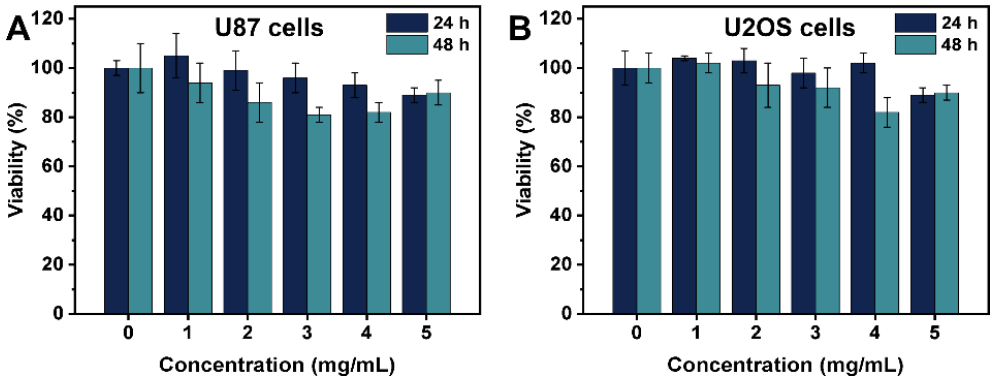

Figure 4.2. Viability of (**A**) U87 and (**B**) U2OS cells (n = 5) incubated with various concentrations of Ho/Fe-oxide NPs for 24 and 48 h.

In vitro MHT with Ho/Fe-oxide NPs

Since temperatures generated by MNPs in an AMF are proportional to the amount of magnetic material, increasing concentrations of Ho/Fe-oxide NPs (0 - 5 mg mL^{-1}) were applied and cell viability with (15 min) and without AMF exposure was studied to verify the efficacy of MHT on the cells. No clear decreases in viability were observed for the AMF(-) groups of both cell lines up to the highest concentration (5 mg mL^{-1}) of NPs added (Figure 4.3). A noticeable decrease in viability by ±22% was detected for U87 cells exposed to AMF when the concentration of 2 mg mL^{-1} of NPs was applied (Figure 4.3A), which aligns with the lowest concentration required to produce heat sufficient for MHT, as defined in Chapter 3. A further increase in the NPs concentration to 3 mg mL^{-1} reduced cell viability to 15% and viability remained at this level at higher concentrations. A comparable response to MHT was observed for U2OS cells, although the concentration required to trigger a decline in viability was higher, i.e. 3 mg mL^{-1}.

Demonstrating the hyperthermic effects of Ho/Fe-oxide NPs to both cell lines, allowed for considerations on balance between efficacy and safety and identification of concentrations that caused measurable cell damage, while still leaving room for the detection of synergistic effects from RT. Taking into account that lower NPs concentrations are generally favored in nanomedicine to minimize adverse effects in the human body, such as retention, metabolism, and possibly long-term toxicity, two NPs concentrations 2 and 2.5 mg mL^{-1} were selected for U87 and U2OS, respectively, as the optimal concentrations for the combined MHT-RT treatment.

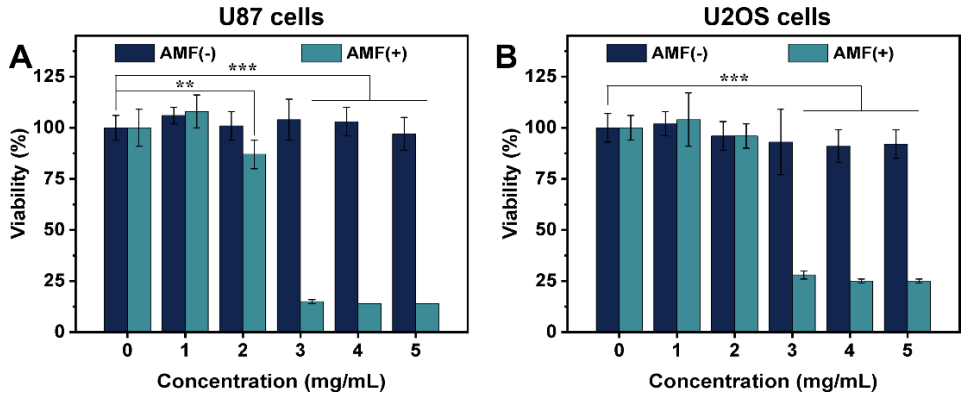

Figure 4.3. MHT effect of Ho/Fe-oxide NPs tested on U87 (**A**) and U2OS (**B**) cells (n = 5) at various concentrations with (+) and without (-) AMF for 15 min. ** $p < 0.01$, *** $P < 0.001$.

^{166}Ho:Ho/Fe-oxide NPs for in vitro synergistic MHT-RT

The ^{166}Ho:Ho/Fe-oxide NPs used in the investigations of efficiency of synergistic magnetic hyperthermia-radiotherapy (MHT-RT), were prepared following the procedure described in Chapter 3. The synthesis could be conveniently adapted for the radioactive analogues by replacing $HoCl_3$ with $^{166}HoCl_3$. Thereby, the desired activities from 0 to 2 MBq were achieved by mixing the radioactive and non-radioactive NPs at different ratios in the cell media, while maintaining the concentrations of 2 and 2.5 mg mL^{-1}, which proved to be sufficient to perform MHT on U87 and U2OS cells, respectively.

As mentioned above, U87 cells are known to be radioresistant, and therefore, were expected to display compensatory growth as a defensive response to cellular stress during the first few days after radiation exposure. Therefore, to accurately assess the therapeutic effect of ^{166}Ho:Ho/Fe-oxide NPs, it was necessary to allow sufficient time for these initial adaptive responses to occur. Consequently, evaluation of the therapeutic outcome was performed 5 days later, ensuring that the observed effects reflected the true impact of the treatment rather than a transient condition.

When evaluating the exclusive effect of RT on U87 cells in the absence of AMF, a viability above 75% was measured even at 2 MBq, which is the lowest activity applied for effective RT across all experimental groups. As can be seen in Figure 4.4A, a much lower activity (0.6 MBq) was necessary to achieve a similar decrease in viability when using AMF, while a further increase in activity allowed for a decrease to ±45% at 2 MBq. In the case of U2OS cells, the viability remained above 85% for the AFM(-) group and decreased to 75% with 2 MBq (Figure 4.4B). After introducing MHT by turning on AMF, a viability of less than 25% could be achieved already at 0.6 MBq. Although the effective NPs concentrations and radiation doses for U87 and U2OS cells were different, the trend of lower viabilities in all AMF(+) groups suggests the synergistic therapeutic effect of MHT-RT.

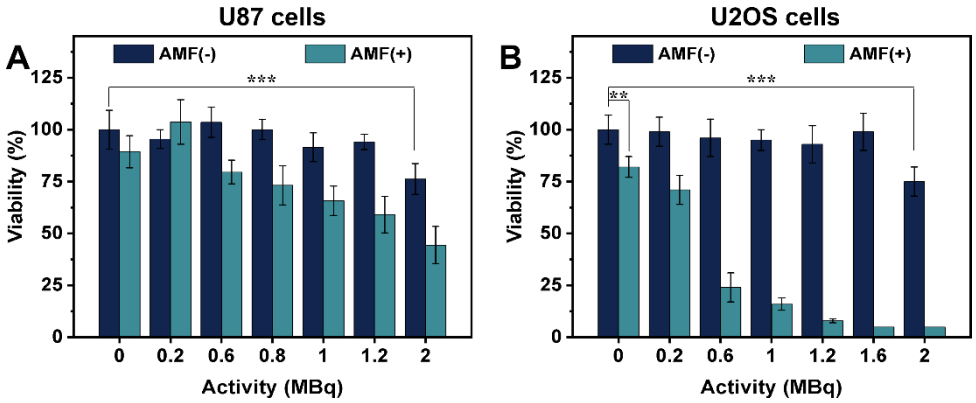

Figure 4.4. Synergistic MHT-RT performance of ^{166}Ho/Fe-oxide NPs on U87 (**A**) and U2OS (**B**) cells (n = 5) at various activities with/without AMF. Concentration of NPs is 2 mg mL^{-1} (U87) and 2.5 mg mL^{-1} (U2OS). ** p < 0.01, *** P < 0.001.

To further illustrate the potential for exploiting the synergistic effects of MHT and RT to reduce both the concentration and activity of NPs, the 50% inhibitory concentrations (IC_{50}) were calculated for U87 and U2OS cells using the viability data from the MHT, RT and MHT+RT experiments (Figure 4.5). Although the number of datapoints was insufficient for highly robust curve fitting, the resulting plots and IC50 and the obtained effective parameters (Table 4.1) depict the overall tendency of the NPs effect on cell viability, rather than providing definitive quantitative values.

The results clearly show that U87 cells require a lower concentration of NPs to reach 50% cell death, whereas U2OS cells need higher activity to achieve the same effect. Regardless of the expected differences in heat and radiation resistance, both cell lines showed substantial reduction in the radiation dose required to reach 50% viability, decreasing from >2MBq to 1.6 in U87 cells and to 0.3 MBq in U2OS cells when treated with 2 and 2.5 mg mL^{-1}, respectively. Since in this study the NPs concentrations were not varied while keeping the activity fixed, the effect of further reduction of the NPs concentration was not assessed. However, the observed trend in the combined treatment supports the possibility of achieving the same therapeutic effect at even lower NPs concentrations.

Table 4.1. Effective parameters[a] and outcomes determined for the individual and synergistic treatments.

	MHT	RT	MHT+RT	
	C (mg mL^{-1})	A (MBq)	C (mg mL^{-1})	A (MBq)
U87	2.18	>2	2	1.6
U2OS	2.63	>2	2.5	0.3

[a] C = concentration, V = viability, A = activity.

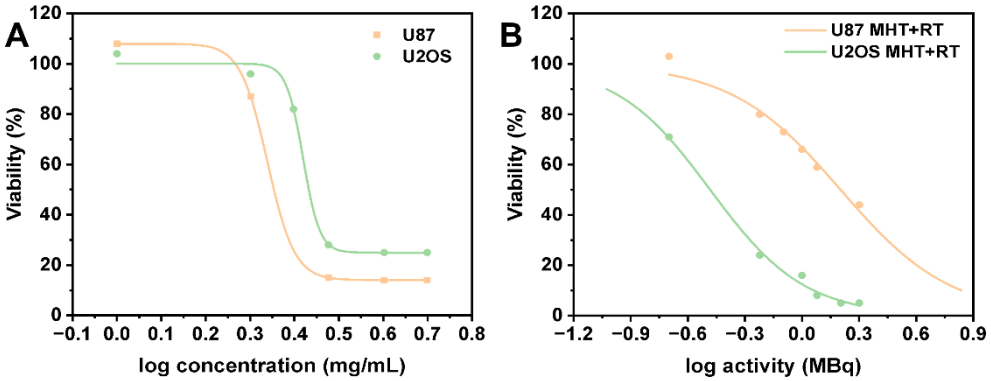

Figure 4.5. 50% inhibitory concentrations (IC_{50}) of U87 and U2OS cells for (A) MHT and (B) MHT+RT. Line correspond to the fitted sigmoidal dose–response curve.

Conclusions

The possibility of using ^{166}Ho/Fe-oxide NPs for cancer treatment combining radioactivity and magnetic hyperthermia was studied on U87 and U2OS cell lines. The individual therapeutic effects of both treatment modalities were compared by observing the viability of the cells incubated with nanoparticles with or without the application of AMF and ^{166}Ho to study the impact of MHT and RT, respectively. Finally, the combined treatment was applied, and the results demonstrated a clear synergistic character of this approach. Compared to MHT and RT alone, the effective concentration of NPs could be reduced to 2 mg mL^{-1}, and the radioactivity of NPs to 1.6 MBq for U87 cells when performing synergistic MHT-RT. Similar results were observed on U2OS cells, where the concentration of NPs was reduced to 2.5 mg mL^{-1}, and the radioactivity to 0.3 MBq. These results suggest that the combined treatment may allow the use of reduced NPs concentrations while maintaining comparable cytotoxicity. However, the combination of these parameters needs further optimization, and additional experiments are required to validate their effects. Finally, sequential subjection of cells to MT and RT treatments will help elucidating the true contribution of each therapeutic modality to the designed combined treatment.

References

1. Zafar, A.; Khatoon, S.; Khan, M. J.; Abu, J.; Naeem, A., Advancements and limitations in traditional anti-cancer therapies: a comprehensive review of surgery, chemotherapy, radiation therapy, and hormonal therapy. *Discov Oncol* **2025,** *16* (1), 607.
2. Citrin, D. E., Recent Developments in Radiotherapy. *New Engl J Med* **2017,** *377* (11), 1065-1075.
3. Chargari, C.; Deutsch, E.; Blanchard, P.; Gouy, S.; Martelli, H.; Guérin, F.; Dumas, I.; Bossi, A.; Morice, P.; Viswanathan, A. N.; Haie-Meder, C., Brachytherapy: An overview for clinicians. *CA: A Cancer J Clin* **2019,** *69* (5), 386-401.
4. Seniwal, B.; Thipe, V. C.; Singh, S.; Fonseca, T. C. F.; Freitas de Freitas, L., Recent Advances in Brachytherapy Using Radioactive Nanoparticles: An Alternative to Seed-Based Brachytherapy. *Front Oncol* **2021,** *11*, 766407.
5. Miszczyk, M.; Magrowski, Ł.; Krzysztofiak, T.; Stando, R.; Majewski, W.; Stawiski, K.; Masri, O.; Ciepał, J.; Depowska, G.; Chimiak, K.; Bylica, G.; Czapla, B.; Masri, M.; Cichur, F.; Jabłońska, I.; Gmerek, M.; Nowicka, Z.; Wojcieszek, P.; Sadowski, J.; Suwiński, R.; Rajwa, P.; Goldner, G.; Moll, M., Brachytherapy boost improves survival and decreases risk of developing distant metastases compared to external beam radiotherapy alone in intermediate and high risk group prostate cancer patients. *Radiother Oncol* **2023,** *183*, 109632.
6. Skowronek, J., Current status of brachytherapy in cancer treatment – short overview. *J Contemp Brachyther* **2017,** *9* (6), 581-589.
7. Albadari, N.; Deng, S.; Li, W., The transcriptional factors HIF-1 and HIF-2 and their novel inhibitors in cancer therapy. *Exp Opin Drug Discov* **2019,** *14* (7), 667-682.
8. Barker, H. E.; Paget, J. T. E.; Khan, A. A.; Harrington, K. J., The tumour microenvironment after radiotherapy: mechanisms of resistance and recurrence. *Nat Rev Cancer* **2015,** *15* (7), 409-425.
9. Jarosz-Biej, M.; Smolarczyk, R.; Cichon, T.; Kulach, N., Tumor Microenvironment as A "Game Changer" in Cancer Radiotherapy. *Int J Mol Sci***2019,** *20* (13), 3212.
10. Nagao, A.; Kobayashi, M.; Koyasu, S.; Chow, C. C. T.; Harada, H., HIF-1-Dependent Reprogramming of Glucose Metabolic Pathway of Cancer Cells and Its Therapeutic Significance. *Int J Mol Sci* **2019,** *20* (2), 238.
11. Song, C. W.; Kim, H.; Kim, M.-S.; Park, H. J.; Paek, S.-H.; Terezakis, S.; Cho, L. C., Role of HIF-1α in the Responses of Tumors to Radiotherapy and Chemotherapy. *Cancer Res Treat* **2025,** *57* (1), 1-10.
12. Stankovic, A.; Mihailovic, J.; Mirkovic, M.; Radovic, M.; Milanovic, Z.; Ognjanovic, M.; Jankovic, D.; Antic, B.; Mijovic, M.; Vranjes-Duric, S.; Prijovic, Z., Aminosilanized flower-structured superparamagnetic iron oxide nanoparticles coupled to 131I-labeled CC49 antibody for combined radionuclide and hyperthermia therapy of cancer. *Int J Pharmaceut* **2020,** *587*, 119628.
13. Yeong, C.-H.; Cheng, M.-h.; Ng, K.-H., Therapeutic radionuclides in nuclear medicine: current and future prospects. *J Zhejiang Uni SCI B* **2014,** *15* (10), 845-863.
14. Stokke, C.; Kvassheim, M.; Blakkisrud, J., Radionuclides for Targeted Therapy: Physical Properties. *Molecules* **2022,** *27* (17), 5429.

15. Gossuin, Y.; Gillis, P.; Hocq, A.; Vuong, Q. L.; Roch, A., Magnetic resonance relaxation properties of superparamagnetic particles. *WIREs Nanomed Nanobiotech* **2009,** *1* (3), 299-310.

16. Hervault, A.; Thanh, N. T. K., Magnetic nanoparticle-based therapeutic agents for thermo-chemotherapy treatment of cancer. *Nanoscale* **2014,** *6* (20), 11553-11573.

17. Liu, D.; Yang, W.; Zhang, B., Magnetic Resonance Imaging and Its Molecular Probes in Evaluating the Response to Tumor Treatment. *Nano Biomed Eng* **2024,** *17* (1), 36-55.

18. Pearce, J.; Giustini, A.; Stigliano, R.; Jack Hoopes, P., Magnetic Heating of Nanoparticles: The Importance of Particle Clustering to Achieve Therapeutic Temperatures. *J Nanotech Eng Med* **2013,** *4* (1), 011005-1.

19. Ghazi, R.; Ibrahim, T. K.; Nasir, J. A.; Gai, S.; Ali, G.; Boukhris, I.; Rehman, Z., Iron oxide based magnetic nanoparticles for hyperthermia, MRI and drug delivery applications: a review. *RSC Adv* **2025,** *15* (15), 11587-11616.

20. Laurent, S.; Dutz, S.; Häfeli, U. O.; Mahmoudi, M., Magnetic fluid hyperthermia: focus on superparamagnetic iron oxide nanoparticles. *Adv Coll Interf Sci* **2011,** *166* (1-2), 8-23.

21. Persano, S.; Vicini, F.; Poggi, A.; Fernandez, J. L. C.; Rizzo, G. M. R.; Gavilán, H.; Silvestri, N.; Pellegrino, T., Elucidating the Innate Immunological Effects of Mild Magnetic Hyperthermia on U87 Human Glioblastoma Cells: An In Vitro Study. *Pharmaceutics* **2021,** *13* (10), 1668.

22. Hermisson, M.; Strik, H.; Rieger, J.; Dichgans, J.; Meyermann, R.; Weller, M., Expression and functional activity of heat shock proteins in human glioblastoma multiforme. *Neurology* **2000,** *54* (6), 1357-1365.

23. Hou, C.-H.; Lin, F.-L.; Hou, S.-M.; Liu, J.-F., Hyperthermia Induces Apoptosis through Endoplasmic Reticulum and Reactive Oxygen Species in Human Osteosarcoma Cells. *International J Mol Sci* **2014,** *15* (10), 17380-17395.

24. Rosa, V.; Silikas, N.; Yu, B.; Dubey, N.; Sriram, G.; Zinelis, S.; Lima, A. F.; Bottino, M. C.; Ferreira, J. N.; Schmalz, G.; Watts, D. C., Guidance on the assessment of biocompatibility of biomaterials: Fundamentals and testing considerations. *Dental Mater* **2024,** *40* (11), 1773-1785.

5

Towards Selective Magnetic Hyperthermia of Tumors via pH-responsive Heating Modulated by ZIF-coated Fe-oxide NPs

Introduction

With cancer remaining a major threat to human health, recent technological advances are driving modern oncology research towards the development of high-precision tumor treatment strategies. Selective targeting of malignant tissues while sparing surrounding healthy structures represents a key challenge in these approaches. Although traditional cancer treatments such as radiation therapy, chemotherapy and surgery still constitute the current standard clinical practice, the emergence of nanotechnology plays a key role in enabling tumor-specific drug delivery at the cellular and molecular level. This, however, does not completely eliminate the problem of toxicity and invasiveness, so the search for new methodologies continues.[1]

Magnetic hyperthermia therapy (MHT) represents an alternative method to treat cancer using magnetic nanoparticles (MNPs) that can generate heat to kill tumor cells (>46 ºC) or to sensitize them to other treatments (42 -46 ºC).[2, 3] The method relies on delivering MNPs to the tumor and exposing them to an alternating magnetic field (AMF), which affects their magnetic moments, resulting in energy dissipation[4, 5] through i) Néel relaxation –flipping of the magnetic dipole within the MNPs, ii) Brownian relaxation – physical rotation of the MNPs, and iii) hysteresis loss.[6, 7] For superparamagnetic nanoparticles (NPs) such as iron oxide (Fe_3O_4, Fe_2O_3), hysteresis loss may be negligible or even non-existent, and the heat is generated primarily by Néel or Brownian relaxation.[6, 8]

Most MHT studies in the literature focus on improving the specific loss power (SLP), a parameter that defines the heat capacity of MNPs and is strongly influenced by their morphology and physical properties.[9] With rational design and appropriate adjustments of particle size, shape, composition, and magnetic anisotropy, the SLP of MNPs can be significantly increased.[8, 10, 11] MNPs smaller than 20 nm typically exist as single magnetic domains, characterized by a uniform magnetization,[12] where heat generated under AFM is primarily governed by Néel relaxation. In this process, the magnetic moments align with the rapidly oscillating field, and the magnetic response leads to energy dissipation as heat. As particle size increases above 20 nm, Brownian relaxation starts to take over, provided that the MNPs can freely rotate. For MNPs beyond the single-domain size limit, heat dissipation becomes dominated by hysteresis losses rather than relaxation mechanisms.[12] Therefore, the optimal MNP size for effective MHT typically ranges from 10 to 50 nm, depending on their morphology and composition.[10] From this point of view, doping with magnetic elements is an interesting way to enhance SLP by modifying the MNPs' magnetic anisotropy.[11]

Although the effectiveness of MHT can be significantly improved by the abovementioned modifications, the non-selective nature of the AMF remains a major limitation. Unlike photothermal therapy which uses a laser to heat specific area, it is virtually impossible to apply AMF solely to the tumor region.[13] Intratumoral administration of MNPs may offer a partial solution to this problem, but at the same time poses challenges, such as precise injection and excessively high local concentrations, both of which lead to the heating effect extending to

surrounding tissue.[14] Therefore, ensuring the efficacy of MNPs restricted to tumor sites is essential to avoid unintended thermal effects in healthy tissues.

Another way to alter the thermal properties of MNPs is to modulate their state of aggregation.[8, 15] Small single-domain iron oxide nanoparticles (Fe-oxide NPs) can, under certain conditions, form long chains, in which magnetic moments tend to align collectively under applied magnetic field leading to an increase in magnetization, and thus, to the generation of heat.[16] On the other hand, if MNPs aggregate randomly, they enter multiple magnetic domain regime, which reduces the overall magnetization.[17] Therefore, modulation of the aggregation state of the applied MNPs is an attractive tool for creating differentiated heating effects in response to biological conditions.

The abnormal tumor cell growth often results in irregular features in the surrounding tumor microenvironment (TME).[18] The typical characteristics include hypoxia, elevated concentrations of certain enzymes and endogenous H_2O_2 (50 - 100 μM), overexpression of glutathione (GSH, ~10 mM), and local acidity (pH = 5.5 - 6.5).[19-23] Due to these specific properties, TME has been extensively investigated as a target for improving therapeutic selectivity. Examples include the use of the high levels of endogenous H_2S in colorectal cancer as a target for in situ synthesis of photothermal agents[24, 25] or H_2O_2 as a target to generate ·OH for chemodynamic therapy based on Fenton/Fenton-like reaction.[26]

In this work, we exploit the pH differences between tumor and normal tissues to engineer nanosystems with pH-responsive hyperthermic behavior. Zeolite imidazole framework-8 (ZIF-8) is a biologically safe nanomaterial, known for its facile preparation and pH-sensitive properties.[27] Furthermore, its large specific surface area and good stability render it an attractive nanocarrier compared to other NPs.[27, 28] Most importantly, ZIF-8 can degrade at lower pH, allowing for selective delivery of therapeutic and/or imaging agents.[29-32] Ghosh *et al*. reported UCNP@MOF-DOX/TCZnPc nanocomposite to deliver doxorubicin and upconversion NPs to tumor for both chemo- and photodynamic therapy.[33] While in most of these studies ZIF-structures are used for pH-responsive drug delivery, their well-defined crystal structure can be utilized not only as a carrier, but also as a tool to promote the aggregation of MNPs.

Based on this strategy, ZIF-8 was used to aggregate Fe-oxide NPs to form Fe-ZIF nanocomposites (NCs), where the effective number of incorporated Fe-oxide NPs and the size of the NCs were controlled by synthetic parameters such as applied concentrations and temperature. This aggregation resulted in a decrease in the collective magnetization, and consequently, in a reduced heating properties at physiological pH 7.4. Under mildly acidic conditions typical of tumors (pH 6.5), ZIF-8 was degraded, the Fe-oxide NPs were released from the crystalline structure, and acting as single-domain MNPs, exhibited an increased heating effect approaching that of native Fe-oxide NPs. Potential of this nanosystem to create selective hyperthermia of tumors was further demonstrated *in vitro* with cancerous human glioma cell line (U87) *vs* healthy human kidney cell line (HEK-293-t).

Materials and Methods

Chemicals

Iron (II) chloride tetrahydrate ($FeCl_2 \cdot 4H_2O$), iron (III) chloride hexahydrate ($FeCl_3 \cdot 6H_2O$), 25% ammonia, polyvinylpyrrolidone (PVP), methanol, ethanol, phosphate buffered saline (PBS) were purchased from Sigma Aldrich. 2-methylimidazole (2-mIm) and zinc nitrate ($Zn(NO_3)_2$ were purchased from Thermo Fisher Scientific (Waltham, Massachusetts, United States). Dulbecco's modified Eagle's medium (DMEM), fetal bovine serum (FBS), penicillin-streptomycin, phosphate buffered saline (PBS), and 0.25% Trypsin-EDTA were purchased from Biowest (Avantor, Nuaillé, France). All chemicals were used without further purification.

Synthesis

PVP-modified iron oxide nanoparticles (PVP-Fe_3O_4 NPs): PVP-Fe_3O_4 NPs were prepared using the previously described protocols.[34] In a typical procedure, $FeCl_2 \cdot 4H_2O$ (198.8 mg, 1 mmol) and PVP (250 mg) were dispersed in 10 mL of water under ultrasonication for 15 min. Then, $FeCl_3 \cdot 6H_2O$ (540.6 mg, 2 mmol) in 5 mL of water was added. After the mixture was heated to 60 °C under vigorous stirring, 1.25 mL of ammonia was added dropwise. The reaction mixture was kept under these conditions for 60 min. The resulting NPs were collected with a magnet, washed several times with water and ethanol and dispersed in water at a concentration of 10 mg mL^{-1} for further use.

Zeolitic imidazolate framework encapsulated iron oxide nanocomposites (Fe-ZIF NCs): Zeolitic imidazolate framework-8 (ZIF-8) encapsulation was performed based on the procedures described elsewhere.[35] 3 mL PVP-Fe_3O_4 NPs were collected with a magnet, redispersed in 10 mL of methanol, and ultrasonicated for 30 min. After this, 1.3136 g of 2-mIm was dissolved in 10 mL of methanol and added to the suspension. The mixture was ultrasonicated for another 20 min and stored in a fridge as well as a solution of 595 mg of $Zn(NO_3)_2$ in 10 mL of methanol. After both solutions reached the temperature of 4 °C, they were mixed and stirred at 4 °C at 1000 rpm for 1.5 h. The obtained Fe-ZIF NCs were collected with a magnet, washed with methanol for three times and dried at room temperature.

Characterization

The size and morphology of PVP-Fe_3O_4 and Fe-ZIF NCs were determined by transmission electron microscopy (TEM), using a 120 kV Jeol-JEM1400 microscope. The samples were prepared by drop-casting a diluted NP suspension on a Quantifoil R1.2/1.3 Cu300 grid and evaporating the solvent at room temperature. The size distribution was counted and calculated from TEM images of ± 30 ZIF particles using Nano Measurer 1.2 software. Magnetic characterization by superconducting quantum interference device (SQUID), was carried out on an

MPMS XL magnetometer from Quantum Design, using about 1-2 mg of dry NPs. The hysteresis loops M(H) obtained under continuously increasing applied magnetic field from –50 to 50 kOe at 5 and 300 K were used to obtain the saturation magnetization and coercivity values. Transmission ^{57}Fe Mössbauer spectra were collected at 4.2 K with a conventional constant-acceleration spectrometer using a ^{57}Co(Rh) source. Velocity calibration was carried out using an α-Fe foil. The Mössbauer spectra were fitted using the Mosswinn 4.0 program. Powder X-ray diffraction (XRD) pattern was measured with a PANalytical X'Pert Pro PW3040/60 diffractometer from 10° to 90° at 45 kV and 40 mA (Cu Kα radiation, λ = 1. 54 Å).

pH-responsive heating

The heating measurement system consisted of the Magnetherm Digital device (Nanotherics, UK), equipped with a 60 mm coil to generate magnetic field/frequencies (*vide infra*) and two glass-fiber optic thermometers (Osensa PRB-G40_2.0-STM-MRI) to measure the temperature in the center and at the bottom of the sample tubes. Equilibration of the temperature was allowed for 5 min, while the insulated sample holder was used to reduce heat loss to the environment. Buffers with specific pH were used to simulate microenvironment in tumors (pH 6.5) and normal tissues (pH 7.4). A series of Fe-ZIF NCs dispersions were prepared with the concentrations varying as: 10, 15, 17, 20, and 22 mg mL^{-1}, of which 1 mL was used to study the heating effects. The cooling temperature during the measurements was set as 37 °C and allowed to equilibrate until it varied less than 0.5 °C/1 min before the start of the experiment. The specific loss power (SLP) expressed in W/g_{Fe} as a measure of heating capacity of the NPs, was calculated with Eq. 1:

$$SLP[W/g_{Fe}] = \frac{C}{m_{Fe}} \cdot \frac{\Delta T}{\Delta t} \quad (1)$$

where C is the heat capacity of the sample, m_{Fe} is the mass of Fe obtained from the inductively coupled plasma-mass spectrometry (ICP-MS) analyses of the same samples after a microwave-assisted digestion of the NPs dispersed in a 5% HNO_3, and $\Delta T/\Delta t$ is the measured time-dependent temperature increase.

In vitro studies

Cell cultures: Human glioblastoma astrocytoma cell line (U87) was provided by ATCC, human kidney cell line (HEK-293-t) was kindly donated by Daan Brinks lab, TU Delft, department of imaging physics. Cells were grown in DMEM supplemented with 10% FBS and 1% penicillin-streptomycin at 37 ºC with 5% CO_2.

CCK-8 assay: U87 cells (100 µL well^{-1}, 5×10^4 mL^{-1}) were seeded into 96-well cell-culture plate and then cultured at 37 ºC with 5% CO_2 for 24 h. Fe-ZIF NCs (10 µL well^{-1}) with various concentrations (0-5 mg mL^{-1}) were added to each well and the cells were maintained for 24 h. Then Cell Counting Kit-8 (CCK-8, 10 µL well^{-1}) was added to the wells and incubated at 37 ºC for 4 h. The absorbance at 450 nm (OD_{450}) in each well was measured using PowerWave XS microplate reader from BIO-TEK with background subtraction.

MHT treatments: U87 cells (2 mL, 5×10^4 mL^{-1}) were seeded in 35 mm dishes and then cultured at 37 ºC with 5% CO_2 for 36 h. 1 mL of Fe-ZIF NCs suspension with varying concentrations (0-5 mg mL^{-1}) were added to each dish. A subset of cells was conditioned at pH 7.4 by aspirating the culture medium after 36 h and replacing it with 1 mL PBS. A second group, subjected to MHT treatment, was exposed to an AMF for 45 min at 710 kHz and 10 mT. After the treatments, the liquid in each dish was removed and the cells were washed three times with PBS to remove residual NPs. To normalize the number of the cells in all experiments, the cells in the blank and experiential groups were counted and diluted to 5×10^4 mL^{-1} and seeded in the 96-well cell-culture plate (100 µL $well^{-1}$). After culturing the cells for 24h at 37 ºC with 5% CO_2, CCK-8 (10 µL $well^{-1}$) was added to the wells and incubated at 37 ºC for 4 h. The absorbance at 450 nm in each well was measured using a microplate reader with background subtraction. The viability of cells was calculated according to Eq. 2, using the average absorbance values of the MHT and blank cell groups.

$$Cell\ viability = \frac{Abs_{ave-MHT}}{Abs_{ave-Blank}} \times 100\% \quad (2)$$

Results and Discussion

Synthesis and characterization of Fe-ZIF NCs

The synthesis of ZIF-based hybrid nanocomposites (NCs) in combination with different NPs typically involves the construction of core-shell structures, in which NPs act as seeds, while the ZIF-crystals grow around them.[29-31] When the surfaces of NPs are charged, the opposite charges of the applied ZIF precursors can promote uniform coatings, as reported for anionic Fe-oxide NPs interacting with Zn^{2+} cations to form a ZIF-8 layer.[36] However, in most cases, extra modification is necessary to create enough active sites on the surface of NPs, so that the core-shell structure can be achieved. Therefore, in this work, we used the PVP-modified Fe-oxide NPs described in Chapter 3 as seeds in the synthesis of Fe-ZIF NCs, which were subsequently used as a model to demonstrate pH-responsive MHT.

In the first attempt, Fe-ZIF NCs were synthesized at room temperature with 15 mg of PVP-Fe-oxide NPs. According to TEM, the size of the resulting NCs with an apparent hexagonal shape was about 230 nm (Figure 5.1). The small dark dots observed in association with these large NCs were identified as Fe-oxide NPs based on their higher electron density compared to the ZIF material. However, the number of Fe-oxide NPs observed per each large particle appears relatively small, which may indicate either inefficient incorporation during the synthesis or an excessive size of the final NC particles. Therefore, the next experiments focused on the formation of smaller

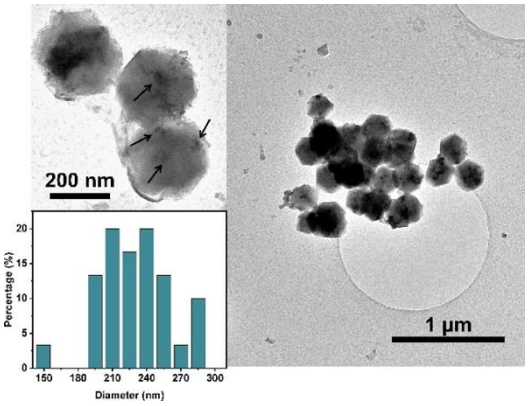

Figure 5.1. TEM images and size distribution of Fe-ZIF NCs synthesized at room temperature using 15 mg of PVP-Fe-oxide NPs.

ZIF-NCs, which was also desirable from an application point of view. One way to achieve this was described by Beh *et al.,* who reported on ZIF-8 with a size about 60 nm, synthesized in an ice bath.[35] The lower reaction temperature reduced nuclear growth and thus improved the nucleation process, yielding smaller ZIF-8 particles with a better size distribution. Adopting this strategy, smaller Fe-ZIF NCs with an average size of ~120 nm could be obtained after stirring at 4 °C for 10 min (Figure 5.2A). Despite this improvement, the shape and size distribution of this batch were still not optimal, as was the Fe-oxide content in each particle. Therefore, in the next experiment, the number of seeds used in the reaction was doubled and the reaction time were prolonged to 30 min and 1.5 h (Figure 5.2B and C). This resulted in a more uniform shape of the obtained NCs while keeping the size small (119.5 ± 32.68 nm). Further extension of stirring time to 2 h showed the hexagon shape of ZIF-NCs was improved, but at the same time the particle size increased (Figure 5.3D).

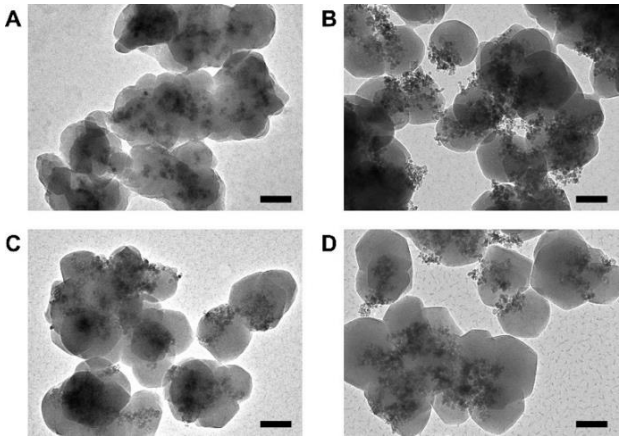

Figure 5.2. TEM images of Fe-ZIF NCs synthesized with 30 mg of PVP-Fe-oxide NPs at 4 ºC and stirring times of 10 min (**A**), 30 min (**B**), 1.5 h (**C**), and 2 h (**D**). Scale bars in all images represent 100 nm.

However, while stirring times of both 30 min and 1.5 h appeared optimal for producing smaller particle sizes, the shorter time, left some Fe-oxide NPs uncoated by ZIF probably due to its insufficient growth, which could compromise the expected pH-responsive heating effect. Therefore, a stirring time of 1.5 h was used to prepare Fe-ZIF NCs for further study, and their composition was subsequently confirmed by X-ray diffraction (XRD) analysis (Figure 5.3). Compared to Fe-oxide NPs, new peaks were found in $2\theta < 40°$, which correspond to the standard card of ZIF-8 (JCPDS no. 01-090-6826). The absence of extra peaks indicated the high purity of Fe-ZIF NCs.

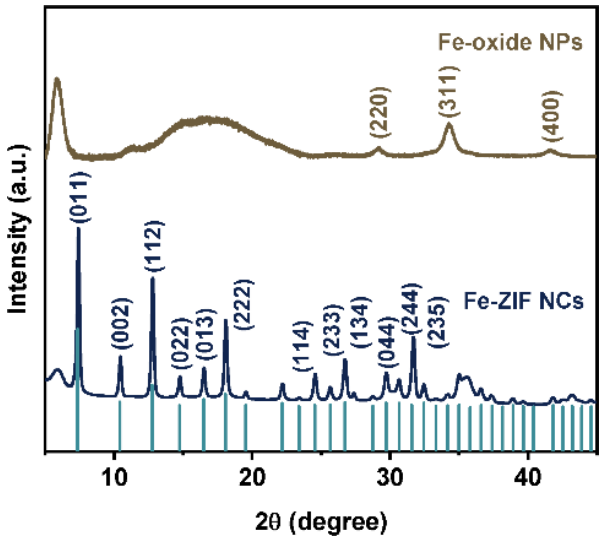

Figure 5.3. XRD patterns of Fe-oxide NPs and Fe-ZIF NCs prepared with 30 mg of PVP-Fe-oxide NPs under vigorous stirring at 4 ºC and for 1.5h.

The static magnetic behavior of dry Fe-ZIF NCs was studied with SQUID magnetometry, measuring magnetization curves at 5 K and 300 K in the presence of magnetic field increasing from –50 to 50 kOe. As shown in Figure 5.4A and B, the saturation magnetization (M_S) values decreased from 62.0 to 13.3 emu/g and from 54.1 to 11.1 emu/g at 5 and 300 K, respectively, as the result of ZIF-encapsulation. Since the M_S values were initially calculated using the total material weight, accounting for the Fe/ZIF ratio, the observed decreases can be partially attributed to the encapsulation of Fe-oxide NPs by ZIF. Correction of the M_S values using the weights of Fe obtained from ICP-MS resulted in increased M_S values (shown as emu/g_{Fe}), with the M_S of Fe-ZIF becoming comparable to that of the uncoated Fe-oxide NPs (Table 5.1). The fact that this correction did not alter the M_S values for Fe-oxide NPs confirms that the observed reduction in magnetization is consistent with the expected effect of ZIF-encapsulation.

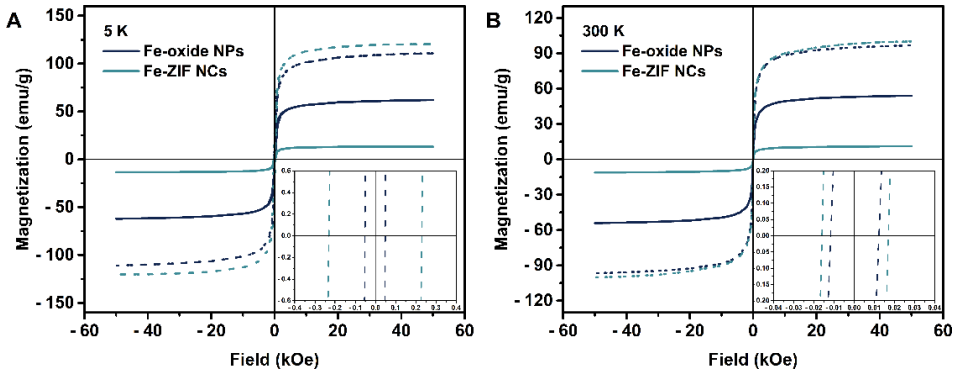

Figure 5.4. SQUID magnetometry performed with dry powders of Fe-oxide NPs and Fe-ZIF NCs resulting in magnetizations (M_S) and coercivities (H_c) in the insets: (**A**) M(H)T curves obtained at T = 5 K (the inset represents 150× magnification of the y-axis) and (**B**) T = 300 K (the inset represents 1500× magnification of the y-axis). The dash lines represent the results after correction for the Fe-concentration.

Table 5.1. Magnetic characteristics of Fe-oxide NPs before and after their encapsulation in ZIF.

Materials	Size (nm)	Saturation Magnetization (M_S) (emu/g)		Coercivity (H_c) (kOe)	
		5 K	300 K	5 K	300 K
Fe-oxide NPs	11.2 ± 2.6	62.0[a] 110.7[b]	54.1[a] 96.6[b]	51.8[a]	11.5[a]
Fe-ZIF NCs	119.5 ± 32.68	13.3[a] 121.1[b]	11.1[a] 100.6[b]	230.6[a]	15.8[a]

[a] Calculated using the total weight of materials. [b] Calculated using the concentration of Fe obtained with ICP-MS.

pH-responsive properties

To study pH-responsive behavior of Fe-oxide NPs after their encapsulation in ZIF, the as-synthesized Fe-ZIF NCs were first dispersed in buffers with different pH. No morphological changes were observed by TEM upon dispersion of Fe-ZIF in PBS (pH 7.4), whereas at pH 6.5 most NCs were partly destroyed (Figure 5.5A-C). Even though a small fraction of Fe-oxide still remained within the ZIF NCs, the majority of the NPs were released (Figure 5.5C). The TEM image of this sample, after centrifugation and re-dispersion in PBS, demonstrates that ZIF can regain its structure when brought back to pH 7.4, while the previously released Fe-oxide NPs were removed during centrifugation and are therefore absent (Figure 5D). These findings suggest that the assembly/disassembly behavior of Fe-oxide NPs can be controlled using the ZIF-structure relying on pH differences of the tumor microenvironment.

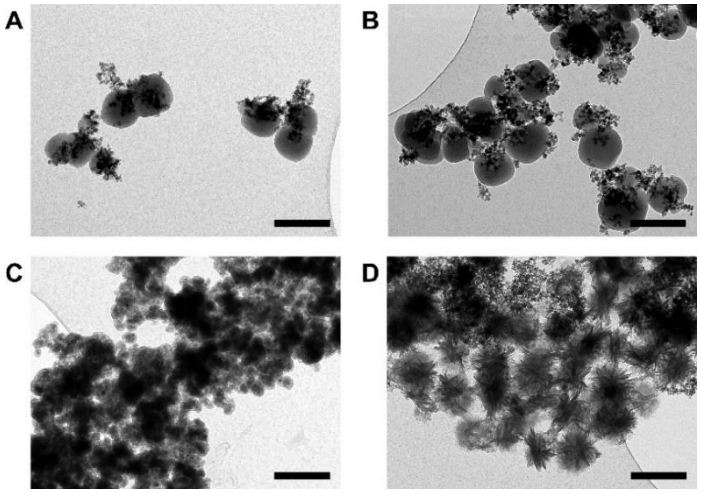

Figure 5.5. TEM images of Fe-ZIF NCs dispersed in (**A**) methanol, (**B**) PBS (pH 7.4), (**C**) acidic buffer (pH 6.5), and (**D**) redispersed in PBS after treated with acidic buffer. Scale bars correspond to 200 nm.

Next, the magnetic properties of the material accompanying the pH changes, the heating behavior of Fe-ZIF NCs was studied at both pH conditions (6.5 and 7.4), with the outcomes designated as Fe-ZIF-6.5 and Fe-ZIF-7.4. To enable a fair comparison of the temperature changes (ΔT) induced by the Fe-ZIF-samples under alternating magnetic field with those caused by Fe-oxide NPs, the weight of Fe-ZIF materials was adjusted to correspond to the exact weight of Fe-oxide NPs (3 mg) used in their preparation. The temperature increase achieved within 5 min at 338 kHz and 18 mT in the presence of Fe-ZIF at pH 6.5 and 7.4 is clearly less effective compared to Fe-oxide NPs (Figure 5.6A). However, the significance of this difference becomes clear when the corresponding SLP values are compared (Figure 5.6B).

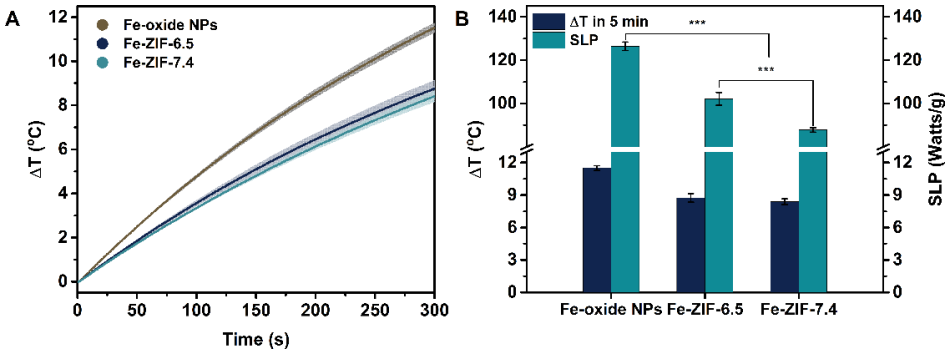

Figure 5.6. pH-responsive magnetic heating of Fe-ZIF NCs compared to Fe-oxide NPs (3 $mg_{Fe\text{-}oxide}$ mL^{-1}): (**A**) heating curves generated during 5 min at 338 kHz and 18 mT, **(B)** comparison of the heating performance considering the temperature change (ΔT) and the SLP values corrected with m_{Fe} determined by ICP-MS.

Besides the ability of the ZIF-coating to attenuate the magnetic heating of Fe-oxide NPs, another important insight is the comparison of the hyperthermic performance of Fe-ZIF NCs in the tumor *vs* normal regions, which can be described by a parameter Δ(ΔT) where average value of $\Delta T_{6.5}$ and $\Delta T_{7.4}$ were used and calculated as $(\Delta T_{6.5} - \Delta T_{7.4})$ Initial measurements of the temperature rise generated with Fe-ZIF NCs at 338 kHz and 18 mT yielded a Δ(ΔT) of 0.26 °C (Figure 5.6A), which is clearly insufficient to achieve the desired tumor specificity. Therefore, the efforts to improve this performance focused on optimalization of the AFM exposure parameters and the applied Fe-concentration. Based on the reported clinical limitation of AFM, imposed by patient safety and expressed as the product of magnetic field strength and frequency,[37] earlier we calculated the equivalent limit value for our experimental setup ($6.3 \cdot 10^3$ T s^{-1}).[38] Table 5.2 lists the field-frequency products for all experimental conditions, several of which approach the abovementioned limit value. However, the 10-min temperature plots obtained at different conditions identified the frequencies of 338 and 710 kHz as producing the strongest Fe-ZIF and a more pronounced difference between pH 6.5 and 7.4, confirming the assumption experimentally (Figure 5.7).

Table 5.2 AMF exposure parameters/results generated by the MagneTherm Digital for pH-responsive heat detection.

Frequency (kHz)	244	289	338	382	437	546	710
Magnetic field (mT)	19	15	18	17	8	5	10
Field-Freq product (T s^{-1})	4636	4335	6084	6876	3496	2730	7100
Δ(ΔT) (°C)	0.18	0.24	0.26	0.24	0.02	0.22	0.41

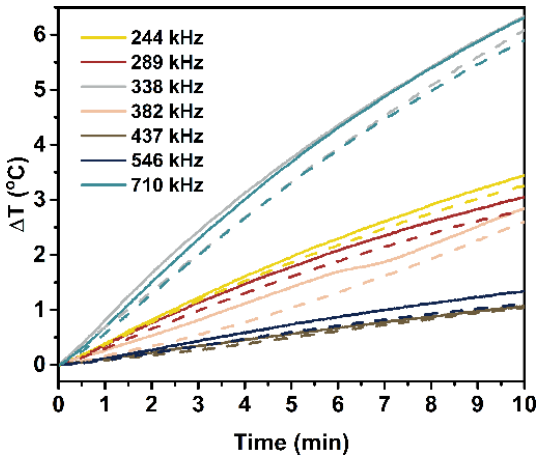

Figure 5.7. Temperature increase generated with Fe-ZIF NCs (10 mg ml^{-1}) measured at pH 6.5 (solid lines) and pH 7.4 (dashed lines) for 10 min at different frequencies with the corresponding magnetic fields as specified in Table 5.2.

The temperature differences calculated for each frequency after 10 min of AFM exposure revealed negligible Δ(ΔT) of 0.22±0.04 ºC between pH 6.5 and 7.4 for most frequencies, with two exceptions of the lowest (0.02 ºC) and highest (0.41 ºC) differences observed at 437 kHz/8 mT and 710 kHz/10 mT, respectively (Table 5.2). The latter AFM parameter set was then used to optimize the applied Fe-concentration, aiming to maximize Δ(ΔT) for improved pH-responsive heating, and thus, more efficient selective heating in the tumor region.

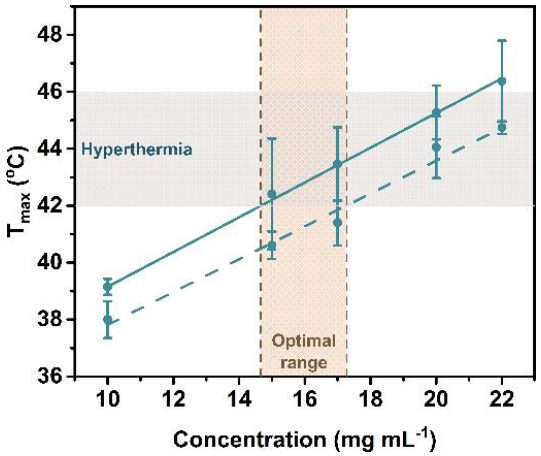

Figure 5.8. Linear fits of the maximum temperatures (T_{max}) obtained after 45 min heating (710 kHz/10 mT) with different concentrations of Fe-ZIF NCs under pH 6.5 (solid line) and pH 7.4 (dashed line). The error bars represent the average of 3 measurements.

The samples with concentrations ranging from 10 to 22 mg mL^{-1} were exposed to AMF during 45 min, and the highest temperatures (T_{max}) were collected from the heating curves (Figure 5.8). The choice of a longer heating time of 45 min was based on the earlier observation of a heating curve at 710 kHz/10 mT that did not reach a plateau after 10 min. The resulting T_{max} values at both pH 6.5 and 7.4 were highly concentration dependent, with a similar slope of 0.61 and 0.58, respectively. According to the corresponding linear fitting results, the lowest temperature required for generation of a therapeutic effect (42 ºC) can be reached at pH 6.5 with the concentration of Fe-ZIF higher than 14 mg mL^{-1}, while at pH 7.4 this minimum concentration is 18 mg mL^{-1}. This concentration range will increase when a higher temperature is required, but there is always a concentration/T_{max} difference between Fe-ZIF-6.5 and Fe-ZIF-7.4 that makes selective MHT feasible.

Tumor-selective magnetic hyperthermia in vitro

The differences in heating temperatures achieved with Fe-ZIF NCs at different pHs were further translated into *in vitro* experiments. Two cell lines were used to evaluate the temperature effects

in tumor (human glioblastoma astrocytoma, U87) and normal (human kidney, HEK-293-t) cells. The viability of both cell lines was determined using a CCK-8 assay, with the absorbance of cells without any treatment being considered as 100% viability. First, the optimal conditions for cell heating had to be determined, taking into account the specific dimensions of the experimental setup, and in particular, the shape and volume of the containers, which can influence the overall temperature. Furthermore, the fact that the cells are attached to the bottom of the wells could mean that lower concentrations of Fe-ZIF are already sufficient to generate an effect similar to the one previously estimated for the concentration range of 14 - 18 mg mL^{-1}. Therefore, initial heating of U87 cells was performed with Fe-ZIF NCs ranging from 0 to 5 mg mL^{-1}, to determine the lowest heating effective concentration. As shown in Figure 5.9A, the absence of AFM resulted in 85% viability up to 5 mg mL^{-1} of Fe-ZIF NCs. In contrast, the groups exposed to AFM showed a significant decrease in viability down to 7.4% starting from 3.3 mg mL^{-1}. A negligible change in viability at 1.7 mg mL^{-1} of Fe-ZIF NCs suggested that the lowest effective concentration for MHT for U87 cells is between 1.7 and 3.3 mg mL^{-1}. A closer look at a smaller concentration range (2.3 to 3.3 mg mL^{-1}) was performed for both U87 and HEK-293-t cell lines, again demonstrating the viability >80% in the absence of AFM (Figure 5.9B).

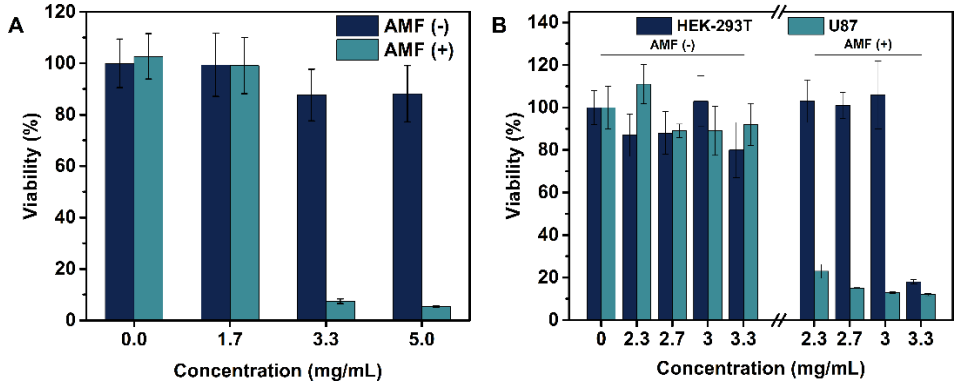

Figure 5.9. *In vitro* investigation of the tumor selective MHT treatment (710 kHz/10 mT, 45 min) using the CCK-8 method. (**A**) Viability of U87 cells treated with Fe-ZIF NCs (0 - 5 mg mL^{-1}) with/without AMF. (**B**) Comparison of the viability of U87 and HEK-293-t cells treated with Fe-ZIF NCs (0 - 3.3 mg mL^{-1}) with/without AMF.

Important observations were made when the same range of Fe-ZIF concentrations was applied to both cell lines exposed to AMF for 45 min. While HEK-293-t cells maintained a viability above 90% up to 3 mg mL^{-1}, it was dropped to 23±3.3% in the case of U87 due to the heating effect generated by released Fe-oxide NPs at lower concentration of 2.3 mg mL^{-1}, further decreasing to 15±0.2% at 2.7 mg mL^{-1}, and only slightly lower (down to 12±0.5%) at higher concentrations. Interestingly, further increasing the concentration of Fe-ZIF NCs in HEK-293-t cells resulted in a decrease in viability down to 18%, indicating that at 3.3 mg mL^{-1} the upper concentration limit to achieve selective MHT, where only tumor is heated above 42 - 45 °C, is exceeded.

Cytotoxicity of Fe-ZIF NCs

Finally, the cytotoxicity of Fe-ZIF NCs was assessed as a key factor, along with heating efficiency, in designing materials for MHT. Both U87 and HEK-293-t cells were incubated with different concentrations of Fe-ZIF NCs (0 - 5 mg mL^{-1}) for extended periods of 24 and 48h and their viability was determined. Comparing the results of HEK-293-t and U87 cells after 24h of incubation with 1 mg mL^{-1} of Fe-ZIF NCs showed that the viability of the former cells remained above 80% (Figure 5.10A), whereas that of the latter dropped to 20% (Figure 5.10B). The minor increase in the viability observed for the higher concentrations of Fe-ZIF NCs added to both cell types could be explained by the interference with the absorbance of iron oxide with OD_{450} used for calculations in the CCK-8 method. On the other hand, the increase in viability at 48h observed in both cell lines, could be explained by the increased metabolism of cells undergoing recovery from the initial exposure to NCs. This phenomenon becomes particularly relevant when using the CCK-8 assay, which measures the metabolic activity of the cells, as opposed to other methods simply count dead cells. This means that the addition of Fe-ZIF NCs may not directly lead to cell death but inhibit their metabolism for a short period of time.

These results suggest that the apparent toxicity of the NCs may be related to the presence of ZIF. A decrease in viability down to 20% previously shown for HEK-293-t cells, was attributed to the slow release of Zn^{2+} from the framework structure at ZIF concentrations above 550 µg mL^{-1}.[39, 40] Another explanation for the unexpected toxicity is the slight change in pH of the culture medium upon addition of Fe-ZIF NCs. In the acidic TME, this effect could be amplified in the presence of pH-responsive NCs, thereby enhancing the therapeutic effect.[41, 42] This may also explain why U87 cells with inherently lower pH are more affected than HEK-293-t, where the NCs remain stable and do not undergo degradation. However, whether Fe-ZIF NCs can sensitize tumors to MHT through direct modulation of pH remains to be investigated.

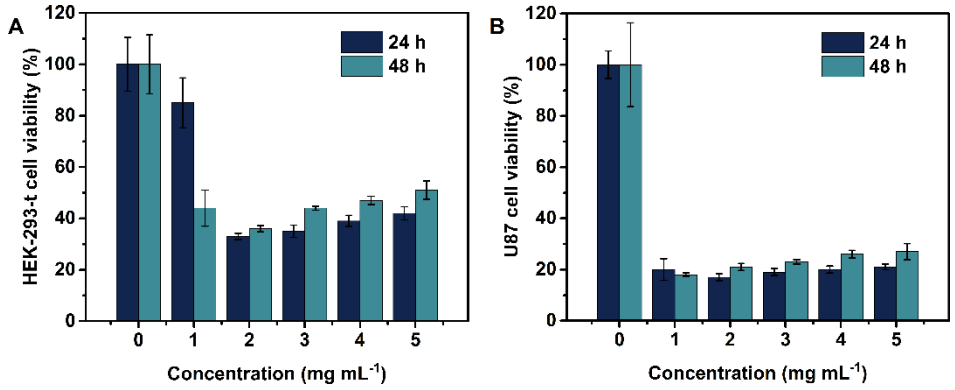

Figure 5.10. Cytotoxicity assessed by determining the viability of: (**A**) HEK-293-t cells, and (**B**) U87 cells incubated with 0 - 5 mg mL^{-1} Fe-ZIF NCs for 24 and 48 h.

Conclusion

In this work, we demonstrated a concept of tumor-selective MHT based on pH differences between normal and tumor tissue. Fe-oxide NPs were synthesized and coated with ZIF-8, which promoted their aggregation, modulation of magnetic properties, and decreased the overall heating performance at physiological pH 7.4. A careful fine-tuning of the synthetic conditions allowed to reduce the size of the obtained Fe-ZIF NCs and fine-tune their pH-responsive magnetic properties. Further optimization concerned the differences in the maximum temperatures arising in the presence of Fe-ZIF NCs at pHs 6.5, typically found in tumor tissues. The best results were obtained using an AFM at 710 kHz and 10 mT, while the optimal concentration of Fe-ZIF NCs required to achieve a tumor-selective temperature rise to 42 - 45 ºC was found to be within the ranges of 14 - 18 and 2.3 to 3 mg mL^{-1} in Eppendorf tubes and cell culture dishes, respectively, reflecting differences in sample geometry and the associated heat dissipation. The results presented here demonstrate the potential of the ZIF-modulated MHT, although improvements in the magnitude of the temperature difference in the tumor tissue are necessary before it can achieve full effectiveness. Finally, the study creates the awareness that the experimental setup itself is a determining factor, which should be taken into consideration, particularly with regard to heat dissipation processes, which in reality will be even more challenging due to complex tissue dimensions and other physiological factors.

References

1. Zafar, A.; Khatoon, S.; Khan, M. J.; Abu, J.; Naeem, A., Advancements and limitations in traditional anti-cancer therapies: a comprehensive review of surgery, chemotherapy, radiation therapy, and hormonal therapy. *Discov Oncol* **2025,** *16* (1), 607.
2. Ahmed, K.; Tabuchi, Y.; Kondo, T., Hyperthermia: an effective strategy to induce apoptosis in cancer cells. *Apoptosis* **2015,** *20* (11), 1411-1419.
3. Chang, D.; Lim, M.; Goos, J. A. C. M.; Qiao, R.; Ng, Y. Y.; Mansfeld, F. M.; Jackson, M.; Davis, T. P.; Kavallaris, M., Biologically Targeted Magnetic Hyperthermia: Potential and Limitations. *Front Pharmacol***2018,** *9*, 831.
4. Jordan, A.; Wust, P.; Fähling, H.; John, W.; Hinz, A.; Felix, R., Inductive heating of ferrimagnetic particles and magnetic fluids: Physical evaluation of their potential for hyperthermia. *I J Hyperth* **1993,** *9* (1), 51-68.
5. Hilger, I.; Frühauf, K.; Andrä, W.; Hiergeist, R.; Hergt, R.; Kaiser, W. A., Heating Potential of Iron Oxides for Therapeutic Purposes in Interventional Radiology. *Ac Radiol***2002,** *9* (2), 198-202.
6. Kötitz, R.; Weitschies, W.; Trahms, L.; Semmler, W., Investigation of Brownian and Néel relaxation in magnetic fluids. *J Magn Magn Maters* **1999,** *201* (1), 102-104.
7. Debye, P. J. W., *Polar molecules*. Dover publications: 1929.
8. Gavilán, H.; Avugadda, S. K.; Fernández-Cabada, T.; Soni, N.; Cassani, M.; Mai, B. T.; Chantrell, R.; Pellegrino, T., Magnetic nanoparticles and clusters for magnetic hyperthermia: optimizing their heat performance and developing combinatorial therapies to tackle cancer. *Chem Soc Rev* **2021,** *50* (20), 11614-11667.
9. Gahrouei, Z. E.; Imani, M.; Soltani, M.; Shafyei, A., Synthesis of iron oxide nanoparticles for hyperthermia application: effect of ultrasonic irradiation assisted co-precipitation route. *Adv Nat Sci Nanosci Nanotechn* **2020,** *11* (2), 025001.
10. Mehdaoui, B.; Meffre, A.; Carrey, J.; Lachaize, S.; Lacroix, L.-M.; Gougeon, M.; Chaudret, B.; Respaud, M., Optimal Size of Nanoparticles for Magnetic Hyperthermia: A Combined Theoretical and Experimental Study. *Adv Func Mater* **2011,** *21* (23), 4573-4581.
11. Abenojar, E. C.; Wickramasinghe, S.; Bas-Concepcion, J.; Samia, A. C. S., Structural effects on the magnetic hyperthermia properties of iron oxide nanoparticles. *Prog Nat Sci Mater Int* **2016,** *26* (5), 440-448.
12. Wahajuddin; Arora, S., Superparamagnetic iron oxide nanoparticles: magnetic nanoplatforms as drug carriers. *Int J Nanomed* **2012,** *7*, 3445-71.
13. Sayed, Z. S.; Hieba, E. M.; Batakoushy, H. A.; Rashdan, H. R. M.; Ismail, E.; Elkatlawy, S. M.; Elzwawy, A., Cancer treatment approaches within the frame of hyperthermia, drug delivery systems, and biosensors: concepts and future potentials. *RSC Adv* **2024,** *14* (53), 39297-39324.
14. Singh, A.; Kumar, N., Estimation of the injection criteria for magnetic hyperthermia therapy based on tumor morphology. *Biomed Phys Eng Express* **2024,** *10* (5), 055017.
15. Bender, P.; Honecker, D.; Fernández Barquín, L., Supraferromagnetic correlations in clusters of magnetic nanoflowers. *Appl Phys Lett* **2019,** *115* (13), 132406.

16. Fu, R.; Yan, Y.; Roberts, C.; Liu, Z.; Chen, Y., The role of dipole interactions in hyperthermia heating colloidal clusters of densely-packed superparamagnetic nanoparticles. *Sci Rep* **2018,** *8* (1), 4704.
17. Guibert, C.; Dupuis, V.; Peyre, V.; Fresnais, J., Hyperthermia of Magnetic Nanoparticles: Experimental Study of the Role of Aggregation. *J Phys Chem C* **2015,** *119* (50), 28148-28154.
18. Cheng, Y. Q.; Wang, S. B.; Liu, J. H.; Jin, L.; Liu, Y.; Li, C. Y.; Su, Y. R.; Liu, Y. R.; Sang, X.; Wan, Q.; Liu, C.; Yang, L.; Wang, Z. C., Modifying the tumour microenvironment and reverting tumour cells: New strategies for treating malignant tumours. *Cell Prolif* **2020,** *53* (8), e12865.
19. Boedtkjer, E.; Pedersen, S. F., The Acidic Tumor Microenvironment as a Driver of Cancer. *Ann Rev Physiol* **2020,** *82* (Volume 82, 2020), 103-126.
20. Corbet, C.; Feron, O., Tumour acidosis: from the passenger to the driver's seat. *Nat Rev Cancer* **2017,** *17* (10), 577-593.
21. Feng, Q.; Bennett, Z.; Grichuk, A.; Pantoja, R.; Huang, T.; Faubert, B.; Huang, G.; Chen, M.; DeBerardinis, R. J.; Sumer, B. D.; Gao, J., Severely polarized extracellular acidity around tumour cells. *Nat Biomed Eng* **2024,** *8* (6), 787-799.
22. Park, Y.; Jeong, E. M., Glutathione Dynamics in the Tumor Microenvironment: A Potential Target of Cancer Stem Cells and T Cells. *Int J Stem Cells* **2024,** *17* (3), 270-283.
23. Wang, Y.; He, J.; Feng, R.; Chen, J.; Xie, G.; Yu, S.; Wu, Y. X.; Tang, K., Lighting up endogenous H_2O_2 in the tumor microenvironment using a dual-mode nanoprobe for long afterglow and MR bioimaging. *Analyst* **2024,** *149* (16), 4230-4238.
24. Qiao, L.; Ou, Y.; Li, L.; Wu, S.; Guo, Y.; Liu, M.; Yu, D.; Chen, Q.; Yuan, J.; Wei, C.; Ou, C.; Li, H.; Cheng, D.; Yu, Z.; Li, Z., H_2S-driven chemotherapy and mild photothermal therapy induced mitochondrial reprogramming to promote cuproptosis. *J Nanobiotech* **2024,** *22* (1), 205.
25. Jia, Q.; Han, X.; Liu, Y.; Liao, X.; Zhou, J., Tumor–microenvironment activated programmable synergistic cancer therapy by bioresponsive rare-earth nanocomposite. *J Rare Earths* **2022,** *40* (9), 1399-1406.
26. Wang, N.; Zeng, Q.; Zhang, R.; Xing, D.; Zhang, T., Eradication of solid tumors by chemodynamic theranostics with H_2O_2-catalyzed hydroxyl radical burst. *Theranostics* **2021,** *11* (5), 2334-2348.
27. Wang, Y.; Zeng, M. T.; Fan, T. F.; Jia, M.; Yin, R. X.; Xue, J.; Xian, L. J.; Fan, P.; Zhan, M., Biomimetic ZIF-8 Nanoparticles: A Novel Approach for Biomimetic Drug Delivery Systems. *Int J Nanomed* **2024,** *19*, 5523-5544.
28. Bunzen, H., Chemical stability of metal-organic frameworks for applications in drug delivery. *Chemnanomat* **2021,** *7* (9), 998-1007.
29. Cai, W. L.; Zhang, W.; Chen, Z. L., Magnetic Fe3O4@ZIF-8 nanoparticles as a drug release vehicle: pH-sensitive release of norfloxacin and its antibacterial activity. *Coll Surf B-Biointerfaces* **2023,** *223*, 113170.
30. Liang, M. M.; Zhou, W. X.; Zhang, H. F.; Zheng, J. T.; Lin, J. M.; An, L.; Yang, S. P., Tumor microenvironment responsive T_1-T_2 dual-mode contrast agent Fe_3O_4@ZIF-8-Zn-Mn NPs for in vivo magnetic resonance imaging. *J Mater Chem B* **2023,** *11* (19), 4203-4210.
31. Lin, J. M.; Xin, P. Y.; An, L.; Xu, Y. J.; Tao, C.; Tian, Q. W.; Zhou, Z. G.; Hu, B.; Yang, S. P., Fe3O4-ZIF-8 assemblies as pH and glutathione responsive T_2-T_1 switching magnetic

resonance imaging contrast agent for sensitive tumor imaging in vivo. *Chem Commun* **2019,** *55* (4), 478-481.

32. Mekrattanachai, P.; Setthaya, N.; Chindawong, C.; Yotnoi, B.; Song, W. G.; Manaspon, C., Synthesis of hydrogels incorporating core-shell structured Fe3O4@ZIF-8 as bio-nanocomposite carriers for drug delivery. *Austr J Chem* **2023,** *76* (4), 201-208.
33. Ghosh, S.; Gul, A. R.; Xu, P.; Lee, S. Y.; Rafique, R.; Kim, Y. H.; Park, T. J., Target delivery of photo-triggered nanocarrier for externally activated chemo-photodynamic therapy of prostate cancer. *Mater Today Chem***2022,** *23*, 100688.
34. El-Boubbou, K.; Lemine, O. M.; Algessair, S.; Madkhali, N.; Al-Najar, B.; Almatri, E.; Ali, R.; Henini, M., Preparation and characterization of various PVPylated divalent metal-doped ferrite nanoparticles for magnetic hyperthermia. *Rsc Adv* **2024,** *14* (22), 15664-15679.
35. Beh, J. J.; Lim, J. K.; Ng, E. P.; Ooi, B. S., Synthesis and size control of zeolitic imidazolate framework-8 (ZIF-8): From the perspective of reaction kinetics and thermodynamics of nucleation. *Mater Chem Phys* **2018,** *216*, 393-401.
36. Chen, G.; Yu, B.; Lu, C.; Zhang, H.; Shen, Y.; Cong, H., Controlled synthesis of Fe3O4@ZIF-8 nanoparticles for drug delivery. *CrystEngComm* **2018,** *20* (46), 7486-7491.
37. Dutz, S.; Hergt, R., Magnetic nanoparticle heating and heat transfer on a microscale: Basic principles, realities and physical limitations of hyperthermia for tumour therapy. *Int J Hyperther* **2013,** *29* (8), 790-800.
38. van Oossanen, R.; Maier, A.; Godart, J.; Pignol, J.-P.; Denkova, A. G.; van Rhoon, G. C.; Djanashvili, K., Magnetic hybrid Pd/Fe-oxide nanoparticles meet the demands for ablative thermo-brachytherapy. *Int J Hyperther* **2024,** *41* (1), 2299480.
39. Johari, S. A.; Sarkheil, M.; Veisi, S., Cytotoxicity, oxidative stress, and apoptosis in human embryonic kidney (HEK293) and colon cancer (SW480) cell lines exposed to nanoscale zeolitic imidazolate framework 8 (ZIF-8). *Environ Sci Pollut Res* **2021,** *28* (40), 56772-56781.
40. Hoop, M.; Walde, C. F.; Riccò, R.; Mushtaq, F.; Terzopoulou, A.; Chen, X.-Z.; deMello, A. J.; Doonan, C. J.; Falcaro, P.; Nelson, B. J.; Puigmartí-Luis, J.; Pané, S., Biocompatibility characteristics of the metal organic framework ZIF-8 for therapeutical applications. *App Mater Today* **2018,** *11*, 13-21.
41. Yustisia, I.; Jusman, S. W. A.; Wanandi, S. I., Extracellular O2 Level and pH Modulation Affected the Human Breast Cancer Stem Cells’ Survival and Stemness. *Adv Sci Lett* **2017,** *23* (7), 6685-6689.
42. Liu, J.; Chen, Q.; Feng, L.; Liu, Z., Nanomedicine for tumor microenvironment modulation and cancer treatment enhancement. *Nano Today* **2018,** *21*, 55-73.

General conclusions and outlook

6

Concluding the thesis, this final chapter provides an overview of the key outcomes, discusses their implications within the broader landscape of magnetic hyperthermia (MHT) research, highlights the limitation of the designed approaches, and outlines directions for future research. First of all, examining research developments in the field hyperthermia (HT) as an adjunctive method for localized cancer treatment, provides important context for the relevance of the work presented in this thesis. The graph in Figure 6.1 clearly shows that, although cancer-related HT-research as whole remains consistently high in number, the MHT-specific subset, and thus the role of nanomaterials, shows a strong increase over the observation period, reflecting growing attention to this research direction. It is evident that advances in nanotechnology create new opportunities for the design of highly efficient MHT systems for oncological treatments. However, rather than focusing exclusively on performance optimization, the main objective of this dissertation was to explore the immense advantages of nanotechnology to address the safety issues of MHT without compromising therapeutic efficacy of MNPs. To achieve this, several strategies were applied to magnetic iron oxide nanoparticles (Fe-oxide NPs), each with its own strengths and weaknesses.

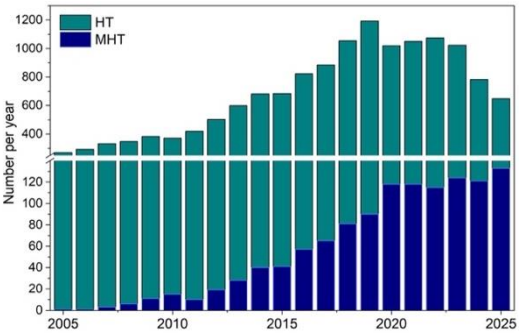

Figure 6.1. Annual number of PubMed-indexed publications from 2005 to 2025 related to general HT and the specific use of MNPs (MHT) in oncology, obtained using queries: (“hyperthermia”) and ("magnetic hyperthermia") or ("nanoparticle hyperthermia") and (“cancer”) and ("2005" [Date-Publication]: "2025"[Date-Publication]). Data were retrieved in 12/ 2025.

The first approach involved boosting the magnetic properties of NPs, which resulted in higher specific loss power (SLP) values, meaning more efficient heat generation under alternating magnetic field (AMF). This reasoning is common in MHT research, and can be translated directly into improved safety, as a higher SLP basically means that the same amount of heat can be achieved with fewer MNPs. The advantage of combining iron with other metals both (para)magnetic and diamagnetic to achieve better heating properties, has been widely explored in the literature.[1] However, the two doping strategies investigated in this thesis offered the opportunity to introduce an additional functionality to MNPs, thus further increasing their therapeutic index. The incorporation of metal ions, such as Mn^{2+} and Ho^{3+}, a lanthanide with one of the highest magnetic moments, into the Fe-oxide lattice can increase the magnetic anisotropy of the hybrid NPs, thereby increasing their SLPs. Besides this improvement, the nature of the doping elements allows for other interesting applications. For example, adding paramagnetic Mn^{2+} into Fe-oxide, enables T_1-weighted MR imaging, provided that the doping is located at the NPs surface. In this case, image contrast arises from the exchange between water molecules coordinated to the surface-bound Mn on the surface and the surrounding bulk water. This

additional feature represents an attractive option for clinical applications for two main reasons. First, positive (bright) T_1 contrast is generally preferred in clinical MRI due to better interpretability. Second, the intrinsically available T_2-weighted contrast of MNPs is often inconvenient as an accompanying imaging modality, as the particle concentrations required for effective heating typically leads to signal oversaturation.[2] The use of T_1-contrast instead of T_2 therefore offers a promising strategy to overcome this limitation, as brighter signals are not only more informative but also less prone to imaging artifacts compared to the dark signals. On the other hand, doping with Ho^{3+}, which next to its superior magnetic properties and thus improved heating, is also known having an attractive radioisotope (^{166}Ho), enables β-radiotherapy as an adjunctive therapeutic modality to MHT. Such a combined approach can further enhance the overall therapeutic efficacy due to the synergistic effects, while reducing the effective concentration of the administered MNPs.

The design of MNPs aimed at maximizing the performance of the above-mentioned functionalities requires the development of suitable synthetic protocols. Cation exchange is the most commonly used method when the morphology of Fe-oxide NPs needs to remain unchanged. However, it requires an extra step during the synthesis and the doping ratio in such a substitution can be difficult to control. Thermal decomposition on the other hand, is a one-step method that offers better control over uniform substitution and results in good morphology, but typically shows low yields while the reaction times are also long. These features can be highly inconvenient, especially for the preparation of MNPs doped with radioisotopes. The co-precipitation method used for Ho^{3+} doping is a more facile and less time-consuming alternative that leads to higher yields, although the particle size and crystallinity are less uniform, and again, hard to control. The application of all three synthetic protocols throughout this thesis not only showed the effect of each method on the final properties of the NPs, but most importantly, provided insight into the trade-offs that can be made during synthesis to balance all these properties, taking into account each element and its associated applications, while ensuring the maximum SLP increase.

While effective MHT requires delivering sufficient number of MNPs to tumor sites, treatment safety implies development of the mechanisms that restricts heating inside the tumor. In terms of efficacy, intratumoral injection is considered a more effective delivery method of MNPs compared to intravenous administration. In this way, the deeply penetrating AMF can work specifically on NPs and the damage to surrounding healthy tissues can be significantly reduced. However, a key concern with intratumoral injection during MHT is the unintentional deposition of MNPs outside the tumor, which can lead to off-site thermotoxicity. Furthermore, the concentration and distribution of MNPs after injection are unknown, making heating control and overall injection accuracy a major challenge in MHT, although the engineering aspects of injection technology itself are beyond the scope of the thesis.

Tumor-selective MNPs for MHT may offer a solution to the problem of injection precision. Specific features of the tumor microenvironment (TME), such as elevated glutathione (GSH) levels or decreased pH, can be used as triggers for MNPs that are modified to respond by

generating heat. An example using the first parameter is a strategy to temporarily limit heating by aggregating Fe-oxide NPs through the formation of disulfide bonds (-S-S-).[3] These can be degraded by GSH, which is overexpressed in TME, resulting in tumor-specific MHT. Similarly, lower pH values in tumors can be exploited by encapsulation of Fe-oxide NPs in nanosystems that initially force their aggregation and reduce heating outside the tumor, where the pH is close to 7.4. Upon intratumoral injection, the ZIF-8 nanocomposites become exposed to the lower pH of the tumor, with the subsequent release of Fe-oxide NPs and the generation of heat. Despite the positive results showing tumor-responsive heating in cancerous vs non-cancerous cells, the small temperature difference and limited control over aggregation remain a bottleneck. Acidic conditions are expected to be sufficient to decompose the ZIF-crystals and unleash the heating capacity of the released NPs. However, the fact that the heat generated was only a small fraction of what was expected for these NPs suggests that the ZIF may not have been completely destroyed. Besides, the aggregation of NPs caused by ZIF encapsulation is difficult to control, which complicates the synthesis of Fe-ZIF with a controlled number of evenly distributed Fe-oxide NPs.

An important aspect that is often overlooked in the research focused on the development of nanomaterials for MHT, is the evaluation of heat distribution. A precise understanding of how heat spreads within biological tissues is crucial to ensure that therapeutic temperatures are reached in the target region but also that the off-target healthy structures are not damaged. This means that next to the particles' characteristics, the variations in tissue composition and local blood flow can also influence the spatial heating pattern, making it essential to assess these effects both experimentally and through modelling. When MNPs are injected intratumorally, their tendency to cluster can lead to the formation of localized 'hot-spots', which may cause uneven thermal dosing and unpredictable therapeutic responses. This is not unique to MHT as it also applies to other therapeutic modalities involving intratumoral injections, such locally administered chemo- or immunotherapies, whose effectiveness also depends heavily on uniform distribution. This illustrates the critical importance of careful treatment planning, which must account for multiple factors, including local conditions, such as tumor type, location, size, density etc., as well as the calculation of the target temperature and NPs concentrations necessary to achieve a therapeutic effect based on the SLP of the MNPs.

Finally, one of the key elements in the development of MNPs for MHT is the *in vitro* assessment of heating performance, which is commonly performed in 2D tumor cell cultures and/or 3D spheroids. While 2D studies provide a first indication of the efficacy of the MNPs, 3D experiments are able to simulate the heating effects under conditions that more closely resemble the *in vivo* tumor environment. Considering the above-mentioned heat distribution when cells are incubated in petri dishes, they are exposed to evenly distributed MNPs that produce virtually the same heat throughout the water volume, whereas in reality, the heat dissipation will be strongly influenced by the heat generated around the injection points and its distance from it.[4]

In general, although MHT has demonstrated considerable potential, further research should include comprehensive safety assessment and improvement. This is as critical as optimizing the therapeutic performance of the materials designed to implement the treatment.

References

1. Sathya, A.; Guardia, P.; Brescia, R.; Silvestri, N.; Pugliese, G.; Nitti, S.; Manna, L.; Pellegrino, T., CoxFe3–xO4 Nanocubes for Theranostic Applications: Effect of Cobalt Content and Particle Size. *Chem Mater* **2016,** *28* (6), 1769-1780.
2. Maier-Hauff, K.; Ulrich, F.; Nestler, D.; Niehoff, H.; Wust, P.; Thiesen, B.; Orawa, H.; Budach, V.; Jordan, A., Efficacy and safety of intratumoral thermotherapy using magnetic iron-oxide nanoparticles combined with external beam radiotherapy on patients with recurrent glioblastoma multiforme. *J Neurooncol* **2011,** *103* (2), 317-24.
3. Liu, Y.; Fan, H.; Guo, Q.; Jiang, A.; Du, X.; Zhou, J., Ultra-small pH-responsive Nd-doped NaDyF4 Nanoagents for Enhanced Cancer Theranostic by in situ Aggregation. *Theranostics* **2017,** *7* (17), 4217-4228.
4. Alamouti, A. K.; Raouf, I.; Zahabi, S.; Salimibani, M., Numerical study of magnetic nanoparticles injection into a brain tumor considering the effects of injection volume and location on the termination of cancerous cells. *Biointerphases* **2024,** *19* (6), 061005.

Summary

Multifunctional, biocompatible magnetic materials, such as iron oxide nanoparticles (Fe-oxide NPs), hold great potential for biomedical applications, including diagnostics (e.g., MRI) and cancer therapy. In particular, they can play a crucial role in advancing cancer thermotherapy by generating heat when administered intratumorally and exposed to an alternating magnetic field. This heat application is often combined with radio(chemo)therapy and/or imaging. Designing materials for such a multimodal approach requires hybrid nanoparticles that retain their magnetic properties while integrating additional functionalities. However, while pursuing additional properties, the safety of treatment should also be considered. For instance, reducing the amount of Fe-oxide NPs used for the treatment may minimize safety concerns related to dose-related toxicity, while focusing on tumor treatment selectivity may help avoid unpredictable damage to adjacent healthy tissues caused by intratumoral injection. The mechanisms of thermotherapy by means of magnetic NPs and the associated safety considerations are described in **Chapter 1.**

In **Chapter 2**, the synthesis and investigation of magnetically enhanced nanoparticles with a palladium core (envisioned for future radiolabeling with therapeutic ^{103}Pd) and a magnetic iron oxide shell containing paramagnetic manganese (Pd/Fe|(nMn)-oxide, n = 0.25 and 0.5) were introduced. Doping the iron oxide lattice with Mn significantly increases magnetic saturation (M_S), boosting specific loss power (SLP) up to 1.7 times compared to undoped analogues. Interestingly, higher Mn content in Pd/Fe|(0.5Mn)-oxide leads to a pronounced Mn outer rim, enhancing the heating efficiency at 346 kHz and 23 mT and contributing to the water exchange on the surface of the paramagnetically doped nanoparticles, resulting in additional T_1-weighted MRI contrast. The enhanced magnetic properties of the hybrid Pd/Fe|Mn-oxide NPs enable effective therapeutic outcomes with injection of only small quantities of the material, offering great potential for effective cancer treatment strategies that combine hyperthermia/thermal ablation with radiotherapy, while allowing for real-time monitoring via MRI.

In **Chapter 3**, holmium (envisioned for future radiolabeling with therapeutic ^{166}Ho) was doped into iron oxide nanoparticles (xHo/Fe-oxide NPs, x = 0.1 - 5%) via modified co-precipitation method and investigated their influence on M_S and SLP. It was shown that the Ho-doping ratio up to 0.5% was not sufficient to increase M_S and SLP values, which mainly depend on the size of the resulting nanoparticles. Starting at 0.5% Ho-doping, both M_S and SLP values increased as the Ho-doping ratio rose, reaching their maximum at 2.5%. Further increases in the doping ratio caused M_S and SLP to decrease due to larger particle size and insufficient lattice substitution. This explanation was supported by another batch synthesized at room temperature, which also showed poor Ho lattice distribution along with reduced M_S and SLP. These findings indicated the possibility of improving magnetic and heating properties by tuning Ho-doping, which provided the basis for developing ^{166}Ho-labeled Fe-oxide NPs for combined magnetic hyperthermia and radiotherapy (MHT-RT).

Subsequently, in **Chapter 4**, Ho^{3+} in 2.5%Ho/Fe-oxide NPs was replaced by therapeutic ^{166}Ho to investigate their potential for synergistic MHT-RT. *In vitro* experiments using both single and combined treatments were performed on U87 and U2OS cell lines by evaluating their viability after incubation with $^{165/166}Ho$/Fe-oxide NPs with/without AMF. For both cell lines, the lower viability of treated with MHT+RT was observed compared to cells treated with either treatment alone, clearly demonstrating the synergistic potential of ^{166}Ho/Fe-oxide NPs. When applying both MHR and RT, the effective concentration could be reduced to 2 mg mL^{-1} and 2.5 mg mL^{-1}, and the radioactivity to 1.6 MBq and 0.3 MBq for U87 and U2OS cells, respectively. This shows that the synergistic effect allows for a reduction in the required concentration and activity of NPs to avoid the dose-related toxicity on healthy tissues.

Chapter 5 presents the concept of pH-responsive Fe-oxide nanocomposites (Fe-ZIF NCs) to improve the tumor selectivity of MHT. ZIF-8 was coated onto Fe-oxide NPs to induce their aggregation, and therefore, reduce the overall heating performance at physiological pH 7.4. In the tumor microenvironment, known to be more acidic, the heating performance was recovered, and a temperature difference was observed. By optimizing the AMF frequency, synthesis condition, NPs concentration and particle size, the maximum heating temperatures were tuned to the therapeutic ranges of 42 - 45 ºC reached only at acidic pH. *In vitro* experiments with U87 and HEK-293t cells further demonstrated the tumor-selective MHT effect. Using AFM at 710 kHz and 10 mT for 45 min, Fe-ZIF NCs showed selective cytotoxicity for U87 cells within the concentration range of 2.3–3 mg mL^{-1}. This work demonstrates a promising approach for improving MHT selectivity through modulation of the aggregation state of Fe-oxide NPs.

Finally, **Chapter 6** provides a brief overview of the relevance of hyperthermia in oncology and the role of nanomaterials in its advancement. The objectives of this thesis are then contextualized in relation to developments in the field, and the main limitations are discussed. Ultimately, this critical perspective crystallizes into recommendations regarding the main findings.

Samenvatting

Multifunctionele, biocompatibele magnetische materialen, zoals ijzeroxide-nanodeeltjes (Fe-oxide NPs), zijn veelbelovend voor biomedische toepassingen, waaronder diagnostiek (e.g. MRI) en kankertherapie. Ze kunnen met name een cruciale rol spelen in de ontwikkeling van thermotherapie bij kanker door warmte te genereren wanneer ze intratumoraal worden toegediend en worden blootgesteld aan een wisselend magnetisch veld. Deze warmtetoepassing wordt vaak gecombineerd met radio(chemo)therapie en/of beeldvorming. Het ontwerpen van materialen voor een dergelijke multimodale aanpak vereist hybride NPs die hun magnetische eigenschappen behouden en tegelijkertijd extra functionaliteiten integreren. Bij het streven naar extra eigenschappen, moet echter ook rekening worden gehouden met de veiligheid van de behandeling. Zo kan het verminderen van de hoeveelheid Fe-oxide-NP's die voor de behandeling wordt gebruikt, de dosisafhankelijke toxiciteitsrisico's minimaliseren, terwijl een grotere focus op selectiviteit bij tumorbehandeling kan helpen om onvoorspelbare schade aan omliggende gezonde weefsels, veroorzaakt door intratumorale injectie, te voorkomen. De mechanismen van thermotherapie met behulp van magnetische NPs en de bijbehorende veiligheidsaspecten worden beschreven in **Hoofdstuk 1.**

Hoofdstuk 2 introduceert de synthese en karakterisering van magnetisch versterkte NPs met een palladiumkern (bedoeld voor toekomstige radiolabeling met therapeutische ^{103}Pd) en een magnetische ijzeroxideschil met paramagnetisch mangaan (Pd/Fe|(nMn)-oxide, n = 0,25 en 0,5). Dotering van het ijzeroxiderooster met Mn verhoogt de magnetische saturatie (MS) aanzienlijk, wat leidt tot een toename van het specifieke verliesvermogen (SLP) tot wel 1.7 keer in vergelijking met ongedoteerde analogen. Interessant is dat het hogere Mn-gehalte in Pd/Fe|(0,5Mn)-oxide leidt tot een explicite buitenste Mn-rand, wat de verwarmingsefficiëntie verhoogt bij frequenties van 346 kHz en 23 mT en de wateruitwisseling op het oppervlak van paramagnetisch versterkte nanodeeltjes bevordert, wat resulteert in een toename van het T_1-gewogen MRI-contrast. De verbeterde magnetische eigenschappen van Pd/Fe|Mn hybride oxide NPs maken het effectieve therapeutische resultaten mogelijk met slechts kleine hoeveelheden van het materiaal. Dit biedt grote mogelijkheden voor de ontwikkeling van effectieve strategieën voor de behandeling van kanker, waarbij hyperthermie/thermische ablatie gecombineerd wordt gecombineerd met radiotherapie, terwijl realtime monitoring met MRI mogelijk is.

In **Hoofdstuk 3** werd holmium (beoogd voor toekomstige radiolabeling met therapeutisch ^{166}Ho) gedoteerd in ijzeroxide-nanodeeltjes (xHo/Fe-oxide NPs, x = 0.1 - 5%) via een gemodificeerde coprecipitatiemethode en werd de invloed ervan op MS en SLP onderzocht. Er werd aangetoond dat een Ho-dopingverhouding tot 0.5% niet voldoende was om de MS- en SLP-waarden te verhogen, die voornamelijk afhangen van de grootte van de resulterende NPs. Vanaf 0.5% Ho-doping namen zowel de MS- als SLP-waarden toe naarmate de Ho-dopingverhouding toenam, tot een maximum van 2.5%. Verdere verhogingen van de dopingverhouding zorgden ervoor dat MS

en SLP afnamen als gevolg van een grotere deeltjesgrootte en onvoldoende roostersubstitutie. Deze verklaring werd ondersteund door een andere batch, gesynthetiseerd bij kamertemperatuur, die eveneens een slechte Ho-roosterverdeling vertoonde, samen met een verminderde MS en SLP. Deze bevindingen duidden op de mogelijkheid om de magnetische en verwarmingseigenschappen te verbeteren door Ho-doping af te stemmen, wat de basis vormde voor de ontwikkeling van ^{166}Ho-gelabelde Fe-oxide NPs voor gecombineerde magnetische hyperthermie en radiotherapie (MHT-RT).

Vervolgens werd in **Hoofdstuk 4** Ho^{3+} in 2.5% Ho/Fe-oxide NPs vervangen door radiotherapeutische ^{166}Ho om hun potentieel voor synergetische MHT-RT te onderzoeken. In vitro-experimenten met zowel afzonderlijke als gecombineerde behandelingen werden uitgevoerd op U87- en U2OS-cellijnen door hun levensvatbaarheid te evalueren na incubatie met $^{165/166}$Ho/Fe-oxide NPs met/zonder AMF. Voor beide cellijnen werd een lagere levensvatbaarheid waargenomen van cellen behandeld met MHT+RT in vergelijking met cellen behandeld met alleen een van beide behandelingen, wat duidelijk het synergetische potentieel van ^{166}Ho/Fe-oxide NP's aantoont. Bij toepassing van zowel MHR als RT kon de effectieve concentratie worden verlaagd tot 2 mg ml^{-1} en 2.5 mg ml^{-1}, en de radioactiviteit tot 1.6 MBq en 0.3 MBq voor respectievelijk U87- en U2OS-cellen. Hieruit blijkt dat het synergetische effect een verlaging van de benodigde concentratie en activiteit van NPs mogelijk maakt, om zo de dosisgerelateerde toxiciteit voor gezond weefsel te voorkomen.

Hoofdstuk 5 beschrijft het concept van pH-responsieve Fe-oxide nanocomposieten (Fe-ZIF NCs) om de tumorselectiviteit van MHT te verbeteren. ZIF-8 werd op Fe-oxide NPs gecoat om hun aggregatie te induceren en daarmee de algehele verwarmingsefficiëntie bij fysiologische pH 7.4 te verminderen. In de tumormicro-omgeving, waarvan bekend is dat deze zuurder is, werd de verwarmingsefficiëntie hersteld en werd een temperatuurverschil waargenomen. Door de AMF-frequentie, synthesecondities, NP-concentratie en deeltjesgrootte te optimaliseren, werden de maximale verwarmingstemperaturen afgestemd om therapeutische bereiken van 42 - 45 ºC te bereiken, uitsluitend bij een zure pH. In vitro-experimenten met U87- en HEK-293t-cellen toonden het tumorspecifieke effect van MHT verder aan. Met behulp van AFM bij 710 kHz en 10 mT gedurende 45 min toonden Fe-ZIF NC's selectieve cytotoxiciteit aan voor U87-cellen in het concentratiebereik van 2.3 - 3 mg ml^{-1}. Deze studie laat een veelbelovende aanpak zien om de MHT-selectiviteit te verbeteren door de aggregatiestatus van ijzeroxide-nanodeeltjes te moduleren.

Tot slot geeft **Hoofdstuk 6** een kort overzicht van de relevantie van hyperthermie in de oncologie en de rol van nanomaterialen in de ontwikkeling ervan. Vervolgens worden de doelstellingen van dit proefschrift in context geplaatst ten opzichte van de ontwikkelingen binnen het vakgebied en worden de belangrijkste beperkingen besproken. Uiteindelijk mondt dit kritische perspectief uit in aanbevelingen met betrekking tot de voornaamste bevindingen.

List of publications

Maier, A., **Jia, Q.**, Shukla, K. J., Dugulan, A. I., Hagedoorn, P. L., van Oossanen, R., van Rhoon, G. C., Denkova, A. G., Djanashvili, K. Enhancing Magnetic Hyperthermia Efficiency in Pd/Fe-Oxide Hybrid Nanoparticles through Mn-Doping, *ACS Applied Nano Materials*. **2024**.

Uliss, P., Gai, H., Kahler, F., Aprea, E., **Jia, Q.**, Gkouzioti, V., Frimat, J-P., Brück, E. H., Boutry, C. M., Burn-Safe Biodegradable Magnetocaloric Composites for Temperature-Controlled Biomedical Applications, *Advanced Science.* **2025**.

Posters

Qi Jia, Antonia Denkova, Kristina Djanashvili. “Heat-Producing and Heat-sensing Iron Oxide Nanoparticles” – RST/RID PhD Day, 23 Spetember 2022, Delft, The Netherlands.

Qi Jia, Alexandra Maier, Keshav Shukla, Achim Iulian Dugulan, Peter-Leon Hagedoorn, Rogier van Oossanen, Gerard C. van Rhoon, Antonia G. Denkova, and Kristina Djanashvili. “Enhancing Magnetic Hyperthermia Efficiency with Mn-Doped Pd/Fe-oxide Nanoparticless” – NOW CHAINS 2024, Veldhoven, The Nederlands.

Qi Jia, Antonia Denkova, Kristina Djanashvili. “Magnetic Element Doping of Iron Oxide Nanoparticles for Enhanced Performance in Cancer Thermo-Radiotherapy” – IOCN 2025, 22-24 September 2025, online.

Acknowledgements

First of all, I would like to thank my promoters, *Dr. Kristina Djanashvili* and *Prof. Dr. Antonia Denkova*, for providing me with the opportunity to study in this interesting field. Kristina, you have helped me greatly, both in my research and in my life. You were always kind and patient whenever I came to your office, whether I had questions, felt upset, or even showed you presentation slides full of Chinese during my first year. You pointed out my problems when I struggled with my experiments and advised me to change direction instead of continuing fruitlessly. When I had a new idea, you listened with patience and discussed it with me, but you also knew when to tell me to "stop" when I overthought things. Thank you for encouraging me and even making me "smile" during my hardest times; it truly helped a lot. You are the best supervisor, and it has been a pleasure working with you. Antonia, thank you for your kind suggestions and support with my experiments. Thank you for helping me whenever I encountered difficulties with cell experiments and work in the cell lab.

Finishing a PhD is a long journey, and writing this thesis has been one of the most challenging tasks. Therefore, I would like to thank *Dr. Taoran Chen*, who was always there supporting and encouraging me to complete my thesis. Although we have known each other for only a few months and are not even in the same country, your words and voice were incredibly supportive and helped me sleep well. Thank you for coming to the Netherlands in December, and I hope to see you in Beijing.

Most of the experiments would have been far more difficult without the help and support from technicians, colleagues, and collaborators. *Baukje*, thank you for introducing me to everything in the lab. *Astrid*, thank you for your help with all cell experiments. *Folkert*, thank you for modifying the laser for me. *Johan*, thank you very much for providing me with a space for laser experiments. *Wiel*, *Robert*, and *Sebastian*, thank you for the training on TEM, XRD, and SQUID machines. *Iulian*, thank you for performing the Mössbauer experiments and explaining everything to me. *Alexandra* and *Rogier*, thank you for sharing your experiences working with Fe-oxide nanoparticles and hyperthermia.

To my friends *Zhao Zishan, Huang Xueqi, Li Yuan, Shang Yuchen*: thank you for your support and delicious food from China. *Yuxin*, thank you for all your suggestions and support; it was wonderful to have someone to discuss with. *Chaofan, Yueer, Yinqi, Ziying*: it was a great pleasure

to meet you all in the Netherlands, and thank you for all your help, dinners, and travel invitations. *Bing, Juncheng (and Jiechen), Runze, Chao, Huanhuan,* and *Hu*: I had not expected so many Chinese colleagues in our group before I arrived. Thank you all for being there; you made me feel at home in a foreign country. *Svenja, Gauri, Esther,* and *Marousha*: I really enjoyed our time together in the same office. Thank you.

Last but not least, I offer my greatest appreciation to my parents and all my family. This was my first time so far away from home, but you always understood me and supported my choices. I love you all!

Jackey

Beijing, January 2026

Curriculum Vitae

Qi Jia was born on March 30, 1996, in Beijing, China. After graduating from high school in 2014, she started her undergraduate studies in Chemistry at Capital Normal University and received her B.Sc. in 2018 under the supervision of Prof. Jing Zhou. Then she continued her Master's studies in physical chemistry in the same group. Her research focused on the design of inorganic nanoparticles for disease detection and tumor therapy. Supported by the China Scholarship Council (CSC), she started her PhD study in November 2021 in the Department of Biotechnology at Delft University of Technology. Her research is conducted in the Applied Radiation and Isotopes (ARI) group in the Department of Radiation Science under the supervision of Dr. Kristina Djanashvili and Prof. dr. ir. Antonia Denkova. Her research focuses on the design and modification of magnetic nanoparticles for magnetic hyperthermia to improve treatment efficiency and safety.